Scuola Internazionale Superiore di Studi Avanzati - Trieste

Accretion Tori around Black Holes

Thesis submitted for the degree of
"Doctor Philosophiæ"

CANDIDATE:
Pedro J. Montero Muriel

SUPERVISORS:
Prof. John C. Miller
Prof. Luciano Rezzolla

October 2004

SISSA – Via Beirut 2-4 – 34014 TRIESTE – ITALY

Table of Contents

Citations to Published Work

The contents of Chapter 2 appear in:

> "Oscillations of vertically integrated relativistic tori – II. Axisymmetric modes in a Kerr spacetime", P. J. Montero, L. Rezzolla, and S. Yoshida, MNRAS in press (preprint: astro-ph/0407642)
>
> "Dynamics of oscillating relativistic tori around Kerr black holes", O. Zanotti, J. A. Font, L. Rezzolla and P. J. Montero, submitted to MNRAS.

Part of Chapter 3 appears in:

> "A new three-dimensional general-relativistic hydrodynamics code", L. Baiotti, I. Hawke, P. J. Montero and L. Rezzolla, *"1st Italian Workshop of Computational Astrophysics"*, Mem. Soc. Astron. Ital., (2003)
>
> "Three-dimensional relativistic simulations of rotating neutron star collapse to a Kerr black hole", L. Baiotti, I. Hawke, P. J. Montero, F. Loffler, L. Rezzolla, N. Stergioulas, J.A. Font and E. Seidel, submitted to Phys. Rev. D (preprint: gr-qc/0403029).

Acknowledgments

I would like to thank colleagues and friends at SISSA with whom I have spent a large amount of my time over the past four years. In particular, I would like to express my thanks to my supervisors, John C. Miller and Luciano Rezzolla, for giving me the opportunity to carry out this research, and for their help and support during these years. I am also very grateful to Shin'ichirou Yoshida, who introduced me to the world of linear perturbative analysis, and to Koji Uryu, with whom I had many helpful discussions and carefully read Chapters 3, 4 & 5 of this Thesis.

I would like to thank the Astrophysics group at the University of Valencia (Spain) and in particular, José María Ibáñez, José Antonio Font and Olindo Zanotti for their warm hospitality while I visited them and for their advise and collaboration. In addition, I would like to mention that being a member of the EU-Network on Sources of Gravitational Waves has been a very fruitful experience.

Finally, but surely not less important, are family and friends that I will thank personally.

Overview

The work presented in this Thesis has been developed along two complementary lines: the construction of numerical relativistic codes to follow the non-linear dynamics of compact objects and the study of the oscillation properties of relativistic tori using linear perturbative analysis. In what follows, a brief overview on how this work has been carried out will be presented. In particular, Chapter 1 serves as an introduction to the oscillation properties of accretion discs and the runaway instability of tori around black holes since these issues are the main motivation behind the work presented in this Thesis.

In Chapter 2 of this Thesis we investigate the oscillation properties of nonself-gravitating, relativistic tori orbiting around black holes. We extend the work done in a Schwarzschild background and consider the axisymmetric oscillations of vertically integrated tori in a Kerr spacetime. The tori are modeled with a number of different non-Keplerian distributions of specific angular momentum and we discuss how the oscillation properties depend on these and on the rotation of the central black hole. We first consider a local analysis to highlight the relations between acoustic and epicyclic oscillations in a Kerr spacetime and subsequently perform a global eigenmode analysis to compute the axisymmetric p-modes. In analogy with what was found in a Schwarzschild background, these modes behave as sound waves and are globally trapped in the torus. For constant specific angular momentum distributions, the eigenfrequencies appear in a sequence 2:3:4:... which is essentially independent of the size of the disc and of the black hole rotation. For non-constant angular momentum distributions, on the other hand, the sequence depends on the properties of the disc and on the spin of the black hole, becoming harmonic for sufficiently large tori. We also compare the linear perturbative approach with non-linear hydrodynamic simulations of geometrically thick discs performed with a 2D general relativistic hydrodynamic code. Next, we present estimates of the gravitational wave emission due to the oscillations of high density tori. We also comment on how p-modes in low-density tori could explain the high frequency quasi-periodic oscillations observed in low-mass X-ray binaries with a black hole candidate and the properties of an equivalent model in Newtonian physics.

An introduction to numerical relativistic hydrodynamics is presented in Chapter 3. The first part of this Chapter is devoted to the 3+1 decomposition of the Einstein equations and a conformal traceless reformulation of this system of equations. Next, we concentrate on the high resolution shock capturing schemes which are the most advanced methods for solving the hydrodynamic equations. In the final part of this Chapter, we concentrate on three dimensional general relativistic hydrodynamic simulations and the development of a new 3D, parallel and general relativistic hydrodynamic code, the `Whisky` code. This code implements high resolution shock capturing methods and exploits the spacetime evolution provided by the `Cactus` code. We describe our contributions to the `Whisky` code, several numerical tests we have performed and simulations of relativistic tori orbiting around Schwarzschild black holes we have carried out. We also note that this code has recently been used to investigate the dynamics of the gravitational collapse of rotating neutron stars to form Kerr black holes.

The following two chapters are devoted to the study of relativistic compact objects in axisymmetry by means of numerical simulations and to the development of the computational tools needed to solve the combined system of Einstein equations and the general relativistic hydrodynamic equations. With the aim of investigating the dynamics of geometrically thick self-gravitating tori orbiting around black holes and assessing whether these systems may be subject to the runaway instability, we have developed a new two dimensional, fully relativistic and non-vacuum code, the `Nada` code for the study of axisymmetric systems. The `Nada` code implements high resolution shock capturing methods and the Einstein equations are cast into a system of constraint and evolution equations in the 3+1 decomposition of this system of equations. In particular, Chapter 4 focusses on the description of the `Nada` code. We first present the method we have implemented to impose the axisymmetry condition while using Cartesian coordinates. Next, we describe the boundary conditions and gauge conditions implemented in our code and we conclude the Chapter with an outline of the formulation of the relativistic hydrodynamic equations used and the schemes to integrate in time the coupled system of the Einstein equations and the relativistic hydrodynamic equations. In the following Chapter, Chapter 5, we present several tests performed to assess the accuracy of the code and results from simulations of spherical relativistic stars.

Chapter 1

Introduction to Accretion Tori

It was after the discovery of quasars that Lyndell-Bell (1969) proposed the system of an accretion disc orbiting around a supermassive black hole as an explanation for the energy source of quasars. Since then, accretion discs have become increasingly important in astrophysics as these are believed to play a key role in various active processes in the Universe such as high-energy radiation, formation of astrophysical jets and binary evolution. Accretion discs may be geometrically thin if the rotating gas follows a Keplerian rotation law but in several situations, specially in the vicinity of the compact object, they may also be geometrically thick, case in which they are often referred as tori. Furthermore, accretion discs (both tori and geometrically thin ones) may appear as optically thin or thick according to the properties of the optical depth in different regions of the disc.

Relativistic tori orbiting around black holes are expected to form as a result of the core collapse in massive stars, $M > 25M_{\odot}$ (MacFadyen & Woosley 1999; Sekiguchi & Shibata 2004) or after the merger of neutron stars (Ruffert & Janka 2001; Shibata et al., 2003). Moreover, most current models for the central engine of gamma-ray bursts involve an accretion torus orbiting around a black hole (Woosley & MacFadyen 1999; Narayan et al., 2001; *cf.* Piran 2004 for a review) and fully relativistic numerical simulations are necessary to establish whether these systems may be subject to instabilities that can lead to the destruction of the disc which could be a major problem for these models of gamma-ray burst that require a black hole and a torus system.

An analytic theory of relativistic optically thick tori around black holes was developed by a number of authors mainly in the seventies (Fishbone 1976; Abramowicz 1978, Kozlowski 1978) after the study of equipotential surfaces inside relativistic differentially rotating perfect fluids with barotropic equation of state by Boyer (1965) and Abramowicz (1974) (in this case the surfaces of constant pressure coincide with the equipotential surfaces). The investigations of Abramowicz (1978) and Kozlowski (1978) led to an analytic theory of the hydrodynamical structure of non-selfgravitating tori in an stationary and axially symmetric spacetime. One of the main results of these studies was that stationary configurations of matter exist and that some of these configurations have sharp cusp located in the equatorial plane. The importance of a sharp cusp is that it can behave as an effective L_1 Lagrange point on the Roche lobe of a close binary system, that is a point at which there is a local force balance in which the gravitational force cancels the centrifugal force. As a result of this balance, accretion of matter through the cusp, where the pressure gradients and the pressure are zero, onto the compact object is possible even in absence of shear viscosity in the fluid. Furthermore, Abramowicz et al. (1983) found that accretion through the cusp could lead to an instability, the so called *runaway instability*, in which the accretion rate diverges on a dynamical time scale. On the other hand, if tori are not subject to the instabilities, it has been recently found by Zanotti et al. (2003) that radial oscillations of the tori can lead to quasi-periodic accretion. Moreover, Zanotti et al. (2003) found that the lower eigenfrequencies of such oscillations appear in a sequence of small integers 2:3:4..., rather independently of the size of the torus and the distribution of specific angular momentum. Zanotti et al. (2003) showed that in the case of high-density tori, this oscillations can lead to a significant emission of gravitational waves. In the case of low-density tori, Rezzolla et al. (2003a) proposed a simple model that exploits the properties of p-mode oscillations of tori to explain the high frequency quasi-periodic oscillations (HFQPOs) in low mass X-ray binaries (LMXBs).

Since the motivation of the work presented in this Thesis is to further study these oscillation properties of tori and to investigate the occurrence of the runway instability of self-gravitating accretion tori by fully relativistic non-linear hydrodynamic simulations, we introduce in the following Sections of this Chapter the main physical concepts related to both of these issues while we postpone the discussion of numerical details for the following Chapters.

1.1 Basics of Thin Disc Oscillations

In this Section we discuss the basic properties of oscillations and waves in thin discs (note that do not include the effect of viscosity and radiative processes on the oscillations and refer to Kato, Fukue & Mineshige 1998; Ipser & Lindblom 1992; Perez et al., 1997; Silbergleit et al., 2001; Nowak & Wagoner 2001 for further details). As in stars, oscillations and waves of various types can be present in discs as a result of restoring forces acting on perturbations. Therefore, the nature of the oscillations can be explained in terms of the restoring force behind them. However, unlike in stars, the oscillation properties of discs have been investigated much less. There is though, an increasing interest in understanding this type of oscillatory motion since it can provide a better insight into the structure of the innermost regions of black hole accretion discs and also further information on the central compact object. Moreover, there have been recent observations of quasi-periodic behaviour in systems containing an accretion disc. For instance, the rapid X-ray variability observed in the spectra of low mass X-ray binaries with black hole candidate.

1.1.1 Classification of Disc Oscillations

In non-rotating fluid objects, the restoring force due to pressure gives rise to *acoustic waves* while if the restoring force is due entropy stratification the resulting waves are called *inertial gravity waves.* Additional oscillation modes will appear if new restoring forces are involved such as those due to magnetic fields, and in the case of accretion discs as a result of rotation (originating the so called *inertial oscillations*) and vertical gravitational fields (giving rise to the so called *corrugation waves*). We briefly explain these type of oscillations:

- **Radial oscillations**

  The *epicyclic frequency* plays a central role in understanding the radial oscillations of discs. Recall that if a particle rotating in a circular orbit around a central object is displaced radially from its equilibrium orbit while its angular momentum remains unchanged it will oscillate around the equilibrium circular orbit. The frequency of this radial motion is called the *radial epicyclic frequency* and the polar equivalent, the *polar epicyclic frequency* can be defined for motion out of the equatorial plane. In accretion discs, in absence of pressure gradients, the most significant restoring force is the centrifugal force which gives rise to inertial oscillations whose frequency is the radial epicyclic frequency. In the Newtonian case, the epicyclic frequency is given by

$$k_r^2 = 2\Omega\left(2\Omega + r\frac{d\Omega}{dr}\right), \tag{1.1}$$

where $\Omega(r)$ is the rotation law of the disc. We note that the radial distribution of the epicyclic frequency in Newtonian discs is quite different from the distribution in relativistic discs, in this latter case the radial distribution of the epicyclic frequency is not monotonic which is related to the origin of wave trapping in relativistic discs. When pressure gradients are present as for non-Keplerian discs, radial oscillations are often a combination of inertial and acoustic waves so that are often referred as to inertial-acoustic waves or *p-modes*. The p-modes of vertically integrated non-selfgravitating accretion tori have recently been investigated by Rezzolla et al. (2003b) through a local and a global linear perturbative analysis. Rezzolla et al. (2003b) obtained the relativistic radial epicyclic frequency for an extended fluid object in a Schwarzschild spacetime and showed that inertial oscillations in the perturbations of tori can be removed only in the special case of constant distribution of constant distribution of specific angular momentum.

- **Polar oscillations**

  When a fluid element of the disc plane is perturbed in the vertical direction a restoring force associated to the vertical component of the gravitational force acts to return the displaced fluid element into the equatorial plane, thus giving rise to oscillations in the vertical direction. These waves are often known as *corrugation waves* which, in the case of non-axisymmetric modes, are associated to the warping of discs.

- **Coupled oscillations**

  In general, in accretion discs vertical and horizontal oscillations are coupled so that, vertical oscillation induce a radial oscillatory motion and viceversa (Kato 2001).

1.1.2 Trapping of Radial Oscillations

Unlike the Newtonian radial epicyclic frequency, which increases monotonically inward, the radial epicyclic frequency for pointlike particles in the relativistic framework increases inwards until it reaches a maximum at a certain radius, depending on the rotation speed of the central object, and then decreases inwards (*cf.* in Fig. 2.1 we show the radial epicyclic frequency for different values of the black hole spin). In the case in which the central object is a Schwarzschild black hole, the radial epicyclic frequency has a maximum at $4r_s$, where $r_s = 2GM/c^2$ is the Schwarzschild radius and vanishes at $3r_s$. The wave propagation region in the radial direction for inertial-acoustic waves with frequency ω, is $\omega > k_r$, where k_r is the epicyclic frequency. The maximum in the epicyclic frequency implies that oscillations in the inner parts of the disc with frequency ω such that $\omega < k_{rmax}$ (*i.e.* regions inside the location of the epicyclic frequency maximum) will not be able to propagate outwards since the wave is reflected back at the point where $\omega = k_r$. The inner edge of the accretion disc acts also as a boundary so that waves can be partially reflected. Therefore, the innermost regions of discs may act as a wave trapping region. This type of trapping does not produce oscillation modes in harmonic relation. In non-Keplerian discs the trapping may occur through other mechanisms (Wagoner 1999).

1.2 The Runaway Instability

We have already mentioned that one of the important features of non-selfgravitating fluids orbiting around a black hole is the existence of a self-crossing equipotential surface, reminiscent of the Roche lobe in binary systems, with the point at which this surface crosses itself being referred to as the cusp. For a finite size torus filling its outermost closed equipotential, mass accretion onto the black hole is possible through its cusp which is located at the inner edge of the torus. As a result of the mass transfer to the black hole and therefore, its increase in mass, the location of the cusp changes. If the cusp moves deeper inside the torus, the mass accretion speeds up leading to the so called runaway instability. This instability was discovered by Abramowicz, Calvani & Nobili (1983) who found that relativistic tori with a constant specific angular momentum are unstable with respect to the accretion of mass through the cusp. In their investigations the gravitational potential of the central black hole was approximated with a pseudo-Newtonian potential (Paczyński & Witta 1980) and the self-gravity of the torus was included using Newtonian gravity. The investigations of the runaway instability continued with the work by Wilson (1984) who considered a Kerr metric for the black hole but neglected the self-gravity of the disc which was modelled with constant distribution of specific angular momentum. He found that under these conditions tori are stable to the instability since accretion transfers not only mass but also angular momentum. However, Khanna & Chakrabarti (1992) studied the existence of the instability modelling the gravity of the rotating black hole with a pseudo-Newtonian potential and including the self-gravity of the tori and found that tori are unstable.

We note that these investigations and the later work by Nishida et al. (1996); Daigne & Mochkovitch (1997); Abramowicz et al. (1998); Matsuda et al. (1998) and Lu et al. (2000) were based on stationary models and have provided only a partial answer to this issue. The results from these series of studies can be summarized as follows:

- Daigne & Mochkovitch (1997); Abramowicz et al. (1998) showed that a non-constant distribution of the angular momentum has an important stabilizing effect.
- Another stabilizing factor is the rotation of the central black hole which has been shown by Wilson (1984) and Abramowicz et al. (1998).
- On the other hand, the self-gravity of the torus tends to favor the occurrence of the instability (Khanna & Chakrabarti 1992; Nishida et al. 1996; Matsuda et al. 1998).
- Using a fully relativistic potential instead of a pseudo-Newtonian potential seems also to favor the instability (Nishida et al. 1996).

A further step forward to clarify whether the runaway instability may exist or not, has been the nonlinear general relativistic hydrodynamical simulations of non-selfgravitating tori performed by Font & Daigne (2002a,b), Zanotti et al. (2003) and Daigne & Font (2004). These authors have used an axisymmetric relativistic hydrodynamic evolution code to perform time-dependent simulations aiming to investigate the onset of the instability. In these studies the self-gravity of the tori was neglected and the spacetime evolution, *i.e.* the evolution of the black hole, was modelled as a sequence of exact stationary black holes of increasing mass and rotation speed. Thus, the increase in the black hole mass and spin was computed from the transfer of mass and angular momentum from the torus to the black hole. In particular, Font & Daigne (2002a) focused on the runaway instability of tori with constant angular momentum around a Schwarzschild black hole. They studied several models with different disc to black hole mass ratios and found that the runaway appears on a dynamical time scale (of less than 1s for the models investigated) when the mass of the black hole was allowed to increase due to the mass transfer from the torus. This was the first estimation of the timescale of this instability which was found to depend weakly on the disc to hole mass ratio. Zanotti et al. (2003) confirmed these results and found that the appearance of the instability does not depend on the way accretion is induced. The case in which tori have a non-constant angular momentum distribution was then studied by Font & Daigne (2002b) and Daigne & Font (2004) who performed dynamical evolutions of tori around a Kerr black hole. In agreement with results obtained with stationary studies their dynamical hydrodynamic simulations confirmed that the runaway instability may not occur when tori have a non-constant distribution of angular momentum. This has a simple explanation in terms of the appearance of an evanescent wave region in the inner parts of the disc when the distribution of angular momentum is non-constant (Rezzolla et al., 2003b). The final answer to this issue must come from numerical hydrodynamical simulations also evolving the spacetime and include the self-gravity of the disc, thus treating the black hole evolution in a fully consistent way.

Chapter 2

Axisymmetric Oscillations of Vertically Integrated Relativistic Tori in a Kerr Spacetime

2.1 Introduction

With the aim of assessing whether the onset of the runaway instability depends sensitively on the choice of initial conditions, Zanotti et al. (2003) carried out general relativistic hydrodynamic simulations of perturbed tori orbiting around a Schwarzschild black hole and shown that the instability may take place independently of the way the mass accretion is induced. In addition, the simulations have indicated how the introduction of perturbations triggers harmonic oscillations in the tori which could produce large variations of their mass quadrupole. In the case in which the torus is made of high-density matter (as in the case of a torus formed after a binary neutron star merger), these oscillations could then lead to the emission of gravitational waves with amplitudes comparable with those produced in a gravitational stellar-core collapse, thus making these objects promising sources of gravitational radiation even if the instability does not set in.

Together with the general relativistic hydrodynamic simulations, oscillation modes of geometrically thick relativistic discs can also be studied through perturbative analyses.

Clearly, this second approach is computationally less intensive and therefore, allows for a more detailed investigation of the parameter space. Using a linear perturbative approach, Rezzolla et al. (2003b; RYZ hereafter), have recently investigated the axisymmetric oscillation properties of relativistic tori in a Schwarzschild spacetime. To simplify the treatment and make it as analytical as possible, the tori were built with vertically integrated quantities, thus transforming the eigenvalue problem into a set of coupled ordinary differential equations. The tori were then modeled with a number of different non-Keplerian distributions of specific angular momentum. Overall, the perturbative analysis of RYZ confirmed the results obtained by Zanotti et al. (2003) through non-linear simulations, revealing that the oscillations found in the simulations correspond to *p*-modes and that the lowest-order eigenfrequencies must be in a sequence of small integers 2:3:4..., rather independently of the size and the specific angular momentum distribution of the tori. Furthermore, a detailed study of the eigenfunctions in RYZ has also provided a possible explanation for the numerical evidence that the runaway instability can be efficiently suppressed for tori with distributions of specific angular momentum that follow a power-law (Font & Daigne, 2002b; Daigne & Font 2004).

Our investigations extend to geometrically thick discs all of the relativistic discoseismology analyses carried so far for thin discs (Okazaki et al., 1987; Perez et al., 1997; Silbergleit et al., 2001; Kato, 2001, Rodriguez et al., 2002) and also the work of RYZ. Therefore, our study is devoted to both a local and a global perturbative analysis of axisymmetric modes of oscillation of relativistic tori in the background spacetime of a Kerr black hole. While the local analysis provides us with the dispersion relation for inertial-acoustic waves in relativistic non-Keplerian discs, the global approach provides us with the eigenfunctions and eigenfrequencies of the *p*-mode oscillations of the system. As in RYZ, we have here removed one spatial dimension from the problem by considering vertically integrated tori and have neglected the variations in the background spacetime produced by the perturbations (*i.e.* Cowling approximation, Cowling 1941). Also in this case, the solution of the eigenvalue problem is simplified considerably and reduces to the solution of second-order ordinary differential equations.

We also compare the linear perturbative approach applied to vertically integrated tori around Kerr black holes with non-linear hydrodynamic simulations of geometrically thick discs performed with a 2D general relativistic hydrodynamic code and we present estimates of the gravitational wave emission due to the oscillations of high density tori.

The oscillations of geometrically thick discs are important not only because they could produce intense gravitational radiation, but also because, in low-density discs, they may serve to explain the high-frequency quasi-periodic oscillations (HFQPOs) observed in low-mass X-ray binaries (LMXBs) containing a black hole candidate. In these systems, in fact, the X-ray luminosity is modulated quasi-periodically, giving rise to distinctive peaks in the power spectral density which, so far, have been found in sequences of small integers 2:3 (see Abramowicz and Kluźniak, 2001 for the intepretation of the results of Remillard et al., 1999 and Strohmayer, 2001; see Remillard et al., 2002, Homan et al., 2003 for further observational evidences). More recently and although with a much poorer statistics, the possible presence of a QPO structure has been suggested also in the power spectrum of the light curve of the two brightest X-ray flares from the Galactic Center black hole (Aschenbach et al., 2004).

Using the striking analogy between the results of the numerical simulations and the observations in LMXBs, Rezzolla et al. (2003a) have proposed a simple model that exploits the properties of p-mode oscillations in thick discs and accounts for the complex phenomenology observed for HFQPOs. It is interesting to note while such a configuration could be produced whenever an intervening process modifies the Keplerian character of the flow near the black hole, the numerical simulations of De Villiers et al. (2003) have now provided a more realistic clue to how these tori can be generated. Similarly, the recent model proposed by Giannios & Spruit (2004) suggests a simple way in which these p-mode oscillations could be excited. Both of these models were not available at the time the model by Rezzolla et al. (2003a) was proposed.

To further develop this model, in addition to the global perturbative analysis of axisymmetric modes of oscillation of relativistic tori in the background spacetime of a Kerr black hole we have also here considered whether a purely Newtonian description of physics could be sufficient to account for the observations. For studying this, we have also performed a global analysis of the axisymmetric oscillations of vertically integrated non-Keplerian discs in Newtonian physics. Our results indicate that no major *qualitative* differences emerge and that the most important features of p-modes in relativistic tori remain unchanged also in the corresponding Newtonian models, albeit with *quantitative* differences.

Hereafter, Greek indices are taken to run from 0 to 3 and the Latin indices i-n run from 1 to 3; unless stated differently, we will use units in which $G = c = M_\odot = 1$.

2.2 Relativistic Tori in a Kerr Spacetime: Assumptions and Equations

We will here assume that the torus does not contribute to the spacetime metric, which we will take to be that external to a Kerr black hole. Furthermore, since we are interested in the portion of the spacetime in the vicinity of the equatorial plane (*i.e.* for values of the spherical angular coordinate $|\theta - \pi/2| \ll 1$), we will write the Kerr metric in cylindrical coordinates $(t, \varpi, \phi, \theta)$ and retain the zeroth-order terms in the ratio (z/ϖ). In this case, the line element assumes the form (Novikov and Thorne 1973)

$$ds^2 = -\frac{\varpi^2 \Delta}{A} dt^2 + \frac{A}{\varpi^2}(d\phi - \omega dt)^2 + \frac{\varpi^2}{\Delta} d\varpi^2 + dz^2 \ , \tag{2.1}$$

where $A \equiv \varpi^4 + \varpi^2 a^2 + 2M\varpi a^2$, $\Delta \equiv \varpi^2 - 2M\varpi + a^2$ and $\omega \equiv 2Ma\varpi/A$. Here, M is the gravitational mass of the black hole and a/M is the Kerr parameter, so that the black hole angular momentum can be expressed as $J = aM$.

The basic equations to be solved to construct models in hydrostatic equilibrium are the continuity equation $\nabla_\alpha(\rho u^\alpha) = 0$ and the conservation of energy-momentum, $\nabla_\alpha T^{\alpha\beta} = 0$, where the symbol ∇ refers to a covariant derivative with respect to the metric (2.1). Here, $T^{\alpha\beta} \equiv (e + p)u^\alpha u^\beta + p g^{\alpha\beta}$ are the components of the stress-energy tensor of a perfect fluid, with u^α being the components of the 4-velocity, ρ the rest-mass density, e the energy density and p the pressure. It is also useful to introduce an orthonormal tetrad carried by the local stationary observer and defined by the one-forms with components

$$\begin{aligned} \boldsymbol{\omega}^{\hat{t}} &= \varpi\sqrt{\Delta/A}\,\mathbf{d}t \ , \qquad & \boldsymbol{\omega}^{\hat{\phi}} &= \sqrt{A}(\mathbf{d}\phi - \omega\mathbf{d}t)/\varpi \ , \\ \boldsymbol{\omega}^{\hat{z}} &= \mathbf{d}z \ , \qquad & \boldsymbol{\omega}^{\hat{\varpi}} &= \varpi/\sqrt{\Delta}\,\mathbf{d}\varpi \ . \end{aligned} \tag{2.2}$$

In this frame, the components of the four velocity of the fluid are denoted by $u^{\hat{\mu}}$ and the 3-velocity components are defined as

$$v^{\hat{i}} \equiv \frac{u^{\hat{i}}}{u^{\hat{t}}} = \frac{\omega^{\hat{i}}_{\alpha} u^{\alpha}}{\omega^{\hat{t}}_{\alpha} u^{\alpha}} \ , \qquad i = \varpi, z, \phi \ . \tag{2.3}$$

We consider the perfect fluid to follow a polytropic equation of state $p = k\rho^{\gamma}$, where k and $\gamma \equiv d\ln p/d\ln\rho$ are the polytropic constant and the adiabatic index, respectively. Next, being interested in a vertically integrated description of the torus, we introduce a vertically integrated pressure

$$P(\varpi) \equiv \int_{-H}^{H} p dz, \tag{2.4}$$

and a vertically integrated rest-mass density

$$\Sigma(\varpi) \equiv \int_{-H}^{H} \rho dz, \tag{2.5}$$

where $H = H(\varpi)$ is the local "thickness" of the torus. We further assume that P and Σ obey an "effective" polytropic equation of state

$$P = \mathcal{K}\Sigma^{\Gamma} \ , \tag{2.6}$$

so that $\mathcal{K}$ and $\Gamma \equiv d\ln P/d\ln\Sigma$ play the role of the polytropic constant and of the adiabatic index, respectively. As mentioned in RYZ, it is important to underline that (2.6) does not represent a vertically integrated polytropic equation of state since the polytropic exponent $\Gamma = \Gamma(\varpi)$ is now a function of the position inside the torus.

We enforce the conditions of hydrostatic equilibrium and axisymmetry (*i.e.* assume $\partial_t = 0 = \partial_\phi$) and simplify the equation of energy-momentum conservation to a Bernoulli-type form (Kozlowski et al., 1978)

$$\frac{\nabla_i p}{e + p} = -\nabla_i \ln(u_t) + \frac{\Omega \nabla_i \ell}{1 - \Omega\ell} \ , \tag{2.7}$$

where $\ell \equiv -u_\phi/u_t$ is the specific angular momentum (*i.e.* the angular momentum per unit energy). Using the only relevant component of Eq. (2.7), we construct the equilibrium model for a non-selfgravitating torus in the Kerr spacetime by integrating in the direction perpendicular to the equatorial plane both the left and right hand side of Eq. (2.7), obtaining

$$\frac{1}{E + P}\frac{dP}{d\varpi} = -\frac{M(1 - a\Omega)^2/\varpi^2 - \varpi\Omega^2}{\varpi^2\Delta/A - A(\omega - \Omega)^2/\varpi^2} \ , \tag{2.8}$$

where E is the vertically integrated energy density (*cf.* Eq. (2.4)).

We next perturb the hydrodynamical equations introducing Eulerian perturbations of the hydrodynamical variables with a harmonic time dependence of the type

$$\left(\delta V^{\hat{\varpi}}, \delta V^{\hat{\phi}}, \delta Q\right) \sim \exp(-\mathrm{i}\sigma t) \ , \tag{2.9}$$

where $\delta Q \equiv \delta P/(E+P)$ and where we have defined the vertically averaged velocity perturbations respectively as

$$\delta V^{\hat{\varpi}} \equiv \frac{1}{2H}\int_{-H}^{H} \delta v^{\hat{\varpi}} dz \ , \qquad \delta V^{\hat{\phi}} \equiv \frac{1}{2H}\int_{-H}^{H} \delta v^{\hat{\phi}} dz \ . \tag{2.10}$$

We assume that the Eulerian perturbations in the metric functions can be neglected, *i.e.* $\delta g_{ab} = 0$ (Cowling approximation; Cowling, 1941). While this condition does not hold true in general, it represents a very good approximation in the case of non-selfgravitating tori.

Introducing now the quantities

$$\delta U \equiv \mathrm{i}\delta V^{\hat{\varpi}} \ , \qquad \delta W \equiv \delta V^{\hat{\phi}} \ , \tag{2.11}$$

to eliminate the imaginary part from the system of equations and after a bit of straightforward algebra, we derive the following set of ordinary differential equations

$$\sigma\frac{\Delta}{\sqrt{A}}\delta U + \alpha\frac{\Delta}{\varpi^2}\delta Q' + \left[\frac{\Delta^{3/2}}{A}\left(\frac{A}{\varpi^2}\right)'\Omega - \frac{\Delta^{3/2}}{A}\left(\frac{A\omega}{\varpi^2}\right)' + 2\frac{\Delta^{3/2}}{\varpi^2}(\Omega-\omega)\frac{P'}{E+P}\right]\delta W = 0 \ , \tag{2.12}$$

$$\begin{aligned}\sigma\frac{\varpi^2\sqrt{\Delta}}{A}\delta W + \Bigg\{\Omega' + \Omega\left[\ln\left(\frac{A}{\varpi^2}\right)' + \frac{A^2\omega\omega'}{\varpi^4\Delta}\right] + \frac{A}{\varpi^2\Delta}\left[\left(\frac{\varpi^2\Delta}{A}\right)' - \left(\frac{A\omega^2}{\varpi^2}\right)' + \omega\left(\frac{A\omega}{\varpi^2}\right)'\right] \\ (\omega-\Omega) - \frac{A^2\omega'}{\varpi^4\Delta}\Omega^2 - \frac{\varpi^2}{A}\left(\frac{A\omega}{\varpi^2}\right)'\Bigg\}\frac{\Delta}{\sqrt{A}}\delta U + \frac{A\sigma\alpha}{\Delta\varpi^2}(\omega-\Omega)\,\delta Q = 0 \ ,\end{aligned} \tag{2.13}$$

$$\begin{aligned}\sigma\delta Q + \left\{\frac{\Delta}{\sqrt{A}}\left[\frac{P'}{E+P} + \widetilde{\Gamma}\left(\frac{1}{\varpi} - \frac{1}{2}\ln\left(\frac{r^2\Delta}{A} - \frac{A}{\varpi^2}(\omega-\Omega)^2\right)'\right)\right] + \widetilde{\Gamma}\left(\frac{\Delta}{\sqrt{A}}\right)'\right\}\delta U \\ - \left(\frac{\sigma\sqrt{\Delta}(\omega-\Omega)A\varpi^2}{\varpi^4\Delta - A^2(\omega-\Omega)^2}\right)\widetilde{\Gamma}\delta W + \widetilde{\Gamma}\frac{\Delta}{\sqrt{A}}\delta U' = 0 \ ,\end{aligned} \tag{2.14}$$

where $\alpha \equiv 1/(u^t)^2$, $\widetilde{\Gamma} \equiv \Gamma P/E + P$, and the index $'$ indicates a radial derivative.

Equations (2.12)–(2.14) are the ϖ- and ϕ-components of the perturbed relativistic Euler equations and the perturbed continuity equation, respectively. These are solved numerically for the eigenfrequencies and eigenfunctions of p-mode oscillations of an oscillating vertically integrated thick disc in a Kerr spacetime. Before discussing the solution of this eigenvalue problem, however, it is instructive to consider how wave-like perturbations propagate in the torus.

2.3 Perturbations of Relativistic Tori: a Local Analysis

We now present a local analysis of the axisymmetric oscillations modes of vertically integrated tori in a Kerr spacetime which will serve to clarify the relation between acoustic waves and other waves that play a fundamental role in fluids orbiting in a central potential, *i.e.* inertial (or epicyclic) waves. For this analysis we assume a harmonic radial dependence in the perturbed fluid quantities of the type $(\delta Q, \delta U, \delta W) \sim \exp(\mathrm{i}k\varpi)$, where k is the radial wavenumber so that the local wavelength is $\lambda = 2\pi/k$.

To make the system of equations simpler, we have removed from equations (2.12)–(2.14) those terms that are much smaller than the others. Details of these simplifications are discussed in the Appendix A. The linearized perturbation equations (2.12)–(2.14) resulting from this procedure can thus be written as a homogeneous linear system in matrix form

$$\mathbf{M}\left(k,\sigma\right) \begin{pmatrix} \delta U \\ \delta W \\ \delta Q \end{pmatrix} = 0 \ , \tag{2.15}$$

where $\mathbf{M}$ is the coefficient matrix given by

$$\mathbf{M}(k,\sigma) = \begin{pmatrix} \dfrac{\sigma\Delta}{\sqrt{A}} & \dfrac{\Delta^{\frac{3}{2}}}{A}\left[\Omega\left(\dfrac{A}{r^2}\right)' - \left(\dfrac{A\omega}{r^2}\right)' + \dfrac{2A\left(\Omega-\omega\right)P'}{r^2(E+P)}\right] & \dfrac{\mathrm{i}k\alpha\Delta}{r^2} \\ \dfrac{H\Delta}{\sqrt{A}} & \dfrac{\sigma r^2\sqrt{\Delta}}{A} & 0 \\ \dfrac{\mathrm{i}k\widetilde{\Gamma}\Delta}{\sqrt{A}} & 0 & \sigma \end{pmatrix}$$

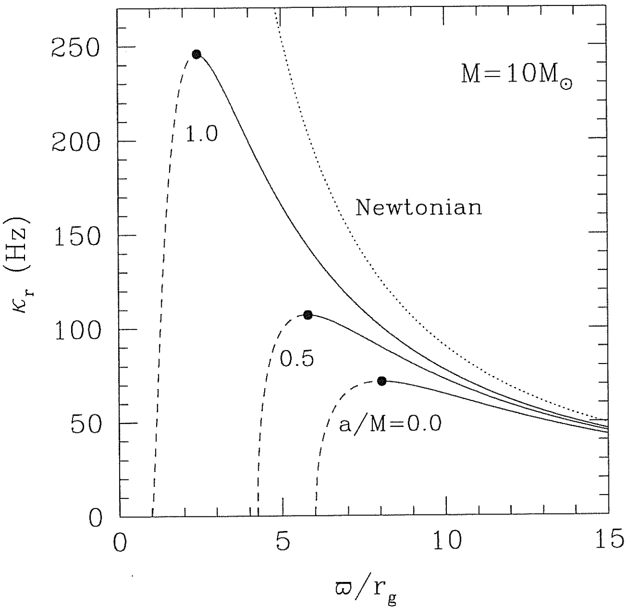

Figure 2.1: Radial epicyclic frequency for different values of the black hole spin. In each curve, a dashed line refers to the "increasing" branch (*i.e.* with $\kappa'_{\rm r} > 0$), while a solid line to the "decreasing" branch (*i.e.* with $\kappa'_{\rm r} < 0$). Indicated with solid circles are the locations of the maximum frequencies for each black hole spin, while the dotted line refers to the Newtonian values for the radial epicyclic frequency. The numerical values have been computed for a black hole with mass $M = 10M_\odot$ and the radial extents have been expressed in units of gravitational radii $r_g \equiv GM/c^2$.

(2.16)

The dispersion relation is then obtained by imposing the determinant of M to be zero, thus guaranteeing that a non-trivial solution to the system of equations (2.15) exists. After a bit of algebra one obtains the dispersion relation

$$\sigma^2 = \kappa_{\rm r}^2 + \frac{\Delta}{\varpi^2}\left[\frac{\varpi^2\Delta}{A} - \frac{A(\omega^2+\Omega^2)}{\varpi^2}\right]k^2c_s^2\ , \tag{2.17}$$

where $c_s \equiv \sqrt{dP/dE}$ is the relativistic sound speed within the vertically integrated disc and where the relativistic radial epicyclic frequency for an extended fluid object in a Kerr spacetime $\kappa_{\rm r}$ is defined as

$$\kappa_{\rm r}^2 \equiv \frac{\Delta D}{\varpi^2}\left[\left(\frac{A}{\varpi^2}\right)'\Omega - \left(\frac{A\omega}{\varpi^2}\right)' + \frac{2A}{\varpi^2}(\Omega-\omega)\frac{P'}{E+P}\right]\ .$$

(2.18)

Here, the quantity D is just a shorthand for

$$D \equiv \frac{A(\omega-\Omega)}{\varpi^2\Delta}\left[\left(\frac{\varpi^2\Delta}{A}\right)' - \left(\frac{A\omega^2}{\varpi^2}\right)' + \omega\left(\frac{A\omega}{\varpi^2}\right)'\right] + \Omega' - \frac{\varpi^2}{A}\left(\frac{A\omega}{\varpi^2}\right)' + \Omega\left[\ln\left(\frac{A}{\varpi^2}\right)' + \frac{A^2\omega\omega'}{\Delta\varpi^4} - \frac{\Omega A^2\omega'}{\Delta\varpi^4}\right] . \qquad (2.19)$$

Equations (2.17) and (2.18) include corrections coming from the rotation of the black hole and pressure gradients from the fluid distribution and reduce respectively to the dispersion relation and to the relativistic epicyclic frequency for an extended object obtained in RYZ for a Schwarzschild black hole (*cf.* Eqs. (42) and (43) of RYZ). When the motion is almost Keplerian, the pressure gradients are negligible and expression (2.18) reduces to the expression for the radial epicyclic frequency for point-like particles (Okazaki et al., 1987)

$$\left(\kappa_{\rm r}^2\right)_{\rm Kep} = \frac{M}{\varpi^3}\left[\frac{1-6M/\varpi \pm 8a\sqrt{M/\varpi^3} - 3a^2/\varpi^2}{(1\pm 8a\sqrt{M/\varpi^3})^2}\right] , \qquad (2.20)$$

where the ± sign distinguishes orbits that are corotating from those that counter-rotating relative to the black hole spin.

The behaviour of the radial epicyclic frequency (2.20) is shown in Fig. 2.1 where different curves refer to different black hole spins and where we consider corotating orbits only. For each curve, furthermore, a dashed line refers to the "increasing" branch of the epicyclic frequency (*i.e.* with $\kappa_{\rm r}' > 0$), while a solid line refers to the "decreasing" branch (*i.e.* with $\kappa_{\rm r}' < 0$). The solid circles indicate the locations of the maximum frequencies for each black hole spin and will be used subsequently in Fig. 2.3. Finally, the dotted line indicates the Newtonian radial epicyclic frequency which will be used for the discussion in Section 2.7.1. The numerical values refer to a black hole with mass $M = 10M_\odot$ and the radial extents have been expressed in units of gravitational radii $r_g \equiv GM/c^2$.

Overall, the dispersion relation (2.17) shows that the propagation of small perturbations in a fluid rotating around a Kerr black hole is characterized by two main features.

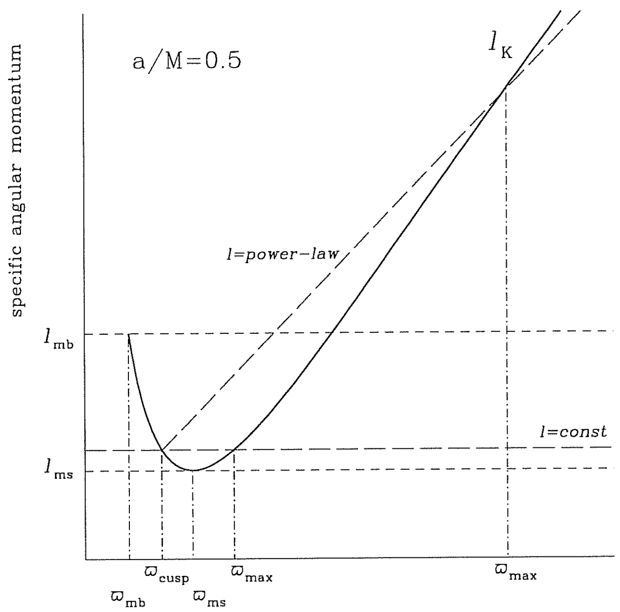

Figure 2.2: Schematic representation of the position of the relevant radii in the cases of "constant" and "power-law" distributions of specific angular momentum. In particular, while $\varpi_{\rm cusp}$ and $\varpi_{\rm max}$ indicate the positions of the cusp and of the rest-mass density maximum, $\varpi_{\rm mb}$ and $\varpi_{\rm ms}$ indicate the positions of the marginally bound and marginally stable orbits.

The first one is of purely acoustic nature (*i.e.* with $\sigma \propto kc_s$); the second of is of purely inertial nature (*i.e.* with $\sigma \propto \kappa_{\rm r}$) and is reminiscent of the oscillations that a particle orbiting in a central potential experiences when perturbed. For these reasons, the resulting waves are usually referred to as inertial-acoustic waves and the corresponding modes can be classified as p-modes. The determination of the eigenfrequencies and eigenfunctions of these modes will be discussed in the following Section.

2.4 Perturbations of Relativistic Tori: a Global Analysis

We now turn to a global analysis of the axisymmetric oscillation of relativistic tori in a Kerr spacetime by solving the system of equations (2.12)–(2.14) as an eigenvalue problem. In particular, the solution is found using a "shooting" method (Press et al., 1986) in which, once the appropriate boundary conditions are provided, two trial solutions are found, starting from the inner edge and outer edge of the disc respectively, and these are then matched at an intermediate point where the Wronskian of the two solutions is evaluated. This procedure is iterated until a zero of the Wronskian is found, thus providing a value for σ and a solution for δQ, δU and δW. The numerical methods employed here to solve the eigenvalue problem are the same as those discussed in RYZ, where a more detailed discussion can be found.

It is useful to briefly summarize how the background model for the torus is constructed as this will help clarifying the discussion of the results presented in the following Sections. First of all, a value of the black hole spin a/M is chosen and the distribution of the specific angular momentum $\ell = \ell(\varpi)$ is selected. The positions of the cusp and the maximum rest-mass density in the torus are then obtained by imposing that the specific angular momentum at these two points coincides with the Keplerian value (see Fig. 2.2 for a schematic view). The inner edge of the torus $\varpi_{\rm in}$ is determined by fixing the potential gap, $\Delta W_{in} = W_{\rm in} - W_{\rm cusp}$, defined as

$$\Delta W_{\rm in} = \ln[(-u_t)_{\rm in}] - \ln[(-u_t)_{\rm cusp}] - \int_{\ell_{\rm cusp}}^{\ell_{\rm in}} \frac{\Omega d\ell}{1-\Omega\ell}\,, \tag{2.21}$$

with $\Delta W_{\rm in} = 0$ corresponding to a torus filling its outermost equipotential surface. Next, the hydrostatic balance equation (2.8) is integrated from $\varpi_{\rm in}$ to the outer edge of the torus $\varpi_{\rm out}$, defined as the position at which $P = 0$. Sequences of tori having different radial extents for a given distribution of specific angular momentum and black hole spin can then be constructed by varying the potential gap ΔW_{in}. In such sequences, the tori will have the same rest-density maxima $\varpi_{\rm max}$.

Clearly, different distributions of specific angular momentum will produce tori with different positions of the cusp and of the maximum rest-mass density $\varpi_{\rm max}$. In order to investigate how the axisymmetric oscillations depend on these properties, we have constructed models with different distributions of specific angular momentum, taken to be either constant within the torus, or increasing outwards according to a generic power-law in radius (*cf.* Eq. (2.24)). The main properties of the various models considered are summarized in Table 2.1, where they are presented in terms of dimensionless quantities. A simple conversion of the dimensionless eigenfrequency $\widetilde{\sigma}$ and of the specific angular momentum $\widetilde{\ell}$

is obtained, for instance, through the following relations

$$\sigma = \tilde{\sigma}\left(\frac{M}{M_{\odot}}\right)^{-1}\left(\frac{GM_{\odot}}{c^2}\right)^{-1} c\ , \tag{2.22}$$

and

$$\ell = \tilde{\ell}\left(\frac{M}{M_{\odot}}\right)\left(\frac{GM_{\odot}}{c^2}\right) c\ . \tag{2.23}$$

2.4.1 Constant Specific Angular Momentum Tori

Fixed black hole spin

We first consider tori with a distribution of specific angular momentum that is constant in space, *i.e.* $\ell(\varpi)$ = const., not only because this choice is mathematically simpler to investigate, but also because it allows for a straightforward determination of the permitted range of equilibrium models. In this case, in fact, for a torus of finite size to exist, the value of the specific angular momentum must satisfy $\ell_{\rm ms} < \ell < \ell_{\rm mb}$, where $\ell_{\rm ms}$ and $\ell_{\rm mb}$ are the specific angular momenta of the marginally stable and of the marginally bound orbit, respectively. For a Schwarzschild black hole, $\ell_{\rm ms} = 3\sqrt{6}/2 \sim 3.67$ and $\ell_{\rm mb} = 4$, while they depend on the black hole spin for a Kerr black hole. Because the position of the rest-mass density maximum $\varpi_{\rm max}$ will depend on the specific value of ℓ chosen, it is then possible to define the range in which $\varpi_{\rm max}$ lies. In other words, all of the possible finite-size tori will have $(\varpi_{\rm max})_{\rm MIN} < \varpi_{\rm max} < (\varpi_{\rm max})_{\rm MAX}$, where we have defined $(\varpi_{\rm max})_{\rm MIN}$ as the value of $\varpi_{\rm max}$ when $\ell = \ell_{\rm ms}$, and $(\varpi_{\rm max})_{\rm MAX}$ as the value of $\varpi_{\rm max}$ when $\ell = \ell_{\rm mb}$. Clearly, $(\varpi_{\rm max})_{\rm MIN}$ also coincides with the location of the marginally stable orbit, while $(\varpi_{\rm max})_{\rm MAX}$ provides the position of the rest-mass density maximum for a torus whose outermost equipotential surface closes at infinity.

Furthermore, because in a Kerr spacetime the values of $\ell_{\rm ms}$ and $\ell_{\rm mb}$ will depend on the black hole spin a/M, it is possible to define the set of all the possible values that $\varpi_{\rm max}$ can assume for constant angular momentum tori constructed in a Kerr spacetime. This is shown as a shaded area in Fig. 2.3, where we have also plotted with solid lines the different values of $(\varpi_{\rm max})_{\rm MIN}$ and $(\varpi_{\rm max})_{\rm MAX}$ as the black hole spin is increased from 0 to 1 [1]. Also shown with a dashed line are the locations of the maximum of epicyclic frequency

---

[1] We have not considered here counterotating black holes, *i.e.* with $a < 0$.

Table 2.1: Main properties of the equilibrium models studied. From left to right the columns show: the black hole spin parameter,the type of specific angular momentum distribution, the constant coefficient ℓ_c and the power-law index q (*cf.* eq. 2.24), the position of the maximum density point $\varpi_{\rm max}$, the position of the inner and outer radii of the torus $\varpi_{\rm in}$ and $\varpi_{\rm out}$, the position of the maximum density point with respect to the epicyclic frequency curve. The potential gap at the inner edge of the torus $\Delta W_{\rm in}$ for models (C1a–P14) is -1.0×10^{-10}, while for (P15–P17), $\Delta W_{\rm in} = -1.0 \times 10^{-2}$, for P18, $\Delta W_{\rm in} = -5.0 \times 10^{-2}$ and for P19, $\Delta W_{\rm in} = -1.0 \times 10^{-1}$.

Model	a/M	$\ell(\varpi)$	$\ell_{\rm c}$	q	$\varpi_{\rm max}$	$\varpi_{\rm in}$	$\varpi_{\rm out}$	L	$\kappa_{\rm r}'(\varpi_{\rm max})$
C1a	0.5	const.	3.283	0.0	6.01	3.21	13.26	10.04	< 0
C1b	0.5	const.	3.313	0.0	6.29	3.13	18.04	14.92	< 0
C1c	0.5	const.	3.343	0.0	6.55	3.05	26.66	23.60	< 0
C1d	0.5	const.	3.373	0.0	6.81	2.99	47.78	44.79	< 0
C1e	0.5	const.	3.403	0.0	7.07	2.93	181.6	178.7	< 0
C2a	0.5	const.	3.193	0.0	5.00	3.65	6.330	2.680	> 0
C2b	0.5	const.	3.207	0.0	5.20	3.54	7.128	3.583	> 0
C2c	0.5	const.	3.223	0.0	5.39	3.45	8.079	4.627	> 0
C2d	0.5	const.	3.253	0.0	5.71	3.32	10.22	6.896	> 0
C3a	0.0	const.	3.704	0.0	7.0	5.22	8.572	3.354	< 0
C3b	0.1	const.	3.637	0.0	7.0	4.71	9.566	4.851	< 0
C3c	0.2	const.	3.573	0.0	7.0	4.24	11.18	6.946	< 0
C3d	0.3	const.	3.511	0.0	7.0	3.79	14.27	10.48	< 0
C3e	0.4	const.	3.452	0.0	7.0	3.36	22.40	19.04	< 0
C3f	0.5	const.	3.395	0.0	7.0	2.95	103.1	100.2	< 0
C4a	0.5	const.	3.167	0.0	4.5	3.99	4.821	0.828	< 0
C4b	0.6	const.	3.060	0.0	4.5	3.32	5.650	2.330	< 0
C4c	0.7	const.	2.960	0.0	4.5	2.70	7.879	5.173	< 0
C4d	0.8	const.	2.867	0.0	4.5	2.14	32.55	30.39	< 0
P10	0.0	power-law	3.381	0.06	9.0	5.02	15.92	10.90	< 0
P11	0.1	power-law	3.120	0.09	9.0	4.97	16.04	11.08	< 0
P12	0.2	power-law	2.999	0.10	9.0	4.64	18.61	13.97	< 0
P13	0.3	power-law	2.800	0.13	9.0	4.49	19.81	15.32	< 0
P14	0.4	power-law	2.738	0.13	9.0	4.04	26.52	22.48	< 0
P15	0.5	power-law	2.730	0.13	9.0	3.49	66.39	62.89	< 0
P16	0.6	power-law	2.649	0.14	9.0	3.74	197.7	194.0	< 0
P17	0.7	power-law	2.362	0.19	9.0	3.71	289.4	285.7	< 0
P18	0.8	power-law	2.272	0.20	9.0	4.84	29.12	24.28	< 0
P19	0.9	power-law	2.152	0.22	9.0	4.45	46.05	41.60	< 0

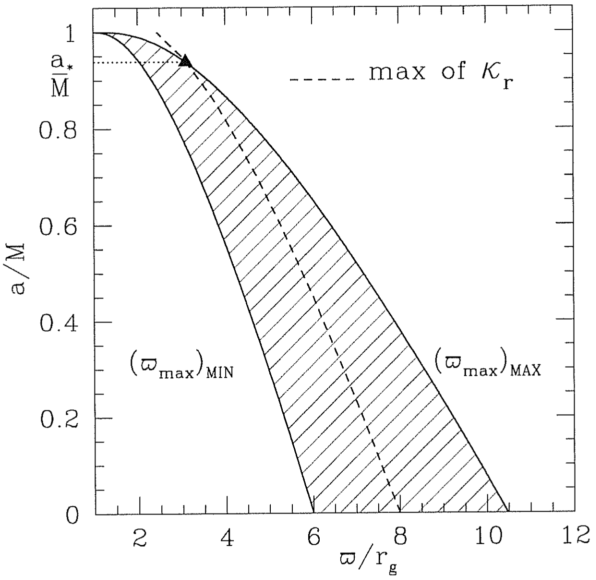

Figure 2.3: Possible locations of the rest-mass density maximum $\varpi_{\rm max}$ for tori with constant specific angular momentum distribution and for all possible black hole spins. The solid lines refer to the smallest and largest possible positions of $\varpi_{\rm max}$, while the dashed line indicates the locations of the maximum of epicyclic frequency κ_r (*cf.* the solid circles in Fig. 2.1).

for different black hole spins (*cf.* the solid circles in Fig. 2.1).

Note that for tori with constant specific angular momentum distributions around rapidly rotating black holes with spin parameter a/M larger than a_*/M (*cf.* Fig. 2.3), all of the possible values of $\varpi_{\rm max}$ will be located on the "increasing branch" of the epicyclic frequency (*i.e.* at positions where $\kappa_{\rm r}' > 0$). As a result, the closer the maximum density point is to the black hole horizon, the smaller the value of the epicyclic frequency at that point (*cf.* Eq. (2.20)). For rotations of the central black hole smaller than a_*/M, on the other hand, the models with $\varpi_{\rm max}$ in the "decreasing branch" of the epicyclic frequency (*i.e.* at positions where $\kappa_{\rm r}' < 0$) are also allowed together with those on the increasing branch. In this case, for any $a < a_*$, if the maximum rest-mass density point coincides with the location of the maximum point of the epicyclic frequency (*i.e.* at positions where $\kappa_{\rm r}' = 0$), the eigenfrequency of the fundamental mode for a given radial extent will have the largest value. The locus of these points is indicated with a dashed line in Fig. 2.3.

In order to investigate the dependence of the fundamental mode of oscillation on

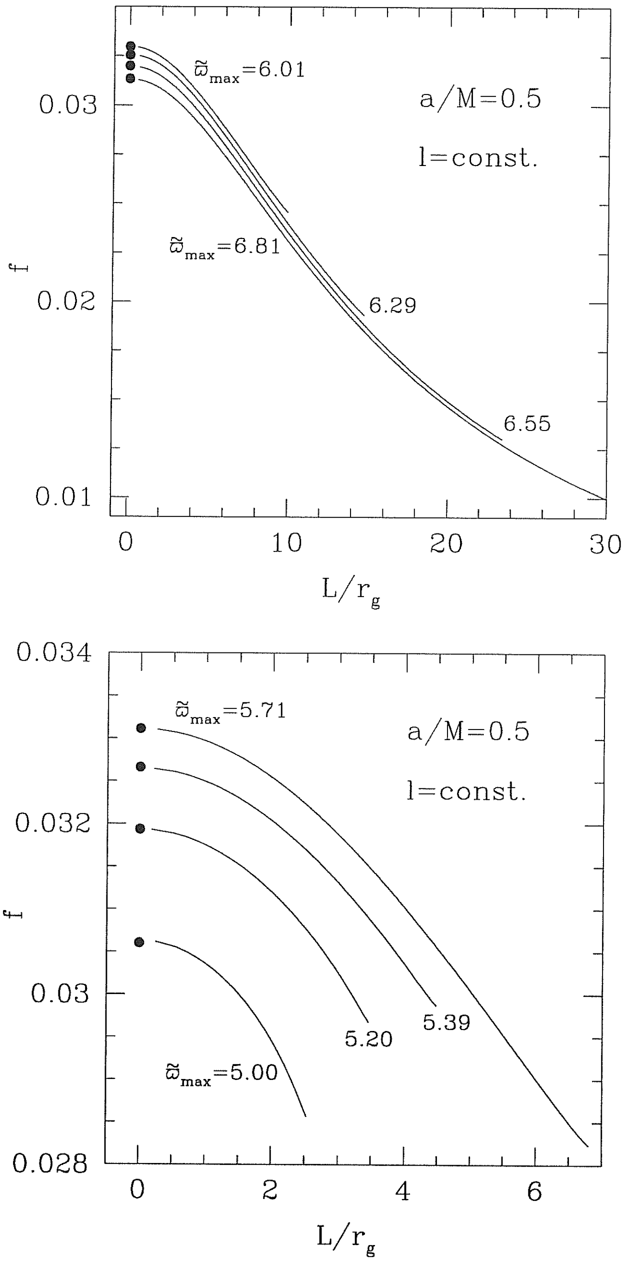

Figure 2.4: Eigenfrequencies for the fundamental mode of axisymmetric p modes for tori with a constant distribution of specific angular momentum. Each line corresponds to a sequence of tori having the same $\varpi_{\rm max}$ but different radial extents L. Both panels refer to a Kerr black hole with $a/M = 0.5$, but while the bottom panel has $\varpi_{\rm max}$ located in the increasing branch of the epicyclic frequency (*i.e.* $\kappa_{\rm r}' > 0$), the top one has $\varpi_{\rm max}$ located in the decreasing branch of the epicyclic frequency (*i.e.* $\kappa_{\rm r}' < 0$).

the position of the maximum rest-mass density, we have first considered sequences of tori having different radial extents $L \equiv \varpi_{\rm out} - \varpi_{\rm in}$. All sequences are built for the same value of the black hole spin, while each sequence is characterized by a specific value of $\varpi_{\rm max}$, which is chosen to be either on the increasing or on the decreasing branch of the corresponding epicyclic frequency. The results for a black hole spin $a/M = 0.5$ are summarized in the two panels of Fig. 2.4, which show the values of the eigenfrequency of the fundamental mode of oscillation f as a function of the disc radial extents L.

In the top panel, in particular, we show the results for models whose maximum rest-mass density is located on the decreasing branch of the radial epicyclic frequency. As expected for modes behaving effectively as acoustic waves trapped in a rotating fluid, the eigenfrequencies decrease like L^{-1} as the radial extent of the torus increases. Note also that, as was shown for tori orbiting around a Schwarzschild black hole, the eigenfrequencies of the fundamental mode tend to the values of the radial epicyclic frequency at $\varpi_{\rm max}$ as the radial dimension of the discs tends to zero. These results confirm the expectation that, as their size diminishes, the discs effectively behave as rings of particles in circular orbits and have as their characteristic frequency the epicyclic frequency at the maximum rest-mass density point.

Note also in the top panel of Fig. 2.4 that models with the same radial extent and different constant angular momentum distributions, *i.e.*, tori with different locations of $\varpi_{\rm max}$, have fundamental eigenfrequencies that become larger as the rest-mass density maximum approaches the black hole. This behaviour can be explained simply since the fundamental eigenfrequencies track the values of the epicyclic frequency and the latter increases for smaller radii as one moves along the decreasing branch.

The opposite behavior is observed in the bottom panel of Fig. 2.4, but in this case the maximum density point of all models is located on the increasing branch of the epicyclic frequency. As a result, models with the same radial extent have fundamental frequencies that become smaller as the rest-mass density maximum approaches the black hole. Therefore, for any given radial extent, the model with the largest fundamental-mode eigenfrequency will be the one with $\varpi_{\rm max}$ located at the maximum of the epicyclic frequency (*i.e.* along the dashed line in Fig. 2.3).

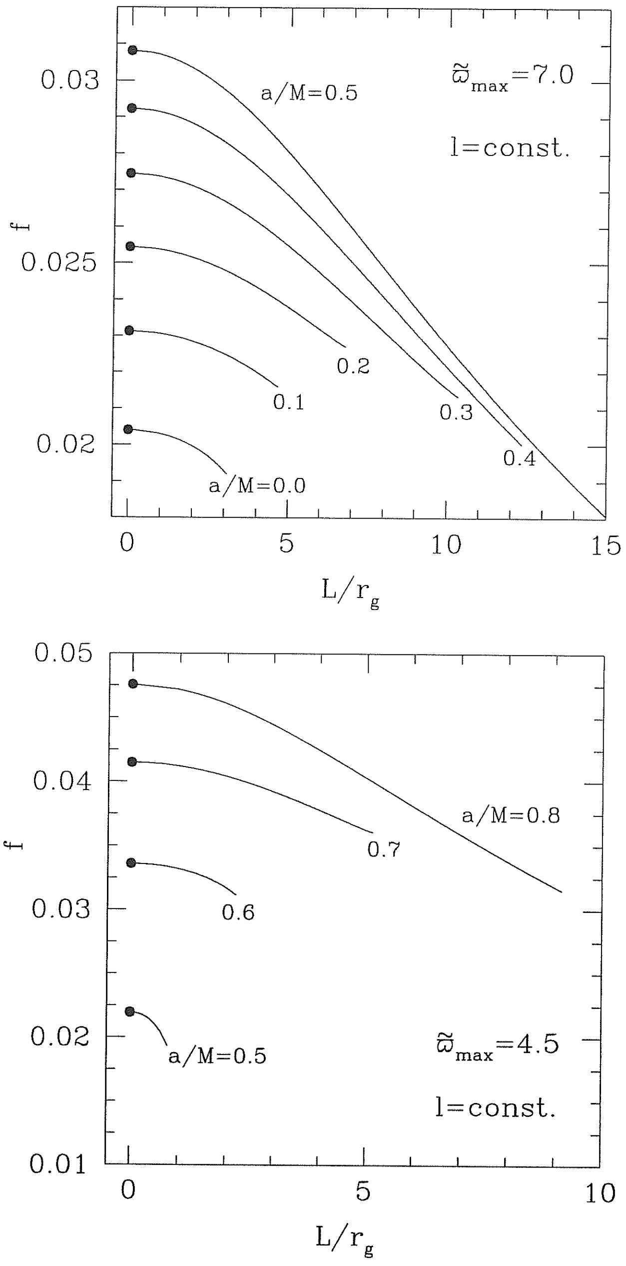

Figure 2.5: Eigenfrequencies for the fundamental mode of axisymmetric p-modes for tori with a constant distribution of specific angular momentum. Each line refers to a sequence of tori for the same black hole spin a/M, but having different radial extents L. In each panel, the sequences have been computed keeping fixed the position of $\varpi_{\rm max}$, which are however different according to whether the black holes are slowly rotating (top panel) or rapidly rotating (bottom panel).

Influence of the black hole spin

In order to investigate the influence of the spin of the central black hole on the axisymmetric oscillations, we have solved the eigenvalue problem for sequences of tori having the same location of $\varpi_{\max}$ but different black hole rotation rates.

We note that, in the case of constant specific angular momentum, it is not possible to construct sequences of tori having the same location of the rest-mass density maximum for all the possible values of the black hole spin. This is due to the fact that for any given $\varpi_{\max}$, the existence of marginally stable and of marginally bound orbit limits the range of values that a/M can assume. This is quite apparent in Fig. 2.3 where, for any chosen value of $\varpi_{\max}$, the black hole spin cannot span the whole range from 0 to 1.

Because of this constraint, we show in the top panel of Fig. 2.5 sequences of tori having the same value of $\varpi_{\max}/M = 7.0$ and black hole spins varying from $a/M = 0.0$ to $a/M = 0.5$. Clearly, these sequences share many of the properties discussed for Fig. 2.4 and, in addition, for any given radial size of the torus, the frequency of the fundamental mode will be larger for larger black hole spin. Indeed, this is what is expected, since the radial epicyclic frequency for a point-like particle $(\kappa_{\rm r})_{\rm Kep}$ increases monotonically with a for any value of ϖ (*cf.* Fig. 2.1). The same behaviour is observed also when $\varpi_{\max}/M = 4.5$, which allows for larger rotations rates of the black hole and is shown in the bottom panel of Fig. 2.5.

Harmonic sequence

An interesting and potentially important feature of axisymmetric p-mode oscillations of tori with constant specific angular momentum is that the lowest-order eigenfrequencies appear in a sequence 2:3:4..., with a good accuracy (*i.e.* within 10%) and rather independently of the details of the disc properties. This feature was first discovered through the fully non-linear numerical simulations of Zanotti et al. (2003) and subsequently confirmed through a perturbative analysis in a Schwarzschild spacetime in RYZ, and through additional independent numerical simulations (Kluźniak et al., 2004).

The existence of a harmonic relation for the lowest-order eigenfrequencies continues to exist also for tori with constant specific angular momentum in a Kerr spacetime and rather insensitively of the black hole spin. In Fig. 2.6 we show the ratio between the frequencies of the first overtone o_1 and the fundamental mode f for some representative tori with constant specific angular momentum (*cf.* Table 2.1). Different line types correspond to sequences that have been constructed with different locations of the rest-mass density maximum. All of the sequences span values of a/M from 0 to 0.8 without showing major qualitative differences.

Since it is not the result of a mathematical constraint but, rather, the consequence of a global mode of oscillation, the 2:3 ratio between the fundamental mode and its first overtone is satisfied with an accuracy that is in general within 10%, but is, nevertheless, not exact. A number of different elements can contribute to a deviation from the exact 2:3 ratio and the results of our calculations show that conditions such as the size of the disc, the location of the rest-mass density maximum, the black hole spin, the distribution of specific angular momentum, or the equation of state considered, can all influence this departure. Note also that in Fig. 2.6 some of the models (*e.g.* C4b and C3a) appear to have a rather large variation in the ratio o_1/f. It should be recalled, however, that these tori exist only over a very small range in the radial extent L (either because of the high value of the specific angular momentum or because of the large spin of the black hole). Being trapped in such small tori and rather close to the black hole horizon where the angular velocity is larger, the p-mode oscillations will be particularly sensitive to variations of the radial size.

Another interesting feature of the lowest-order eigenfrequencies is that, for any given black hole rotation speed, their ratio tends to a single value $o_1/f \sim 1.52$ as the size of the tori tends to zero (*cf.* Fig. 2.6). This is in good qualitative agreement with what was found in the perturbative analysis of slender tori (Blaes 1985), where the dispersion relation for generic perturbations of Newtonian slender tori having constant distributions of specific angular momentum, was derived (*cf.* Eq. (1.8) of Blaes 1985, with $j = 1$, and $|k| = 0$).

2.4.2 Non-Constant Specific Angular Momentum Tori

We next investigate axisymmetric p-modes in tori with non-constant distributions of specific angular momentum. In this case the problem is not very clearly defined since

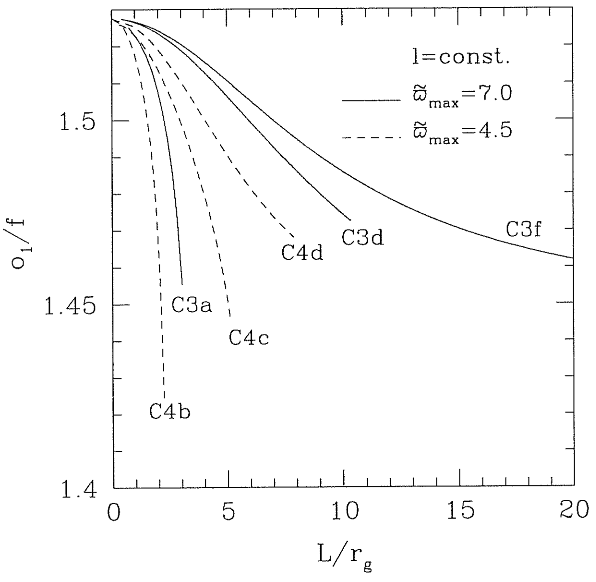

Figure 2.6: Ratio of the first overtone and the fundamental mode of oscillation for tori with constant specific angular momentum distributions. The different sequences refer to the different models described in Table 2.1, with the solid lines referring to $\varpi_{\rm max} = 7.0\, r_g$ and the dashed ones to $\varpi_{\rm max} = 4.5\, r_g$.

there is no obvious angular momentum distribution to specify. The first guide in the infinite possible choices is that they should correspond to stable fluid configurations. While in Newtonian theory one can make use of the simple Rayleigh stability criterion for rotating inviscid fluids $d\ell/d\varpi \geq 0$ (Tassoul 1978), the situation in a general relativistic framework is more complex. In particular, the condition of stability requires that, for the perfect fluids considered here, the gradient of the specific angular momentum must never point toward the interior of the quasi-circular level surfaces of ℓ (Seguin 1975, Abramowicz and Prasanna 1985). Because of this, we have used a simple prescription for the specific angular momentum in which it increases outwards with a power-law distribution of the type

$$\widetilde{\ell} = \ell_c \varpi^q \ , \tag{2.24}$$

where both ℓ_c and q are positive constants (*cf.* Table 2.1 for the different values used).

Following the procedure presented in the previous Section, we have constructed tori by selecting the angular momentum distribution such that the position of the cusp is always located between the marginally bound and the marginally stable orbits. Note that, in

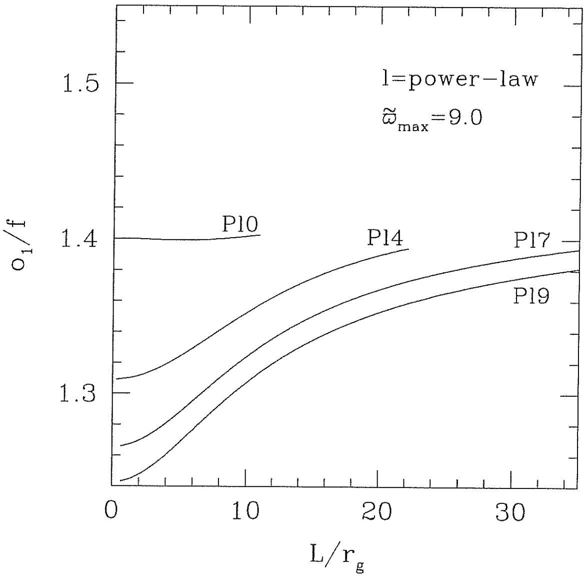

Figure 2.7: Ratio of the first overtone and the fundamental mode of oscillation for tori with a power-law distribution of specific angular momentum. The different sequences distinguish different choices of the index q, but all refer to the same value for ℓ_c (*cf.* Table 2.1).

principle, this is not the only possible choice. Non-constant distributions of specific angular momentum, in fact, allow for the construction of tori having the cusp at radii larger than the position of the marginally stable orbit. In such tori, matter lost through the cusp as a result of small perturbations would be able to find new stable circular orbits and, as a result, the accretion onto the black hole will require mechanisms other than simple perturbations in the flow. Here, we have not investigated the properties of these discs whose dynamics, however, has been considered in detail by Zanotti et al. (2004).

Overall, the solutions for tori with non-constant distributions of specific angular momentum share qualitative similarities with those found when ℓ = const. In particular, the main properties of the p-mode oscillations in this case can be summarized as follows: Firstly, the eigenfrequencies depend on the location of the rest-mass density maximum $\varpi_{\rm max}$ and on whether the latter is located on the increasing or decreasing branch of the radial epicyclic frequency. Secondly, all eigenfrequencies tend to the radial epicyclic frequency at the location of $\varpi_{\rm max}$ in the limit of small tori. Thirdly, as the result of the presence of an *evanescent-wave* region (see RYZ for a detailed discussion), the eigenfunctions become

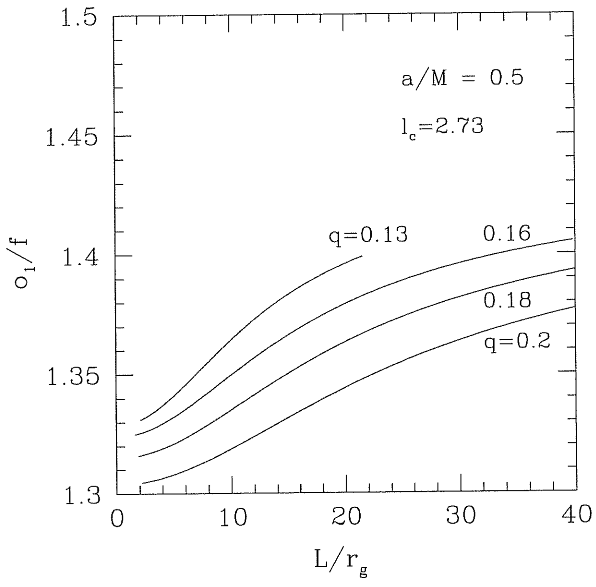

Figure 2.8: Ratio of the first overtone to the fundamental mode shown as a function of the tori radial extent of the torus L. The tori are modelled with a power-law distribution of specific angular momentum and the different lines refer to different choices of the index q, but all assume the same value of $\ell_c = 2.73$.

vanishingly small at the inner edge of the disc, while they do not do so at the outer edge. Finally, for any sequence built with fixed $\varpi_{\rm max}$, the eigenfrequencies increase as the spin of the black hole is increased.

Despite these similarities, a difference does emerge when investigating non-constant angular momentum tori. In this case, in fact, the ratio between the first overtone and the fundamental frequency of oscillation o_1/f has a behaviour which is more complex than the one found when $\ell =$ const. In particular, it depends not only to the position of $\varpi_{\rm max}$, but also to the values on ℓ_c and q, as well as to those on a/M. Most importantly, while the eigenfrequencies remain in a harmonic sequence for sufficiently large discs, departures from a 2:3 ratio can be observed for very small discs. This is shown in Fig.2.7, where the o_1/f ratio is plotted for sequences of models orbiting around central black holes rotating at different rates and having different distributions of specific angular momentum (see Table 2.1 for the model descriptions). In all the cases considered, however, the departure from a 2:3 ratio is less than 20%.

Table 2.2: Fundamental properties of the initial models. From left to right the columns show: the name of the model, the black hole spin parameter, the power-law index q of the angular momentum distribution, the polytropic constant κ, the inner and the outer radius of the tours, r_{in} and r_{out}, the equatorial size of the torus L, the rest-mass density at the maximum rest-mass density point and the average rest-mass density. For all models considered the mass of the black hole is $M = 2.5M_{\odot}$.

Model	a	q	κ	r_{in}	r_{out}	L	ρ_{max}	$\langle\rho\rangle$
A1a	0.0	0.2	1.41×10^{13}	6.824	17.118	10.29	1.56×10^{13}	3.26×10^{12}
A2a	0.0	0.2	3.50×10^{13}	6.498	21.485	14.98	6.45×10^{12}	1.14×10^{12}
A3a	0.0	0.2	7.02×10^{13}	6.244	27.089	20.84	2.97×10^{12}	4.31×10^{11}
A4a	0.0	0.2	1.23×10^{14}	6.035	34.767	28.73	1.53×10^{12}	1.69×10^{11}
B1a	0.7	0.2	3.61×10^{13}	3.746	12.149	8.40	3.19×10^{13}	5.69×10^{12}
B2a	0.7	0.2	7.12×10^{13}	3.607	15.356	11.75	1.55×10^{13}	2.28×10^{12}
B3a	0.7	0.2	1.26×10^{14}	3.492	19.789	16.29	7.89×10^{12}	8.79×10^{11}
B4a	0.7	0.2	2.08×10^{14}	3.395	26.400	23.00	4.09×10^{12}	3.16×10^{11}
B5a	0.7	0.1	4.28×10^{12}	3.412	5.779	2.367	5.52×10^{14}	1.25×10^{14}
B6a	0.7	0.1	1.86×10^{13}	3.230	7.202	3.97	1.57×10^{14}	3.37×10^{13}
B7a	0.7	0.1	4.60×10^{13}	3.103	8.880	5.77	6.72×10^{13}	1.26×10^{13}
B8a	0.7	0.1	9.05×10^{13}	3.004	11.032	8.03	3.36×10^{13}	5.16×10^{12}
B9a	0.7	0.1	1.58×10^{14}	2.922	13.983	11.06	1.80×10^{13}	2.16×10^{12}
C1a	0.9	0.2	3.62×10^{13}	2.611	8.270	5.66	9.38×10^{13}	1.69×10^{13}
C2a	0.9	0.2	7.16×10^{13}	2.519	10.459	7.94	4.58×10^{13}	6.74×10^{12}
C3a	0.9	0.2	1.26×10^{14}	2.443	13.500	11.05	2.37×10^{13}	2.69×10^{12}
C4a	0.9	0.2	2.09×10^{14}	2.379	18.064	15.68	1.22×10^{13}	9.50×10^{11}
A1b	0.0	0.2	1.28×10^{9}	6.824	17.118	10.29	9.25×10^{12}	3.22×10^{12}
A1c	0.0	0.2	9.82×10^{4}	6.824	17.118	10.29	7.18×10^{12}	3.21×10^{12}
B1b	0.7	0.2	2.12×10^{13}	3.746	12.149	8.40	1.57×10^{14}	2.83×10^{13}
B1c	0.7	0.2	4.56×10^{13}	3.746	12.149	8.40	1.58×10^{13}	2.85×10^{12}

Finally, note that, as the size of the discs tends to zero, the ratios do not tend to the same value, as was the case for constant specific angular momentum tori but, rather, to a value that depends on the index q of the power-law. This is shown in Fig. 2.8, where we illustrate results for sequences of tori with the same ℓ_c but different indices q, built around the same Kerr black hole with $a/M = 0.5$. Also in this case, a closer agreement with a harmonic relation between the lowest-order eigenfrequencies is recovered for sufficiently large discs.

2.5 Comparisons with Non-linear Dynamical Studies

Additional information on the axisymmetric oscillation modes of tori around black holes can be obtained from general relativistic non-linear hydrodynamic simulations of axisymmetric relativistic tori. In order to compare our linear perturbative approach with hydrodynamic simulations, we have computed the eigenfrequencies and eigenfunctions for several models and then compared with results obtained from simulations of these tori carried out with the evolution code described by Zanotti et al. (2003). We note that these numerical simulations have been performed in 2D using spherical polar coordinates and therefore, no approximation on the structure of the tori is made, *i.e.* we do not make use of the vertical integrated description of the tori for the hydrodynamical simulations. We refer to Zanotti et al. (2004) for a detailed explanation of these non-linear simulations and here, we focuss on the comparison of both approaches. For this purpose we have calculated the Fourier transforms of the time evolution of the L_2 norm of the rest-mass density for all models, defined as $||\rho||^2 \equiv \sum_{i=1}^{N_r} \sum_{j=1}^{N_\theta} \rho_{ij}^2$. As this is a global quantity it is particularly useful for comparisons with the results of the eigenvalue problem in the linear perturbative analysis.

The models we have considered for this comparison between the linear perturbative analysis and the non-linear hydrodynamic simulations are listed in Table 2.2, we note that hereafter we use the label for the models as given in this table (*i.e.* in Table 2.2 and not Table 2.1). These models consist of relativistic tori filling their outermost closed equipotential surface and thus have the inner radius coinciding with the position of the cusp, *i.e.* $r_{\text{in}} = r_{\text{cusp}}$. These models have been divided into three classes named A, B and C according to whether the tori orbit around a black hole with spin parameter $a = J/M^2$ of 0.0, 0.7 or 0.9, respectively. All of the models but two (*i.e.* B1b and B1c) have a torus-to-hole mass ratio $M_{\text{t}}/M = 0.1$. Similarly, only two models (*i.e.* A1b and A1c) have been built with an adiabatic index γ different from 4/3. More specifically, models B1b and B1c have mass ratios $M_{\text{t}}/M = 0.5$ and $M_{\text{t}}/M = 0.05$ respectively, while models A1b and A1c have polytropic index $\gamma = 5/3$ and $\gamma = 2$, respectively.

In general, all of the computed spectra consist of a fundamental mode f and of a

Table 2.3: Frequency ratio o_1/f as extracted from the power spectra of the L_2 norm of the rest mass density (second column) and as computed from the solution of the eigenvalue problem (third column).

Model	$(o_1/f)_{num}$	$(o_1/f)_{linear}$
A1a	1.30	1.26
A2a	1.32	1.30
A3a	1.36	1.33
A4a	1.36	1.36
B1a	1.31	1.28
B2a	1.39	1.31
B3a	1.39	1.34
B4a	1.31	1.37
B6a	1.33	1.28
B7a	1.37	1.32
B8a	1.36	1.36
B9a	1.40	1.38
C1a	1.30	1.25
C2a	1.32	1.29
C3a	1.36	1.32

series of overtones. Among these overtones, one always appears at twice the fundamental frequency, while another one (identified as the first overtone o_1) is usually located between f and $2f$. Since the ratio o_1/f can be computed with good accuracy from the spectra, we compare it with the ratio between the two first eigenfrequencies computed with the linear perturbative analysis. This comparison is reported in Table 2.3 which shows the values of o_1/f computed using the two approaches for most of the models we have considered. For few of the models, such as B5a and C4a, it was not possible to identify the mode o_1 unambiguously, and they have not been reported in this table. For all models that allowed a clear identification, the agreement with the prediction of the linear perturbative approach is very good, with differences of $\sim 5\%$ at most.

Since the excitation of a particular overtone depends sensibly on the choice of the initial perturbation, we can excite a specific mode by perturbing the equilibrium model with the corresponding eigenfunctions for the radial velocity and rest-mass density of the vertically integrated model which are calculated by the perturbative analysis. Exploiting this possibility, we have investigated in detail the dynamics of model C1a and have considered initial data consisting either on generic perturbations in the radial velocity or in the rest-mass density (or in both), or on specific perturbations obeying the eigenfunctions for the velocity and the rest-mass density for the o_1 overtone. The results of this investigation are shown in Fig. 2.9, which shows the power spectra of the L_2 norm of ρ for the three different initial perturbations. We note that the two generic initial perturbations, represented by a global perturbation in the radial velocity (solid line) and by a global perturbation in the rest-mass density (dotted line), are less efficient in exciting the mode o_1 than when its mode eigenfunction is used (dashed line). In the latter case, the power channelled in that mode increases by a factor ~ 20 with respect to when a global perturbation in the radial velocity is used and by a factor ~ 5 with respect to when a global perturbation in the rest-mass density is used.

We note that exciting overtones above o_1 is increasingly difficult. The tests performed using the eigenfunctions of the mode o_2, for instance, could not provide a clear signature of the excitation of this particular mode, in contrast with the mode o_1. We believe this is probably due to the approximation made in the linear perturbative approach which treats thick discs as vertically integrated objects. While we expect this approximation to be a satisfactory one for the lower-order modes, it turns increasingly less accurate as the mode number increases.

In Fig. 2.9 we also note the presence of a mode overtone at twice the fundamental frequency, a fact which turns out to be very general for all the initial models of our sample. It was shown by RYZ through a linear analysis that the eigenfrequencies of p-modes oscillations in thick discs with a constant distribution of specific angular momentum appear in a harmonic sequence 2:3:4.... Since this same sequence was also found in the non-linear numerical simulations carried out by Zanotti et al. (2003), it was natural to interpret this overtone at twice the fundamental frequency as the mode o_2, for which $o_2/f = 2$. However, on the light of the present results (*i.e.* the difficulty to excite the mode o_2 in the numerical simulations using the corresponding eigenfunctions as a perturbation) and since our investigations using the perturbative analysis have shown that p-modes in thick discs with more generic angular momentum distributions can show deviations from the simple sequence 2:3:4..., we believe that the identification of the mode at twice the fundamental frequency

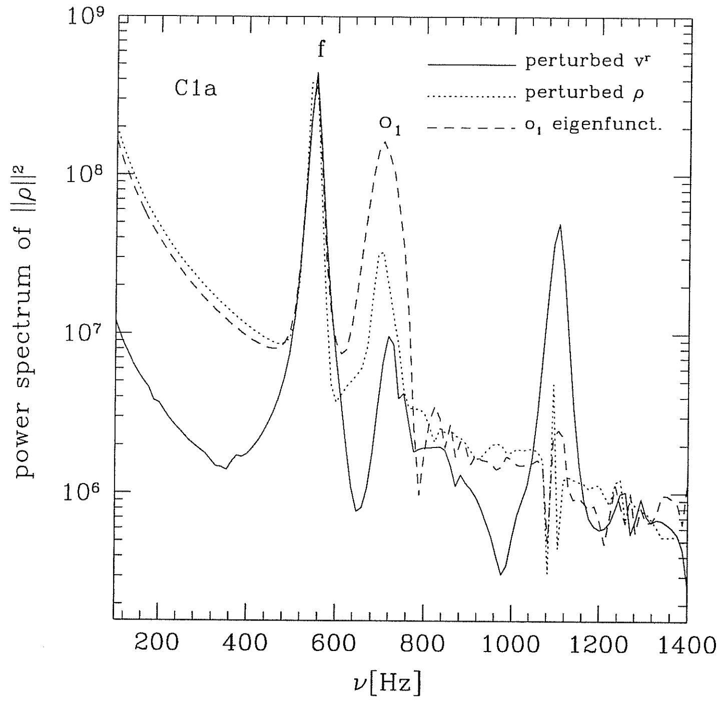

Figure 2.9: Power spectra of the L_2 norm of the rest-mass density for model C1a. The different lines refer to different initial perturbations: the solid line corresponds to an initial perturbation given by a parametrized spherically symmetric radial velocity, the dotted line to a global initial perturbation in the density, and the dashed line to an initial perturbation given by the eigenfunction of mode o_1. Vertical units are arbitrary and values have been rescaled in order to match the power of the fundamental frequency.

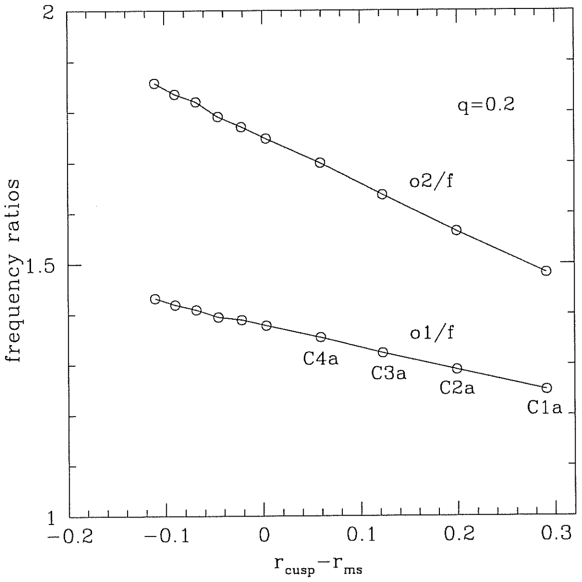

Figure 2.10: Ratio of overtones as computed through the linear analysis. The ratios o1/f and o2/f approach 3/2 and 2, respectively, as the cusp of torus penetrates deeper in the potential well.

with the mode o_2 requires more care. This feature is shown in Fig. 2.10. This figure shows for several models the frequency ratios o_1/f and o_2/f as a function of the penetration of the inner radius of the disc in the black hole potential well. We have computed these ratios with the linear perturbative code. Four of the models displayed in this figure belong to the sample of models that have been simulated numerically with the hydrodynamics code (C1a, C2a, C3a, C4a). As it is clear from the figure, both o_1/f and o_2/f differ from 3/2 and 2, values which they approach only in the limit of a torus penetrating deeply in the potential well. Furthermore, while the spectra obtained from the numerical simulations show a clear peak at the position predicted by the liner analysis for the mode o_1, it is difficult to find a peak at the position predicted by the perturbative code for the o_2 overtone.

A plausible interpretation of the peak at $2f$ is that it does not correspond to the o_2 overtone (which has too little power to be distinguished in the power spectra) but, rather, that it is the result of a non-linear coupling effect. It is, in fact, a general property of non-linear systems that of showing non-harmonic oscillations (i.e. linear combinations of their normal modes of oscillations) so that if the system has eigenfrequencies ω_i, the non-linearity of the equations will also produce modes at frequencies $\omega_i \pm \omega_j$ (*cf.* Landau & Lifschitz 1976, §28). Furthermore, the non-linear overtones where most of the power could be concentrated are the ones with eigenfrequencies $n \times f$, although modes with frequencies $n \times f + m \times o_1$ are also expected (here both n and m are integers). This behaviour seems confirmed in the power spectra of models B1a, B6a and C1a which show, besides the fundamental, also a peak at $f + o_1$.

This comparison between the results of the non-linear numerical simulations and those coming from the linear perturbation analysis indicate that the fundamental mode f and its first overtone in the numerical simulations do represent the two first p-modes of the system and that these are in ratio o_1/f close to 1.5, with deviations that are always smaller than $\sim$ 15%. Additional p-modes are also probably excited in the simulations but the corresponding power is too little to be visible in the power spectra, which instead always show overtones at integer multiples of the fundamental frequency (most notably at $2f$) and that are the result of non-linear coupling effects. It is useful to stress that this is a feature of tori with non-constant distribution of specific angular momentum and that a pure overtone $o2$ at twice the fundamental frequency is instead present in tori with constant distribution of specific angular momentum.

2.6 Gravitational Wave Emission

The oscillating behaviour of the perturbed tori that we have investigated in the previous Section is responsible of significant changes of the quadrupole moment of these sources. When the tori are compact enough and dense enough (e.g. when they are produced through binary neutron star mergers) the changes of the quadrupole moment result in the emission of potentially detectable gravitational radiation. In Zanotti et al. (2003) it was shown that the amount of energy that can be radiated in this way from perturbed high density tori can indeed be very high, with resulting signal-to-noise (S/N) ratios comparable or larger than those expected from the burst signal associated with the bounce in the collapse of the core of massive stars (Müller et al. 2004). This property is closely related to the toroidal topology of these objects, which have their maximum rest mass density away from the origin and thus have intrinsically high quadrupole moments and significant time variation of the latter. In the following we examine the issue of the gravitational wave emission from non-constant angular momentum tori orbiting around Kerr black holes.

The procedure for computing the gravitational wave emission is the same presented in Zanotti et al. (2003) and it is based on the use of the Newtonian quadrupole approximation. In particular, the time evolution of the wave amplitude $A^{\rm E2}_{20}$, which is the second time derivative of the mass quadrupole moment, is first computed through the "stress formula" (Finn 1989) as

$$\begin{aligned} A^{\rm E2}_{20} = k\int\rho\Big[& v_r v^r(3z^2-1)+v_\theta v^\theta(2-3z^2)-v_\phi v^\phi \\ & -6z\sqrt{(v^r v_r)(v_\theta v^\theta)(1-z^2)}-r\frac{\partial\Phi}{\partial r}(3z^2-1) \\ & +3z\frac{\partial\Phi}{\partial\theta}\sqrt{1-z^2}\Big]r^2{\rm d}r{\rm d}z\ , \end{aligned} \tag{2.25}$$

where $k = 16\pi^{3/2}/\sqrt{15}$, $z \equiv \cos\theta$ and Φ is the gravitational potential, approximated to the first Post-Newtonian order as $\Phi = (1 - g_{rr})/2$. The transverse traceless (TT) wave amplitude is then computed as (Zwerger & Müller 1997)

$$h^{TT}(t) = F_+\left(\frac{1}{8}\sqrt{\frac{15}{\pi}}\right)\frac{A^{\rm E2}_{20}}{R}\ , \tag{2.26}$$

where R is the distance to the source and where the detector's beam pattern function, $F_+ = F_+(R,\theta,\phi)$, is set to one as if optimal conditions of detectability were met. In order to investigate the possibility that pulsating relativistic tori can be effectively detected by the interferometric instruments presently in operation or under construction, we have computed the signal-to-noise ratio with respect to LIGO I, Advanced LIGO, and VIRGO. For doing this we need an estimate of the frequency where most of the gravitational wave emission is channelled, and this is provided by the *characteristic frequency* f_c, which is a detector dependent quantity. If the detector has a power spectral density $S_h(f)$, then the characteristic frequency is given by (Thorne 1987)

$$f_c \equiv \left[\int_0^\infty \frac{\langle|\tilde{h}(f)|^2\rangle}{S_h(f)} f df\right]\left[\int_0^\infty \frac{\langle|\tilde{h}(f)|^2\rangle}{S_h(f)} df\right]^{-1}\ , \tag{2.27}$$

where $\langle|\tilde{h}(f)|^2\rangle$, which is an average over randomly distributed angles of the Fourier transforms $\tilde{h}(f)$ of $h^{TT}(t)$, has been approximated as $\langle|\tilde{h}(f)|^2\rangle \simeq |\tilde{h}(f)|^2$. Strictly related to the

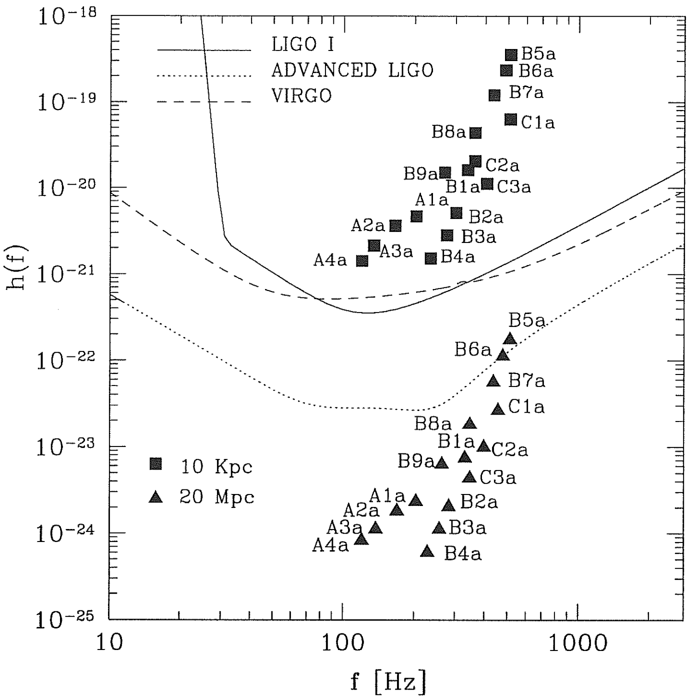

Figure 2.11: Characteristic wave amplitudes for the tori models of Table 2.1, computed at a galactic distance of 10Kpc and at an extra-galactic distance of 20Mpc with respect to the strain noise of LIGO I and Advanced LIGO, respectively. The strain noise of VIRGO is also reported for comparison.

characteristic frequency is the characteristic amplitude, that gives a typical measurement of the gravitational wave emission h^{TT} detected by a given particular instrument and reads

$$h_c \equiv \left[3\int_0^\infty \frac{S_h(f_c)}{S_h(f)}\langle|\tilde{h}(f)|^2\rangle f df\right]^{1/2} . \tag{2.28}$$

The resulting signal-to-noise ratio is then computed as

$$\frac{S}{N} = \frac{h_c}{h_{\rm rms}(f_c)} , \tag{2.29}$$

where $h_{\rm rms}(f_c) \equiv \sqrt{f_c S_h(f_c)}$ is the *strain noise* of the detector at the characteristic frequency.

Figure 2.11 shows the strain noise of the three detectors considered here, as a function of frequency. Note that all of the sensitivity curves reported assume an optimally incident wave in position and polarization and that the curve for Advanced LIGO represents the sum of presently anticipated noise sources. In Fig. 2.11 we show the computed characteristic amplitudes in comparison with the strain noise of the detectors for sources located at a distance of 10 Kpc (*i.e.* for galactic sources) and 20 of Mpc (*i.e.* for sources within the Virgo cluster). As it is evident from the figure, in the first case all of the models considered lie well above the sensitivity curves of the detectors, while in the second case only a couple of models would be marginally detected by the Advanced LIGO detector. Note also that the relatively high scattering of the models in the figure (from the most powerful one, B5a, to the least powerful one, A4a) are due to the differences in the average rest-mass densities.

In Table 2.4 we report the characteristic frequency, characteristic amplitude, and S/N ratio of the gravitational waves emitted by our tori models, with respect to the different detectors considered. In particular we choose the sources at the distance of 10Kpc for LIGO I and VIRGO, while extragalactic sources at a distance of 20 Mpc for Advanced LIGO. We also remark that the numbers obtained should be considered as lower limits of the amplitudes of the gravitational wave signals that could be effectively emitted. Firstly, because the torus-to-hole mass ratio could be higher than 0.1, and the gravitational signal, which scales linearly with this ratio (see Zanotti et al. 2003), would then be proportionally larger. Secondly, because the perturbations affecting the torus could be dramatically larger in a realistic formation scenario, *i.e.* after the core-collapse of a massive star or binary neutron star merger.

Table 2.4: Computed estimates regarding the detection of the gravitational wave signals emitted by relativistic tori around Kerr black holes with power-law distributions of the angular momentum. The table reports the characteristic frequency, the characteristic amplitude and the signal-to-noise ratio computed for three detectors, LIGO I, VIRGO and Advanced LIGO, assuming a galactic distance for the first two, and an extra-galactic distance for the Advanced LIGO detector. $\tau_{\rm life} = 100$ orbital periods.

Model	f_c (Hz) LIGO I (10 Kpc)	f_c (Hz) VIRGO (10 Kpc)	f_c (Hz) A. LIGO (20 Mpc)	h_c LIGO I (10Kpc)	h_c VIRGO (10Kpc)	h_c A. LIGO (20 Mpc)	S/N LIGO I (10 Kpc)	S/N VIRGO (10 Kpc)	S/N A. LIGO (20 Mpc)
A1a	205	207	206	4.6×10^{-21}	4.7×10^{-21}	2.3×10^{-24}	10.1	7.5	0.09
A2a	169	170	171	3.6×10^{-21}	3.6×10^{-21}	1.8×10^{-24}	9.0	6.3	0.07
A3a	137	139	140	2.1×10^{-21}	2.2×10^{-21}	1.1×10^{-24}	5.8	3.9	0.04
A4a	121	117	122	1.4×10^{-21}	1.7×10^{-21}	8.3×10^{-25}	4.1	3.2	0.03
B1a	344	367	336	1.6×10^{-20}	1.7×10^{-20}	7.3×10^{-24}	19.5	20.4	0.14
B2a	303	361	281	5.1×10^{-21}	5.7×10^{-21}	2.0×10^{-24}	7.2	7.0	0.06
B3a	279	341	261	2.8×10^{-21}	3.2×10^{-21}	1.1×10^{-24}	4.3	4.0	0.03
B4a	239	299	233	1.5×10^{-21}	1.7×10^{-21}	6.0×10^{-25}	2.7	2.3	0.02
B5a	519	522	515	3.5×10^{-19}	3.5×10^{-19}	1.7×10^{-22}	247	325	1.3
B6a	498	505	487	2.3×10^{-19}	2.4×10^{-19}	1.1×10^{-22}	175	225	1.0
B7a	446	454	436	1.2×10^{-19}	1.2×10^{-19}	5.6×10^{-23}	100	122	0.6
B8a	366	393	349	4.3×10^{-20}	4.5×10^{-20}	1.8×10^{-23}	48	52	0.3
B9a	275	325	267	1.5×10^{-20}	1.8×10^{-20}	6.2×10^{-24}	24	22	0.2
C1a	538	556	506	6.5×10^{-20}	6.7×10^{-20}	3.0×10^{-23}	44	58	0.23
C2a	454	493	406	2.3×10^{-20}	2.4×10^{-20}	1.0×10^{-23}	20	24	0.12
C3a	412	491	347	1.1×10^{-20}	1.3×10^{-20}	4.3×10^{-24}	10.9	12.3	0.07
C4a	239	318	226	7.4×10^{-21}	9.8×10^{-21}	2.9×10^{-24}	10.9	12.0	0.1

2.7 Implications for HFQPOs in LMXBs

Observations of X-ray emissions from binary systems comprising a stellar-mass compact object have long been considered important tools to test General Relativity in strong-field regimes. In particular, the high frequency quasi-periodic oscillations (HFQPOs) observed in LMXBs binaries containing a black hole candidate have been proposed as a tool for measuring black hole properties such as mass and spin in a direct way. In such systems, the X-ray observations show a particularly rich phenomenology in which the luminosity is modulated quasi-periodically, giving rise to distinctive peaks in the power spectral density. A puzzling feature of the QPO frequencies in these systems is that they are found in sequences of small integers (*i.e.* 1:2, 2:3, or 1:2:3; Abramowicz and Kluźniak, 2001; Remillard et al., 2002; Homan et al., 2003).

Numerous models have been suggested to explain the HFQPOs and their peculiar harmonic property (see Abramowicz and Kluźniak, 2004 for a recent review) but the scarcity of the observational data, on the one hand, and the crudeness of the different models, on the other hand, have not yet made it possible to determine which model provides the most likely description of the processes responsible for the QPOs. It should be noted the first steps towards a more quantitative and physically realistic description of the emission properties of possible QPO models have recently been taken (Schittman and Bertschinger, 2004; Schnittman, 2004).

Among the proposed models, one is particularly simple as it is based on the assumption that the accretion disc around the black hole terminates with a sub-Keplerian part, *i.e.* a torus of small size (Rezzolla et al., 2003a). This model was motivated by the numerical simulations of relativistic tori in a Schwarzschild spacetime (Zanotti et al., 2003) and by the subsequent perturbative study of p-mode oscillations of relativistic vertically integrated tori presented in RYZ. A Cornerstone of this model is the evidence, both numerical and analytic, that in these objects the fundamental mode and the first overtones are found to be in the harmonic sequence 2:3:4... to a good precision and in a very wide parameter space.

Because the p-modes considered in the above model represent the basic oscillation modes of a non-Keplerian disc, some of their features are not expected to be very sensitive to the properties of the spacetime which determine the motion of the fluid. The harmonic 2:3 relation between the fundamental frequency and the first overtone is one such feature and, indeed, this property has been encountered essentially unmodified in Schwarzschild and Kerr spacetimes, but also in a Newtonian gravitational potential. Because of this, it is then natural to consider whether a fully Newtonian description of the physics is sufficient to account for the phenomenology observed in HFQPOs, or whether General Relativity is indeed necessary. This question in addressed in the following Section.

2.7.1 Can Newtonian Physics Explain the HFQPOs?

In order to assess whether p-mode oscillations in purely Newtonian tori could account for the HFQPO phenomenology, we have performed a global analysis of the axisymmetric oscillations of vertically integrated non-Keplerian discs in Newtonian physics and compared the results with those obtained in a general relativistic framework.

Consider therefore a non-selfgravitating perfect fluid torus in equilibrium and orbiting a central object of mass M_0 producing a gravitational potential Ψ. As in the general relativistic case, the system of equations describing the torus will be simplified by considering vertically integrated or vertically averaged quantities, which we indicate as P and Σ, in analogy with corresponding relativistic quantities (*cf.* Eqs. (2.4) and (2.5)). In order to handle simpler expressions we normalize all quantities as

$$\widetilde{v}^{\,i} \equiv \frac{v^i}{c_0} , \qquad \widetilde{\Sigma} \equiv \frac{\Sigma}{\Sigma_0} , \qquad \widetilde{P} \equiv \frac{P}{P_0} , \qquad \widetilde{\varpi} \equiv \frac{\varpi}{\varpi_0} , \tag{2.30}$$

where $i = \varpi, \phi$, while Σ_0 is the maximum mass density and where we have defined

$$P_0 \equiv K\Sigma_0^{1+1/N} , \qquad c_0^2 \equiv \left(1 + \frac{1}{N}\right)\frac{P_0}{\Sigma_0} , \qquad \varpi_0 \equiv \frac{GM_0}{c_0^2} . \tag{2.31}$$

The equilibrium configurations are then obtained by solving the hydrostatic equilibrium equation which, in terms of the normalized quantities, is written simply as

$$\frac{1}{\widetilde{\Sigma}}\widetilde{P}' = \widetilde{\Omega}^2\widetilde{\varpi} - \widetilde{\Psi}' , \tag{2.32}$$

where $\widetilde{\Psi} \equiv \Psi/c_0^2$ and $\widetilde{\Omega} \equiv \Omega/\Omega_0$, with Ω_0 being the angular velocity at ϖ_0. Introducing now the Emden function $\widetilde{\Theta}$ and its related quantity $\widetilde{Q} \equiv N\widetilde{\Theta}$, the normalized rest-mass density

$\widetilde{\Sigma}$ can be written as $\widetilde{\Sigma} = \widetilde{\Theta}^N$, and the equation of hydrostatic equilibrium is expressed as an ordinary differential equation for $\widetilde{Q}$, *i.e.*

$$\widetilde{Q}' = \widetilde{\Omega}^2 \widetilde{\varpi} - \frac{1}{\widetilde{\varpi}^2} \, . \tag{2.33}$$

Once the angular velocity distribution $\Omega = \Omega(\varpi)$ is fixed and a choice is made for the inner radius $\widetilde{\varpi}_{\rm in}$, equation (2.33) can be integrated to provide the background Newtonian torus in equilibrium.

For simplicity we now restrict our attention to constant specific angular momentum distributions so that the equation of hydrostatic equilibrium (2.33) simplifies to

$$\widetilde{Q}' = \frac{\ell^2}{\widetilde{\varpi}^3} - \frac{1}{\widetilde{\varpi}^2} = -\left(\frac{\ell^2}{2\widetilde{\varpi}^2} - \frac{1}{\widetilde{\varpi}}\right)' \, . \tag{2.34}$$

Before discussing the solution of the eigenvalue problem, it is useful to recall the features of the Newtonian models that represent important differences from the relativistic counterparts. The first one is that the right-hand side of equation (2.34) is just the derivative of an effective potential (*i.e.* the one in the round brackets) and it is therefore straightforward to calculate the inner edge of the largest possible torus as the radial position at which this potential vanishes, *i.e.* $(\widetilde{\varpi}_{\rm in})_{\rm MIN} = \ell^2/2$.

The second feature to notice is again easily derived from equation (2.34) and shows that the position of the mass density maximum (*i.e.* $Q' = 0$) is simply given by $\widetilde{\varpi}_{\rm max} = \ell^2$, coinciding with the position at which the specific angular momentum assumes a Keplerian value. As in relativistic tori, $\widetilde{\varpi}_{\rm max}$ grows with increasing specific angular momentum; unlike relativistic tori, however, no lower or upper limits exist for $\widetilde{\varpi}_{\rm max}$. Indeed, for vanishingly small values of ℓ, it is possible to construct tori whose pressure maxima lie arbitrarily close to the rotation axis. This property is the consequence of the fact that, in Newtonian physics and for constant distributions of specific angular momentum, ℓ is not constrained to lie in a finite interval. This represents a major difference with respect to the general relativistic picture and, as will be discussed later on, makes the parameter space for the background models effectively unbounded.

We next proceed to consider the eigenvalue problem and, as we did for the general relativistic case, we neglect perturbations in the gravitational potential (Cowling approximation) and introduce perturbations in the velocity and pressure with a harmonic time

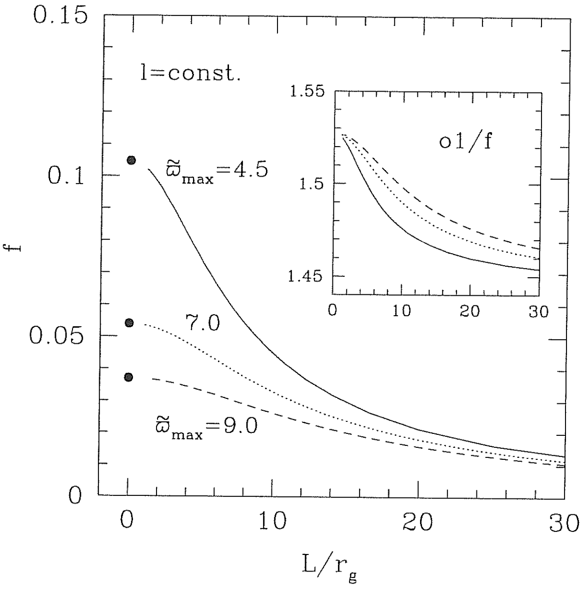

Figure 2.12: Eigenfrequencies of the fundamental mode of oscillation for Newtonian tori with constant angular momentum distribution orbiting a central mass $M = 10\,M_\odot$. We show with solid circles the values of the Newtonian Keplerian radial epicyclic frequency at the different locations of $\varpi_{\rm max}$, while the inset shows the ratio of the first overtone and of fundamental eigenfrequency as a function of the radial extents L.

dependence of the type $\sim \exp(-i\sigma t)$. To simplify the notation, hereafter we will omit the "tilde" on all variables, which however should be meant to refer to normalized quantities. As a result, the perturbed Euler and continuity equations can be written as

$$\sigma\delta\Sigma + \frac{1}{\varpi}\left(\varpi\Sigma\delta U\right)' = 0 \ , \tag{2.35}$$

$$\sigma\delta U + 2\varpi\Omega\delta W - \delta Q' = 0 \ , \tag{2.36}$$

$$\left(\Omega' + \frac{2}{\varpi}\Omega\right)\delta U + \sigma\delta W = 0 \ , \tag{2.37}$$

where, in analogy with the corresponding relativistic quantities, δU and δW are the vertically averaged radial and azimuthal velocities, respectively (*cf.* eqs. 2.10 and 2.11).

After some simple algebra, equations (2.35)–(2.37) are cast into a single, second-order ordinary differential equation

$$\delta Q'' + \left[\frac{1}{\varpi} + \frac{Q'}{Q}N + \ln\left(\frac{\sigma}{D}\right)'\right]\delta Q' + \frac{ND}{Q}\delta Q = 0 \ , \tag{2.38}$$

for the quantity δQ defined as

$$\delta Q \equiv \left(\frac{N}{N+1}\right)\frac{\delta P}{\Sigma} \ . \tag{2.39}$$

In equation (2.38), the quantity

$$D \equiv \sigma^2 - 2\Omega(2\Omega + \varpi\Omega') \ , \tag{2.40}$$

measures the deviation of the eigenfrequency σ from the Newtonian radial epicyclic frequency $(\kappa_{\rm r}^2)_{\rm Newt} \equiv 2\Omega(2\Omega + \varpi\Omega')$, which coincides with the orbital frequency when the orbital motion is Keplerian, *i.e.* $(\kappa_{\rm r})_{\rm Newt} = \Omega_{\rm Kep}$. Note that while equation (2.38) appears to be singular at the radial position where $D = 0$, it is actually regular everywhere since $\delta Q'$ and D vanish at the same position (*cf.* eqs. 2.36 and 2.37).

The eigenfrequencies and eigenfunctions of the axisymmetric p-modes described by equations (2.35)-(2.37) have been computed using the same numerical method discussed in the previous Sections and some representative results are presented in Fig. 2.12. More specifically, we show the eigenfrequencies of the fundamental mode of oscillation for three sequences of constant angular momentum Newtonian tori orbiting a central source of gravitational potential with a mass of $10M_{\odot}$. The sequences have been built keeping the position of the density maximum fixed (*i.e.* $\tilde{\varpi}_{\rm max} = 4.5$, 7.0 and 9.0, respectively) and varying the position of the inner radius to produce tori of different radial sizes. The inset, on the other hand, shows the ratio of the first overtone to the fundamental eigenfrequency as a function of the tori radial size of the torus for the three different sequences. A first glance at Fig. 2.12 and a comparison with Figs. 2.4, 2.5 and 2.6, shows that no major *qualitative* differences emerge in a Newtonian framework and that all of the most important features of p-modes in relativistic tori remain unchanged also in the corresponding Newtonian models. Most notably, the fundamental eigenfrequencies depend on the position of the mass density and on the radial sizes of the discs, increasing as the latter decrease. In addition, as the radial sizes tend to zero, the fundamental eigenfrequencies tend to the values of the radial epicyclic frequencies at the position of the mass density maxima. Finally, along all sequences, the first and second eigenfrequencies are in a harmonic sequence 2:3.

Besides this qualitative agreement, however, *quantitative* differences are also present and can be easily appreciated by comparing, for instance, the curve for $a/M = 0$ in the top panel of Fig. 2.5 with the dotted line in Fig. 2.12. Indeed, the simultaneous presence of qualitative similarities and quantitative differences between Newtonian and general relativistic models is not surprising and reflects the fact that the p-modes are fundamental modes of oscillation of orbiting fluid objects. As such, they depend only in part on the gravitational field (or background spacetime) in which the fluid is moving. Indeed, also for rotating stars, the qualitative features of the p-mode oscillations are preserved when going from a Newtonian description to a full general relativistic one, with quantitative differences being present, however, and depending on the strength of the spacetime curvature.

Finally, note that because the radial epicyclic frequencies represent the asymptotic limit of the fundamental eigenfrequencies for vanishing torus sizes and since the Newtonian epicyclic frequency is always *larger* than the corresponding general relativistic one for all values of the black hole spin (*cf.* solid and dotted lines in Fig. 2.1), all of the Newtonian frequencies along a sequence with $\ell =$ const. will be larger than the corresponding relativistic ones. This, together with the fact that the Newtonian epicyclic frequency diverges for vanishingly small radii [*i.e.* $(\kappa_{\rm r})_{\rm Newt} = \Omega_{\rm Kep} \sim \varpi^{-3/2}$], makes it clear that for any observed QPO frequency it will be possible to find a Newtonian torus of size L that could produce p-mode oscillations with the correct frequencies and in a 2:3 ratio. Stated differently, while the parameter space in the (f, L) plane for relativistic tori is bounded above by the sequence approaching the largest epicyclic frequency admissible by a Kerr black hole with spin $a/M = 1$, this restriction does not exist for Newtonian tori and a Newtonian physicist, who ignores the existence of marginally stable orbits or of an event horizon, would be able to find an equilibrium solution at every point in that plane.

As a result, and at least in principle, Newtonian physics could explain the HFQPOs if the only information available is the mass of the central object M and the frequencies of the modulation in the X-ray luminosity σ. The only way to remove this ambiguity and thus disprove the interpretation of the Newtonian physicist, would be to make combined measurements of M and σ, together with the radial extension of the torus L or of the position of the mass density maximum $\varpi_{\rm max}$. While these observations would probably difficult to make in practice, similar difficulties are found also in proving the existence of stellar-mass black holes in X-ray binaries (Abramowicz, Kluźniak and Lasota, 2002). This is simply the consequence of the fact that no limit exists in Newtonian physics to the compactness of the sources of gravitational potential.

Chapter 3

Numerical Relativistic Hydrodynamics

3.1 Introduction

Solving numerically the coupled system of the Einstein equations and the relativistic hydrodynamic equations is a very challenging task. This difficulty arises from the several ingredients needed for successful numerical relativistic simulations such as computation of accurate initial data, suitable formulation of the evolution equations, appropiate gauge and boundary conditions, as well as accurate and stable numerical schemes that integrate forward in time the evolution equations. The field of numerical relativistic hydrodynamics has experienced a significant advance in recent years as a result of several factors (see for a review Brügmann 2000; Lehner 2001; Font 2003). One of these factors, is the development new formulations of the Einstein equations and the relativistic hydrodynamic equations. These formulations are better suited for their numerical solution and allow for long-term numerical evolutions. Another important factor is the development of powerful supercomputers which are used to carry out computationally expensive numerical simulations. Also the need of accurate waveforms which can be used as templates to correlate the gravitational wave detector output in the so called "matched filtering" techniques have contributed to the development of the field of numerical relativity. Numerical relativistic simulations represent a valuable tool to gain a better insight into the physics of compact objects, such as neutron stars, and understanding relativistic astrophysical processes such as the formation of outflows and Gamma-ray bursts.

In this Chapter, we first describe the 3+1 decomposition of the Einstein equations and a conformal traceless formulation which is now widely used in numerical relativity. Next, we focus on the formulation of the relativistic hydrodynamic equations as conservation laws and on the high resolution shock capturing (HRSC) schemes. Furthermore, these Sections introduce the formulation of the Einstein equations and the hydrodynamic equations that we have implemented in the `Nada` code, described in the following Chapter, and also in the `Whisky` code presented in the last part of this Chapter.

In Sections 3.2, 3.3 and 3.4 we adopt abstract index notation (we refer to Wald, 1984, Section (2.4) for an extended discussion of this notation) and use the Latin letters *a*-*h* and *o*-*z* to denote abstract indices, which run from 0 to 3. When we express three-dimensional tensors in a coordinate system, we use the Latin indices $i - n$, which run from 1 to 3, while for four-dimensional objects we use Greek letters which run from 0 to 3.

3.2 3+1 Decomposition of Spacetime

The covariant framework in general relativity, in which time has the same "status" as the three remaining spatial dimensions and where space and time are unified into a 4-dimensional spacetime, is not well adapted to perform numerical simulations that aim to evolve forward in time a given set of initial data. In this Section, we will summarize an initial value formulation of general relativity, commonly referred to as the "ADM" formulation of Einstein's equations (after Arnowitt, Deser and Misner 1962) or the 3+1 decomposition, since the spacetime is split into a time dimension and three spatial dimensions. We refer to York (1979); Wald (1984); Choptuik (1998) and Baumgarte & Shapiro (2003) for further details on the 3+1 decomposition.

In this formulation, the spacetime (M, g_{ab}) is foliated into a series of non-intersecting spacelike hypersurfaces, Σ_t, which are parametrized by a scalar function, t. The foliation is characterized by the closed one-form

$$\Omega_a = \nabla_a t. \tag{3.1}$$

where ∇_a denotes the covariant derivative associated with the 4-metric g_{ab}. Orthogonal to the hypersurfaces lies the timelike unit normal vector field, n^a defined by

$$n_a = -\alpha \nabla_a t, \tag{3.2}$$

where the lapse function α is defined from the normalization: $n^a n_a = -1$. The spatial component of γ_{ab}, induced by the spacetime 4-metric g_{ab}, is a spatial metric to the spatial slice, Σ_t and is given by

$$\gamma_{ab} = g_{ab} + n_a n_b. \tag{3.3}$$

A projection operator that projects a 4-dimensional tensor into a spacelike slice is obtained by rising one index in Eq. (3.3)

$$\gamma^a{}_b = g^a{}_b + n^a n_b. \tag{3.4}$$

Using the projection operator (3.4) we define the covariant derivative D_a compatible with the spatial metric γ_{ab}; for example

$$D_a T_c{}^b \equiv \gamma_a^d \gamma_e^b \gamma_c^f \nabla_d T_f{}^e. \tag{3.5}$$

The 4-dimensional Riemann tensor, ${}^{(4)}R_{abc}{}^d$, is defined by the action of the commutator of the covariant derivatives on an arbitrary dual-vector field, V_a

$$\left(\nabla_a \nabla_b - \nabla_b \nabla_a\right) V_c = {}^{(4)} R_{abc}{}^d V_d, \tag{3.6}$$

while the Riemann tensor of a hypersurface is defined by requiring that for every spatial dual-vector field, W_a

$$\left(D_a D_b - D_b D_a\right) W_c = R_{abc}{}^d W_d \ , \quad n_d R_{abc}{}^d = 0. \tag{3.7}$$

The spatial Ricci tensor, R_{ab}, and the spatial Ricci scalar, R can be obtained from $R_{abc}{}^d$ by contraction in the usual manner.

We have defined the Riemann tensor associated with the spatial metric, ${R_{abc}}^d$, but this cannot contain all of the information as the 4-dimensional Riemann tensor also involves time derivatives, that is, ${R_{abc}}^d$ gives information about the curvature intrinsic to the slice but not about the embedding of the slice in the 4-dimensional spacetime. This information, which is related to the time derivative of the spatial metric is given through the extrinsic curvature tensor, K_{ab}, which is defined by projecting the the gradient of the hypersurface normal into the slice

$$K_{ab} = -{\gamma^c}_a {\gamma^d}_b \nabla_c n_d. \tag{3.8}$$

or alternatively, taking the Lie derivative along the unit normal vector field, $\mathcal{L}_{\mathbf{n}}$, of the spatial metric $\gamma_{ab} = g_{ab} + n_a n_b$ and using $n_b \nabla_a n^b = 0$, it can be easily show that an equivalent definition of the extrinsic curvature tensor is

$$K_{ab} = -\frac{1}{2} \mathcal{L}_{\mathbf{n}} \gamma_{ab}. \tag{3.9}$$

The spatial metric, γ_{ab}, and the extrinsic curvature, K_{ab}, have to satisfy certain relations so that the spatial slices are consistently embedded into the spacetime, M. These relations are obtained by means of the the spatial projections of the 4-dimensional Riemann tensor into Σ_t, known as the Gauss, Codazzi and Ricci equations.

The Gauss equation is obtained by projecting all indices of ${}^{(4)}{R_{abc}}^d$ into Σ_t,

$${\gamma^p}_a {\gamma^q}_b {\gamma^r}_c {\gamma^s}_d \, {}^{(4)}R_{pqrs} = R_{abcd} + K_{ac} K_{bd} - K_{bc} K_{ad}, \tag{3.10}$$

the Codazzi equation, by projecting three indices into Σ_t and contracting one index with the unit normal, n^a,

$${\gamma^p}_a {\gamma^q}_b {\gamma^r}_c n^s \, {}^{(4)}R_{pqrs} = D_a K_{cb} - D_c K_{ab}, \tag{3.11}$$

and finally, the Ricci equation is obtained by making two spatial projections and two contractions with n^a,

$$n^d n^c {\gamma^p}_a {\gamma^q}_b \, {}^{(4)}R_{qdpc} = \mathcal{L}_n K_{ab} + \frac{1}{\alpha} D_a D_b \alpha + {K^c}_b K_{ac}. \tag{3.12}$$

Since the foliation is described by the closed one-form, Ω_a (3.1), it is convenient to express the time derivative along a vector field, t^a, as dual to the closed one-form:

$$t^a \Omega_a = t^a \nabla_a t = 1, \tag{3.13}$$

t^a can be decomposed in a part orthogonal and in a part tangential to Σ_t in terms of the lapse function, α, and a spatial vector named the shift vector, β^a,

$$t^a = N^a + \beta^a = \alpha n^a + \beta^a. \tag{3.14}$$

The lapse function determines how much proper time elapses between two timeslices along the normal vector, n^a, and the shift vector indicates how much spatial the coordinates are shifted with respect to the normal vector. Thus, given two spatial slices, Σ_{t1} and Σ_{t2}, parametrized by the coordinate time t, the vector field t^a, will determine how coordinates move forward in time from Σ_{t1} to Σ_{t2}.

3.3 3+1 Decomposition of Field Equations

We have now defined all of the geometrical objects associated with the spatial slices needed to write the Einstein equations in the ADM form, which consists of a set of four *constraint equations* and the *evolution equations* for the spatial metric and the extrinsic curvature. These equations are obtained by projecting the Einstein equations into Σ_t and n^a and using the Gauss, Codazzi and Ricci equations to eliminate the 4-dimensional Riemann tensor. The matter content on each slice is described by the projections of the stress-energy tensor, T_{ab}, the energy density, the momentum density and the spatial stress-energy tensor as measured by the normal observer n^a

$$\rho \equiv n^a n^b T_{ab}, \tag{3.15}$$

$$j_a \equiv -\gamma^b{}_a n^c T_{bc}, \tag{3.16}$$

$$S_{ab} \equiv \gamma^c{}_a \gamma^d{}_b T_{cd}. \tag{3.17}$$

Contracting both indices with the normal field in the Einstein equation

$$R_{ab} - \frac{1}{2} g_{ab} R = 8\pi T_{ab}, \tag{3.18}$$

and using a contraction of the Gauss equation (3.10) leads to the *Hamiltonian constraint*

$$R + K^2 - K_{ab}K^{ab} = 16\pi\rho, \tag{3.19}$$

where $K = K^{a}{}_{a}$ is the trace of the extrinsic curvature tensor. Similarly, contracting one index in the Einstein equation (3.18) with the normal field and projecting the remaining index onto the hypersurface and using the Codazzi equation yields to the *momentum constraint*

$$D_b K_a^b - D_a K = 8\pi j_a. \tag{3.20}$$

The two constraint equations, the Hamiltonian and momentum constraints, involve only spatial quantities and their spatial derivatives. The spatial metric and the extrinsic curvature have to satisfy the constraints on each hypersurface in order to allow for the embedding of the spatial slices $(\Sigma_t,\, \gamma_{ab},\, K_{ab})$ in the spacetime $(M,\, g_{ab})$. Evolution equations, on the other hand, govern how the initial data $(\gamma_{ab},\, K_{ab})$ evolve forward in time from one spatial slice to the next. The evolution equation for the spatial metric follows from the definition of the extrinsic curvature (3.9) and expressing in terms of t^a

$$\mathcal{L}_t \gamma_{ab} = -2\alpha K_{ab} + \mathcal{L}_\beta \gamma_{ab}. \tag{3.21}$$

The evolution equation for the extrinsic curvature follows from the spatial projection of Einstein's equations (3.18) and Ricci's equation (3.12)

$$\begin{aligned} \mathcal{L}_t K_{ab} = {} & -D_a D_b \alpha + \alpha \left(R_{ab} - 2K_{ac}K_b^c + K K_{ab}\right) \\ & -\alpha 8\pi \left(S_{ab} - \frac{1}{2}\gamma_{ab}\left(S - \rho\right)\right) + \mathcal{L}_\beta K_{ab}, \end{aligned} \tag{3.22}$$

where $S = S_a^a$ is the trace of S_{ab}.

So far, the spacetime basis of vectors has been completely arbitrary and in no particular relatioship with the one-form Ω_a, so that the constraint and evolution equations have been derived in the most general form (*i.e.* in a tensorial and coordinate independent manner). Next, we introduce a basis of spatial vectors that are well adapted to the 3+1 decomposition of the spacetime, that is, we introduce a basis of spatial vectors e_i (where i=1,2,3) tangential to each slice Σ_t, so that $\Omega_a (e_i)^a = 0$. We choose as the fourth basis vector $(e_0)^a = t^a$ so that the Lie derivative along t^a reduces to the partial derivative with respect to t and the covariant, spatial components of the normal vector n^a vanish, $n_i = n_a (e_i)^a = 0$. Since the projection of a spatial tensor along the normal vector is zero, the zeroth component of contravariant spatial tensors have to be zero. We then can write the shift vector as

$$\beta^a = \left(0, \beta^i\right), \tag{3.23}$$

and, since $n^a = \frac{1}{\alpha}\left(t^a - \beta^a\right)$ the normal vector takes the form

$$n^a = \frac{1}{\alpha}\left(1, -\beta^i\right), \tag{3.24}$$

and its covariant components are

$$n_a = (\alpha, 0, 0, 0). \tag{3.25}$$

From the definition of the spatial metric and using (3.25) it follows that $\gamma^{a0} = 0$ and $\gamma_{ij} = g_{ij}$. The inverse 4-dimensional metric can be expressed as

$$g^{\alpha\beta} = \begin{pmatrix} -\alpha^{-2} & \alpha^{-2}\beta^i \\ \alpha^{-2}\beta^j & \gamma^{ij} - \alpha^{-2}\beta^i\beta^j \end{pmatrix}, \tag{3.26}$$

and the components of the 4-dimensional metric are

$$g_{\alpha\beta} = \begin{pmatrix} -\alpha^2 + \beta_k\beta^k & \beta_i \\ \beta_j & \gamma_{ij} \end{pmatrix}. \tag{3.27}$$

Then the line element in the 3+1 formulation becomes

$$ds^2 = -\alpha^2 dt^2 + \gamma_{ij}\left(dx^i + \beta^i dt\right)\left(dx^j + \beta^j dt\right). \tag{3.28}$$

Since the entire content of the decomposed Einstein equations is contained in their spatial components alone, the Hamiltonian constraint (3.19) can be expressed as

$$R + K^2 - K_{ij}K^{ij} = 16\pi\rho, \tag{3.29}$$

the momentum constraint (3.20) as

$$D_j K^j_i - D_i K = 8\pi j_i, \tag{3.30}$$

and the evolution equations for the spatial metric (3.21) and the extrinsic curvature (3.22) as

$$\partial_t \gamma_{ij} = -2\alpha K_{ij} + D_i\beta_j + D_j\beta_i, \tag{3.31}$$

$$\begin{aligned} \partial_t K_{ij} &= -D_i D_j \alpha + \alpha\left(R_{ij} - 2K_{ik}K^k_j + KK_{ij}\right) \\ &\quad - \alpha 8\pi\left(S_{ij} - \frac{1}{2}\gamma_{ij}\left(S - \rho\right)\right) \\ &\quad + \beta^k D_k K_{ij} + K_{ik}D_j\beta^k + K_{kj}D_i\beta^k. \end{aligned} \tag{3.32}$$

Equations (3.29) to (3.32) are known as the ADM equations. The lapse function α, and the shift vector β^i describe how coordinates evolve from slice to slice they reflect the gauge freedom in general relativity. Moreover, appropriate gauges are a key ingredient for long-term stable numerical simulations and we will comment further on them in Section 4.4.

3.4 Conformal-Traceless Reformulation of ADM System

The ADM system of equation (3.29-3.32) is still not in the most convenient form for numerical implementation since it develops instabilities (Bona et al., 1995; Anninos et al., 1996; Cook et al., 1998; Alcubierre et al., 2000b). Nakamura, Oohara and Kojima presented in 1987 a conformal-traceless reformulation of the ADM system (which we refer to here as the NOK formulation). In this formulation the trace of the extrinsic curvature is evolved separately and mixed second derivatives in the Ricci tensor are eliminated with the introduction of auxiliary variables. The most widespread versions of this formalism are those given by Shibata and Nakamura (1995) and Baumgarte and Shapiro (1999) and are commonly known as the BSSN formulation. It has been shown (Baumgarte et al., 1999; Shibata et al., 2000; Shibata & Uryu 2000; Alcubierre et al., 2000a,b; Shibata & Uryu 2002; Font et al., 2002c) that numerical implementations based on this new reformulation are more robust and allow for long-term numerical simulations even in spacetimes involving strong gravitational fields, such as black holes and neutron stars. This section describes this reformulation of the ADM system as it has been implemented in the `Nada` code (described in the following Chapter). We first introduce a conformal factor and the conformally related metric as

$$\tilde{\gamma}_{ij} = e^{-4\phi}\gamma_{ij}, \tag{3.33}$$

such that the determinant of the conformal metric, $\tilde{\gamma}_{ij}$, is unity and $\phi = \ln(\gamma)/12$, where $\gamma = det(\gamma_{ij})$. We also define the conformally related traceless part of the extrinsic curvature, K_{ij},

$$\tilde{A}_{ij} = e^{-4\phi}A_{ij} = e^{-4\phi}\left(K_{ij} - \frac{1}{3}\gamma_{ij}K\right). \tag{3.34}$$

Taking the trace of the evolution equation (3.31) for the spatial metric leads to an evolution equation for the trace of γ_{ij}, γ

$$\partial_t \ln(\gamma) = -2\alpha K + 2D_i\beta^i, \tag{3.35}$$

and using the new variables we obtain an evolution equation for the conformal factor

$$\partial_t\phi = -\frac{1}{6}\alpha K + \beta^i\partial_i\phi + \frac{1}{6}\partial_i\beta^i. \tag{3.36}$$

Similarly, by taking the trace of the evolution equation (3.32) for K_{ij} and combining with the Hamiltonian constraint we obtain (3.29)

$$\partial_t K = -\gamma^{ij}D_jD_i\alpha + \alpha\left(\tilde{A}_{ij}\tilde{A}^{ij} + \frac{1}{3}K^2\right) + 4\pi\alpha\left(\rho + S\right) + \beta^i\partial_i K. \tag{3.37}$$

Combining these equations (3.36) and (3.37) with the evolution equations (3.31) and (3.32) we arrive to the evolution equations for $\tilde{\gamma}_{ij}$ and $\tilde{A}_{ij}$

$$\partial_t\tilde{\gamma}_{ij} = -2\alpha\tilde{A}_{ij} + \beta^k\partial_k\tilde{\gamma}_{ij} + \tilde{\gamma}_{ik}\partial_j\beta^k + \tilde{\gamma}_{kj}\partial_i\beta^k - \frac{2}{3}\gamma_{ij}\partial_k\beta^k, \tag{3.38}$$

$$\begin{aligned}\partial_t\tilde{A}_{ij} \;=\;& e^{-4\phi}\left[\alpha\left(R_{ij} - \frac{1}{3}\gamma_{ij}R\right) - \alpha 8\pi\left(S_{ij} - \frac{1}{3}\gamma_{ij}S\right)\right.\\ &\left.-\left(D_iD_j\alpha - \frac{1}{3}\gamma_{ij}D^kD_k\alpha\right)\right] + \alpha\left(K\tilde{A}_{ij} - 2\tilde{A}_{il}\tilde{A}^l_j\right)\\ &+\beta^k\partial_k\tilde{A}_{ij} + \tilde{A}_{ik}\partial_j\beta^k + \tilde{A}_{kj}\partial_i\beta^k - \frac{2}{3}\tilde{A}_{ij}\partial_k\beta^k.\end{aligned} \tag{3.39}$$

The Ricci tensor R_{ij} that appears in the source term of the evolution equation (3.39) is split into two parts as follows

$$R_{ij} = R^{\phi}_{ij} + \tilde{R}_{ij}, \tag{3.40}$$

where R^{ϕ}_{ij} is given by

$$R^{\phi}_{ij} = -2\tilde{D}_i\tilde{D}_j\phi - 2\gamma_{ij}\tilde{D}^k\tilde{D}_k\phi + 4\tilde{D}_i\phi\tilde{D}_j\phi - 4\gamma_{ij}\tilde{D}^k\phi\tilde{D}_k\phi, \tag{3.41}$$

where $\tilde{D}_i$ is the covariant derivative with respect to the conformal metric $\tilde{\gamma}_{ij}$. Following Baumgarte and Shapiro (1999) the conformal Ricci tensor, $\tilde{R}_{ij}$, is expressed as

$$\tilde{R}_{ij} = -\frac{1}{2}\tilde{\gamma}^{mn}\partial_{mn}\tilde{\gamma}_{ij} + \tilde{\gamma}_{k(i}\partial_{j)}\tilde{\Gamma}^k + \tilde{\Gamma}^k\tilde{\Gamma}_{(ij)k} + \tilde{\gamma}^{mn}\left(2\tilde{\Gamma}^k_{m(i}\tilde{\Gamma}_{j)kn} + \tilde{\Gamma}^k_{in}\tilde{\Gamma}_{kmj}\right), \tag{3.42}$$

where $\tilde{\Gamma}^i{}_{ij}$ are the connection coefficients associated with $\tilde{\gamma}_{ij}$ and we have introduced the *conformal connection functions*, $\tilde{\Gamma}^i$, defined as

$$\tilde{\Gamma}^i \equiv \tilde{\gamma}^{jk}\tilde{\Gamma}^i{}_{jk} = -\partial_j \tilde{\gamma}^{ij}. \tag{3.43}$$

The conformal connection functions are considered as independent variables whose evolution equation follows from the definition (3.43) by permuting the time and space derivatives

$$\begin{aligned} \partial_t \tilde{\Gamma}^i &= -2\tilde{A}^{ij}\partial_j \alpha + 2\alpha \left(\tilde{\Gamma}^i_{jk}\tilde{A}^{kj} - \frac{2}{3}\tilde{\gamma}^{ij}\partial_j K - 8\pi \tilde{\gamma}^{ij} S_j + 6\tilde{A}^{ij}\partial_j \phi \right) \\ & \beta^j \partial_j \tilde{\Gamma}^i - \tilde{\Gamma}^j \partial_j \beta^i + \frac{2}{3}\tilde{\Gamma}^i \partial_j \beta^j + \frac{1}{3}\tilde{\gamma}^{li}\partial_{jl}\beta^j + \tilde{\gamma}^{lj}\partial_{lj}\beta^i. \end{aligned} \tag{3.44}$$

The main difference between this version and the one introduced by Shibata and Nakamura (1995) is that, in the latter, the auxiliary variables are $\tilde{F}_i = -\sum_j \partial_j \tilde{\gamma}_{ij}$ instead of the $\tilde{\Gamma}^i$.

The Evolution equations (3.35-3.39) and (3.44) are the new system of evolution equations equivalent to the ADM system. Because of the good stability properties of this conformal-traceless reformulation of the ADM system it is widely use in numerical relativity. For instance, the robustness of this formulation has been shown in recent simulations of the merger of binary neutron stars (Shibata & Uryu 2000, 2001, 2002; Shibata et al; 2003), evolutions involvin g black holes (Alcubierre et al., 2001b; Laguna et al., 2002; Yo et al., 2002; Duez et al., 2003, 2004) and long-term evolution of neutron stars (Font et al. 2002c) and gravitational collapse of neutron stars to black holes (Shibata 2003a,b; Baiotti et al., 2004).

3.4.1 Further Adjustments

In addition to the Hamiltonian and the momentum constraints, following Yo et al. (2002), we introduce these new constraints:

- $\tilde{A}_{ij}$, has to be traceless.
- The determinant of the conformal metric $\tilde{\gamma}_{ij}$ has to be unity.
- The conformal connection functions have to satisfy the following identity

$$\tilde{\Gamma}^i - \tilde{\gamma}^{jk}\tilde{\Gamma}^i_{jk} = 0. \tag{3.45}$$

We solve in our code only five components of the conformal-traceless part of the extrinsic curvature, $\tilde{A}_{ij}$, and by imposing that $\tilde{A}_{ij}$ has to be traceless we compute the $\tilde{A}_{zz}$ component as

$$\tilde{A}_{zz} = -\frac{\tilde{A}^x_x + \tilde{A}^y_y + \tilde{A}_{xz}\tilde{\gamma}^{xz} + \tilde{A}_{yz}\tilde{\gamma}^{yz}}{\tilde{\gamma}^{zz}}. \tag{3.46}$$

Similarly, we evolve only five components of the conformal metric and compute the $\tilde{\gamma}_{zz}$ component from the other five components and imposing that $det(\tilde{\gamma}_{ij}) = 1$

$$\tilde{\gamma}_{zz} = 1 + \frac{\tilde{\gamma}_{yy}\tilde{\gamma}^2_{xz} - 2\tilde{\gamma}_{xy}\tilde{\gamma}_{yz}\tilde{\gamma}_{xz} + \tilde{\gamma}_{xx}\tilde{\gamma}^2_{yz}}{\tilde{\gamma}_{xx}\tilde{\gamma}_{yy} - \tilde{\gamma}^2_{xy}}. \tag{3.47}$$

In practice, equation (3.44) is not used to evolve the conformal connection functions but the expression bellow is used instead

$$\begin{aligned}
\partial_t\tilde{\Gamma}^i &= -2\tilde{A}^{ij}\partial_j\alpha + 2\alpha\left(\tilde{\Gamma}^i_{jk}\tilde{A}^{kj} - \frac{2}{3}\tilde{\gamma}^{ij}\partial_j K - 8\pi\tilde{\gamma}^{ij}S_j + 6\tilde{A}^{ij}\partial_j\phi\right) \\
&\quad \beta^j\partial_j\tilde{\Gamma}^i - \tilde{\Gamma}^j\partial_j\beta^i + \frac{2}{3}\tilde{\Gamma}^i\partial_j\beta^j + \frac{1}{3}\tilde{\gamma}^{li}\partial_{jl}\beta^j + \tilde{\gamma}^{lj}\partial_{lj}\beta^i - \\
&\quad \left(\chi + \frac{2}{3}\right)\left(\tilde{\Gamma}^i - \tilde{\gamma}^{jk}\tilde{\Gamma}^i_{jk}\right)\partial_j\beta^j.
\end{aligned} \tag{3.48}$$

where χ is free parameter. We generally take $\chi = 2/3$.

3.5 Hyperbolic Partial Differential Equations

Let us consider a set of m one dimensional first order partial differential equations (we refer to Toro 1999 and Leveque 1992, 1998 for further details) written in matrix form as

$$\partial_t\mathbf{U} + \mathbf{A}\partial_x\mathbf{U} + \mathbf{S} = 0, \tag{3.49}$$

where

$$\mathbf{U} = \begin{bmatrix} U_1 \\ U_2 \\ \vdots \\ U_m \end{bmatrix}, \quad \mathbf{S} = \begin{bmatrix} S_1 \\ S_2 \\ \vdots \\ S_m \end{bmatrix}, \quad \mathbf{A} = \begin{bmatrix} A_{11} & \dots & A_{1m} \\ A_{21} & \dots & A_{2m} \\ \vdots & \vdots & \vdots \\ A_{m1} & \dots & A_{mm} \end{bmatrix}. \tag{3.50}$$

The system (3.60) is said to be *linear with constant coefficients* if the elements of the matrix **A** are all constant and also the components of the vector **S**. If the matrix **A** is a function of the vector **U** the system is then called *quasi-linear.* This system is said to be hyperbolic at a point (x,t) if the matrix **A** has m real eigenvalues λ_1,...,λ_m and a corresponding set of linearly independent right eigenvectors $\mathbf{K}^{(1)}$,...,$\mathbf{K}^{(m)}$.

3.5.1 Conservation Laws

A system of hyperbolic partial differential equations is said to be a system of *conservation laws* if can be written in the following form

$$\partial_t \mathbf{U} + \partial_x \mathbf{F}(\mathbf{U}) = 0, \tag{3.51}$$

where $\mathbf{U} = (U_1, U_2, ..., U_m)^T$ is called the vector of conserved variables and the vector of fluxes is $\mathbf{F}(\mathbf{U}) = (F_1(U_j), F_2(U_j), ..., F_m(U_j))^T$, where $j = 1, ..., m$. The *Jacobian* matrix is defined by

$$\mathbf{A}(\mathbf{U}) = \frac{\partial \mathbf{F}}{\partial \mathbf{U}} = \begin{bmatrix} \frac{\partial F_1}{\partial U_1} & \cdots & \frac{\partial F_1}{\partial U_m} \\ \frac{\partial F_2}{\partial U_1} & \cdots & \frac{\partial F_2}{\partial U_m} \\ \vdots & \vdots & \vdots \\ \frac{\partial F_m}{\partial U_1} & \cdots & \frac{\partial F_m}{\partial U_m} \end{bmatrix}. \tag{3.52}$$

3.5.2 Characteristics

Let us consider a scalar linear advection equation in one dimension

$$\partial_t U + a \partial_x U = 0, \tag{3.53}$$

with initial conditions at time $t = 0$ given by

$$U^{(0)}(x) \equiv U(x, 0) \tag{3.54}$$

Characteristic or *characteristic curves* are curves $x = x(t)$ in the $t - x$ plane along which the partial differential equation becomes and ordinary differential equation. The rate of change of U along $x = x(t)$ is

$$\frac{dU}{dt} = \frac{\partial U}{\partial t} + \frac{dx}{dt}\frac{\partial U}{\partial x}, \tag{3.55}$$

if the characteristic curve satisfies

$$\frac{dx}{dt} = a, \tag{3.56}$$

then from equations (3.53) and (3.63) we obtain

$$\frac{dU}{dt} = \frac{\partial U}{\partial t} + a\frac{\partial U}{\partial x} = 0. \tag{3.57}$$

Thus U is constant along the characteristic curve $x = x(t)$. Then given an initial profile $U(x,0) = U^{(0)}(x)$, the solution along the characteristic curve $x(t) = x_0 + at$ that passes through the initial point x_0 on the x-axis is given by

$$U(x,t) = U^{(0)}(x_0) = U^{(0)}(x - at). \tag{3.58}$$

3.5.3 Riemann Problem

A Riemann problem for the system of conservation laws (3.71) is an initial value problem with the following initial conditions

$$\mathbf{U}(x,0) = \begin{cases} \mathbf{U}_L & \text{if} \quad x < 0, \\ \mathbf{U}_R & \text{if} \quad x > 0, \end{cases} \tag{3.59}$$

where $\mathbf{U}_L$ (left) and $\mathbf{U}_R$ (right) are two constant values as shown in the top panel of Fig. 3.1. In the general case of a non-linear set of hyperbolic equations, the solution of the Riemann problem consists of three different type of wave solutions: a shock, a rarefaction and a contact discontinuity which represent some of the possible wave patterns as shown in the bottom panel of Fig. 3.1. The rarefaction moves into the high density region in the opposite direction to the shock wave which moves into the less dense region, giving to two new constant states,$\mathbf{U}_L^*$ and $\mathbf{U}_R^*$, separated from each other by a contact discontinuity. Across the contact discontinuity the pressure and velocity will be continuous but the density will be discontinuous. Finding a solution to a Riemann problem involves finding the values for the fields (density, velocity and pressure) at the two intermediate states.

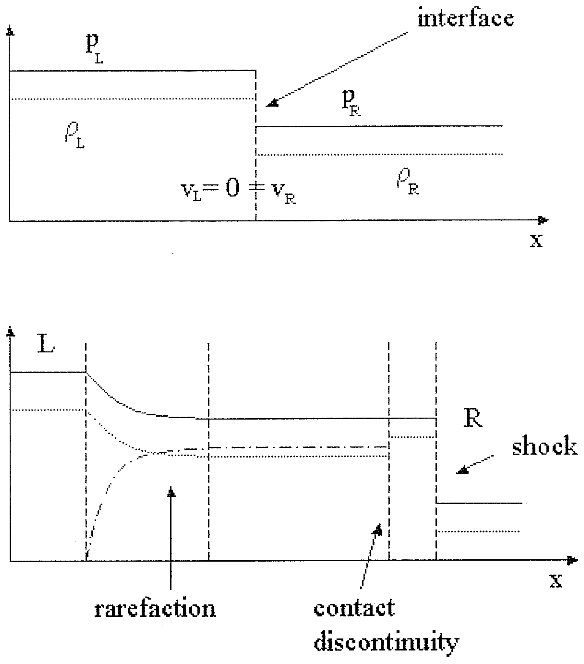

Figure 3.1: Schematic representation of the initial data for a Riemann problem in the top panel and its solution (bottom panel), showing the rarefaction, contact discontinuity and shock waves between the left(L) and right(R) states for the density (dotted line), pressure (solid line) and velocity (dashed line).

3.5.4 Characteristic Variables

Let us consider a homogeneous linear hyperbolic system of m partial differential equations of the form

$$\partial_t \mathbf{U} + \mathbf{A}\partial_x \mathbf{U} = 0. \tag{3.60}$$

From the condition of hyperbolicity $\mathbf{A}$ has a set of m real eigenvalues λ_i and a set of m right eigenvectors $\mathbf{K}^{(i)}$ such that the matrix $\mathbf{A}$ can be expressed as

$$\mathbf{A} = \mathbf{K}\mathbf{M}\mathbf{K}^{-1}, \tag{3.61}$$

with

$$\mathbf{K} = \left[\mathbf{K}^{(1)}, ..., \mathbf{K}^{(m)}\right], \quad \mathbf{M} = \begin{bmatrix} \lambda_1 & \dots & 0 \\ 0 & \dots & 0 \\ \vdots & \vdots & \vdots \\ 0 & \dots & \lambda_m \end{bmatrix}, \tag{3.62}$$

where $\mathbf{M}$ is a diagonal matrix. Within this framework, *Characteristic variables* $\mathbf{W} = (W_1, W_2, ..., W_m)^T$ are defined by

$$\mathbf{W} = \mathbf{K}^{-1}\mathbf{U}. \tag{3.63}$$

In terms of the characteristic variables, the system (3.60) becomes decoupled and can be written as

$$\mathbf{K}\partial_t \mathbf{W} + \mathbf{A}\mathbf{K}\partial_x \mathbf{W} = 0 \quad \textit{or} \quad \partial_t \mathbf{W} + \mathbf{M}\partial_x \mathbf{W} = 0. \tag{3.64}$$

The solution of this system of equations with initial data $\mathbf{W}^0 = (W_1^{(0)}, W_2^{(0)}, ..., W_m^{(0)})^T$ is simply (recall Eq. (3.58))

$$W_i(x,t) = W_i^{(0)}(x - \lambda_i t) \ , \ \text{for } i = 1, ..., m, \tag{3.65}$$

so that the solution in terms of the original variables is obtained using Eq. (3.63) as

$$\mathbf{U}(x,t) = \sum_{i=1}^{m} W_i(x,t)\mathbf{K}^{(i)}. \tag{3.66}$$

3.6 Overview to High Resolution Shock Capturing (HRSC) Methods

3.6.1 Introduction to Finite Difference Approximation to Derivatives

In *finite difference* methods, continuous problems are discretized so that the domain of the partial differential equation (PDE) is replaced by a finite set of points or *grid.* Continuous functions are represented by a set of discrete values at successive grid points. That is, any continuous function $u(x)$, is replaced by a set of discrete values $u_i \equiv u(x_i)$, where $x_i = x_0 + i\Delta x$ $(i = 1, 2, ..., I)$ represent the i-th point of a grid having spacing Δx.

Derivative operators are approximated by finite difference expressions based on a Taylor series. The function $u(x)$ at the neighboring point $x_0 + \Delta x$ of $x = x_0$ can be expressed as the following Taylor series

$$u(x_0 + \Delta x) = u(x_0) + \sum_m \frac{(\Delta x)^m}{m!} u^{(m)}(x_0), \tag{3.67}$$

where $u^{(m)}(x_0)$ is the m-th derivative of $u(x)$ at $x = x_0$. By truncating the series (3.67) and solving for the derivative we can obtain finite difference approximations for the derivative operator. For example, by neglecting second-order terms of (3.67) we can approximate the first derivative to a first-order *forward* finite difference approximation

$$u^{(1)}(x_0) = \frac{u(x_0 + \Delta x) - u(x_0)}{\Delta x} + O(\Delta x). \tag{3.68}$$

Similarly, by expanding $u(x)$ at $x_0 - \Delta x$ we can obtain a *backward* first-order approximation

$$u^{(1)}(x_0) = \frac{u(x_0) - u(x_0 - \Delta x)}{\Delta x} + O(\Delta x), \tag{3.69}$$

and neglecting third-order and higher terms in the expansions of $u(x)$ at $x_0 + \Delta x$ and $x_0 - \Delta x$ and subtracting the resultant expressions yields to a second-order central finite approximation

$$u^{(1)}(x_0) = \frac{u(x_0 + \Delta x) - u(x_0 - \Delta x)}{2\Delta x} + O(\Delta x^2). \tag{3.70}$$

3.6.2 Godunov's Schemes

Let us consider for simplicity a 1-dimensional hyperbolic system of partial differential equations in conservation law form

$$\partial_t \mathbf{U} + \partial_x \mathbf{F}(\mathbf{U}) = 0, \tag{3.71}$$

where $\mathbf{U}$ is the vector of unknowns and $\mathbf{F}(\mathbf{U})$ is the vector of fluxes. It is also possible to write (3.71) in the following integral form

$$\frac{d}{dt}\int_{x_1}^{x_2} \mathbf{U} dx = \mathbf{F}(\mathbf{U}(x_1,t)) - \mathbf{F}(\mathbf{U}(x_2,t)). \tag{3.72}$$

In order to solve this equation numerically we must first discretize the unknowns $\mathbf{U}(x,t)$ in space and time such that these are approximated by some discrete values $\mathbf{U}_i^n \equiv \mathbf{U}(x = x_i, t = t_n)$.

In Fig. 3.2 we show the values of the function $U(x)$ at grid points represented with solid circles. The interface between adjacent cells is represented by solid vertical lines while horizontal dashed lines in each cell refer to an averaged representation of the function $U(x)$ within the cell. The average value of $\mathbf{U}(x)$ at time $t = t_n$ over the cell $I_i = [x_{i-1/2}, x_{i+1/2}]$ is computed by

$$\mathbf{U}_i^n \equiv \frac{1}{\Delta x}\int_{x_{i-1/2}}^{x_{i+1/2}} \mathbf{U}(x, t^n) dx. \tag{3.73}$$

This set of cell averages defines a piecewise constant representation of $\mathbf{U}(x,t)$. From the integral conservation form (3.72) with $x_1 = x_{i-1/2}$ and $x_2 = x_{i+1/2}$ we obtain the algorithm in conservative form

$$\mathbf{U}_i^{n+1} = \mathbf{U}_i^n - \frac{\Delta t}{\Delta x}\left(\mathbf{f}_{i-\frac{1}{2}} - \mathbf{f}_{i+\frac{1}{2}}\right), \tag{3.74}$$

where we have used the following definition

$$\mathbf{f}_{i\pm1/2} \equiv \frac{1}{\Delta t}\int_{t^n}^{t^{n+1}} \mathbf{F}(\mathbf{U}(x_{i\pm1/2}, t)) dt. \tag{3.75}$$

The quantity $\mathbf{f}_{i\pm1/2}$, known as *intercell fluxes*, are time averages of the physical flux $\mathbf{F}(\mathbf{U})$ at the cell interfaces. As shown in Fig. 3.2, discretization and piecewise constant representation of $\mathbf{U}(x)$ sets up a local Riemann problem at each of the cell interfaces. Therefore, by solving these sequences of local Riemann problems we can obtain the quantities $\mathbf{U}(x_{i\pm1/2}, t)$ needed

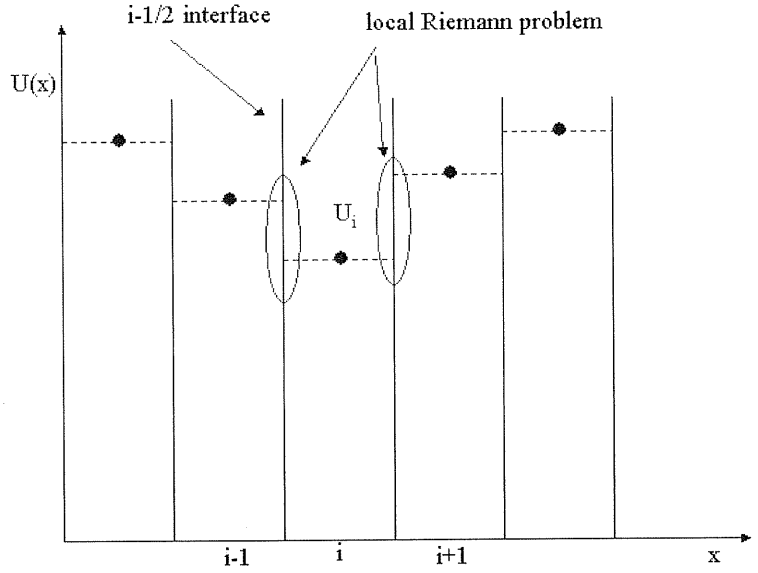

Figure 3.2: Discretization of function U and piecewise constant representation of the U within the cell sets up the initial data for local Riemann problems at the interfaces between adjacent cells

to compute the intercell fluxes (*cf.* Eq. (3.75)). Then, the solution $\mathbf{U}_i^n$ of the system of equations is updated forward in time to $\mathbf{U}_i^{n+1}$.

The Godunov's method (Godunov 1959) assumes the data to be piecewise constant within each numerical cell and computes the intercell fluxes by solving the local Riemann problem at the cell interfaces. If we apply Eq. (3.74) to the linear advection equation (3.53), *i.e.* $F = aU$, and solve the local Riemann problems as described in Section 3.5, we obtain that the intercell flux at the cell interface $x_{i+1/2}$, for the case in which $a > 0$, is given by

$$f_{i+1/2} = aU_i. \tag{3.76}$$

We note that Godunov's method gives only first order accuracy. More accurate approximations to the left and right states setting up the Riemann problem will increase the accuracy of the scheme. Thus, higher order modifications of Godunov's method (HRSC schemes) are based on different *reconstruction* schemes that aim to increase the accuracy on smooth parts of the solution (second order or higher) and allow for high resolution of shocks without producing spurious oscillations in the vicinity of large gradients.

3.6.3 Reconstruction Methods: MC Slope Limiter

Since the accuracy of the spatial differencing is determined by the order of the extrapolation used to compute the values at the cell interfaces, we have implemented in the `Nada` code a class of second order accurate scheme based on piecewise linear interpolation, the so called *slope limiter methods.* These schemes are simpler to implement than piecewise parabolic methods (which are third order accurate) and still resolve the discontinuities well and minimize the appearance of spurious oscillations. In our implementation of the slope limiter, the left and right states of a given grid function at the cell interface are obtained by means of monotonic piecewise linear reconstruction computed as follows

$$\mathbf{U}_{i+1/2}^L = \mathbf{U}_i + \sigma_i(x_{i+1/2} - x_i), \tag{3.77}$$

$$\mathbf{U}_{i+1/2}^R = \mathbf{U}_{i+1} + \sigma_{i+1}(x_{i+1/2} - x_{i+1}), \tag{3.78}$$

where σ_i is the slope computed from the slope limiting function. The so called *monotonized central-difference* (MC) limiter by B. J. Van Leer (1977) computes the slope by

$$\sigma_i = \mathrm{MC}(\mathbf{s}_{i-1/2}, \mathbf{s}_{i+1/2}), \tag{3.79}$$

where

$$\mathbf{s}_{i+1/2} = \frac{\mathbf{U}_{i+1} - \mathbf{U}_i}{x_{i+1} - x_i}, \tag{3.80}$$

and

$$MC(a,b) = \begin{cases} 0 & \text{if} \quad ab \leq 0 \\ 2a & \text{if} \quad |a| < |b| \quad \text{and} \quad 2|a| < |c| \quad \text{and} \quad ab > 0 \\ 2b & \text{if} \quad |a| > |b| \quad \text{and} \quad 2|b| < |c| \quad \text{and} \quad ab > 0 \\ c & \text{if} \quad |c| < 2|a| \quad \text{and} \quad |c| < 2|b| \quad \text{and} \quad ab > 0, \end{cases} \tag{3.81}$$

with $c \equiv (a+b)/2$. At the local extrema of the function the limited slopes are equal to 0. Thus, reducing the scheme to first order at there.

This scheme is said to be *total variation diminishing* (TVD). That is, defining the concept of *total variation* (TV) of a solution at time $t = t^n$ as

$$TV(\mathbf{U}^n) = \sum_{i=0}^{\infty} |\mathbf{U}^n_{i+1} - \mathbf{U}^n_i|, \tag{3.82}$$

a TVD scheme ensures that the variation of the solution at any time is always bounded by the total variation of the initial data

$$TV(\mathbf{U}^{n+1}) \leq TV(\mathbf{U}^n). \tag{3.83}$$

In practice, Eq. (3.83) ensures that the solution in non-oscillatory.

3.6.4 Riemann Solvers

Once a reconstruction scheme has computed the data on either side of each cell interface, these are then used to specify the initial states of the Riemann problems. Although the solution of a general Riemann problem cannot be given in a closed analytic form, it is possible to find a solution numerically to any required accuracy. This solution is referred to as the *exact* solution of a Riemann problem, even it is not an analytical one. In Newtonian hydrodynamics, the exact solution of the one-dimensional Riemann problem can be found in *e.g.* Courant & Friedrichs (1976). In the case of special relativistic hydrodynamics (Martí & Müller; 1999), the exact solution, for the case of pure normal flow, was derived by Martí & Müller (1994), generalizing the solution obtained by Thompson (1986) for zero initial velocities. Pons et al. (1998), taking advantage of the local flatness of a curved spacetime, generalized this special relativistic Riemann solver in general relativistic hydrodynamics. A general solution for the case of non-zero tangential velocities in relativistic hydrodynamics has been obtained by Pons et al. (2000). Recently, Rezzolla & Zanotti (2001) and Rezzolla, Zanotti & Pons (2003) have presented a new approach for the solution of exact Riemann problems in relativistic hydrodynamics which focusses on the relativistic invariant relative velocity between the two unperturbed initial states of the fluid.

However, although it is possible to find an exact solution of the Riemann problem at every cell interface, this is not computationally efficient and several different *approximate Riemann solvers* have been developed. These are computationally less expensive and yet give very satisfactory results. Next, we discuss the three approximate flux Riemann solvers (*i.e.* give a direct approximation to the intercell flux rather than to the state $\mathbf{U}(x_{i\pm1/2}, t)$) and that we have implemented in the `Whisky` code.

HLLE solver

The Harten, Lax, van Leer and Einfeldt (HLLE; Harten et al. 1983, Einfeldt 1988) solver approximates the solution of the Riemann problem as three constant states separated by two waves. In this approach, the solution takes the following form

$$\mathbf{U} = \begin{cases} \mathbf{U}_L & \text{if} \quad x/t < \xi_{min}, \\ \mathbf{U}_* & \text{if} \quad \xi_{min} < x/t < \xi_{max}, \\ \mathbf{U}_R & \text{if} \quad x/t > \xi_{max}, \end{cases} \tag{3.84}$$

where ξ_{min} and ξ_{max} are the minimum and maximum characteristic velocities obtained from the solution of the Riemann problem. In practice, these are taken to be the smallest and largest eigenvalues of the Jacobian matrix (*cf.* Eq. 3.52) evaluated at both the left and right state of each cell interface. The numerical flux is given by

$$\mathbf{f}^{HLLE} = \frac{\xi_{max}\mathbf{F}(\mathbf{U}_L) - \xi_{min}\mathbf{F}(\mathbf{U}_R) + \xi_{min}\xi_{max}(\mathbf{U}_R - \mathbf{U}_L)}{\xi_{max} - \xi_{min}}. \tag{3.85}$$

The main advantage of the scheme is its simple implementation since it does not require full knowledge of the spectral decomposition of the Jacobian matrix as it makes only use of the eigenvalues, unlike Roe's solver or the Marquina flux formula that require the right and left eigenvectors. This method is very stable but also diffusive.

Roe solver

The Riemann solver implemented in our numerical code, the approximate Riemann solver of Roe (Roe 1981) which is a common choice among the various approximate solvers in numerical relativistic hydrodynamics and has been applied to a large variety of physical problems.

Applying the chain rule to the conservation law (3.71) we can rewrite it in terms of the Jacobian matrix, $\mathbf{A}(\mathbf{U}) = \partial\mathbf{F}/\partial\mathbf{U}$, as

$$\partial_t\mathbf{U} + \mathbf{A}(\mathbf{U})\partial_x\mathbf{U} = \mathbf{S}(\mathbf{U}). \tag{3.86}$$

Roe's solver replaces the Jacobian matrix, $\mathbf{A}(\mathbf{U})$, by a constant matrix, $\tilde{\mathbf{A}} = \tilde{\mathbf{A}}(\mathbf{U_L}, \mathbf{U_R})$, which transforms the original conservation law into a linear system with constant coefficients

$$\partial_t\mathbf{U} + \tilde{\mathbf{A}}\partial_x\mathbf{U} = \mathbf{S}(\mathbf{U}). \tag{3.87}$$

Roe's conditions for the stability of the numerical flux are:

- $\tilde{\mathbf{A}}(\mathbf{U_L}, \mathbf{U_R})(\mathbf{U_R} - \mathbf{U_L}) = \mathbf{F}(\mathbf{U_R}) - \mathbf{F}(\mathbf{U_L})$, which ensures conservation across the discontinuities.
- $\tilde{\mathbf{A}}(\mathbf{U}, \mathbf{U}) = \mathbf{A}(\mathbf{U})$, which guarantees consistency with the exact Jacobian matrix.
- $\tilde{\mathbf{A}}$ must have real eigenvalues, $\tilde{\lambda}_q$, and a complete set of linearly independent right eigenvectors, $\tilde{\mathbf{K}}^{(q)}$, so that hyperbolicity of the system is ensured.

In practice the numerical fluxes across the cell interfaces computed by the Roe flux are given by

$$\mathbf{f}^{Roe}_{i+1/2} = \frac{1}{2}\left[\mathbf{F}(\mathbf{U}_R) + \mathbf{F}(\mathbf{U}_L) - \sum_{q=1}^{p} |\tilde{\lambda}_q|\Delta\tilde{\omega}_q\tilde{\mathbf{K}}^{(q)}\right], \tag{3.88}$$

where the quantities $\Delta\tilde{\omega}_q$ are the jump of the characteristic variables and are computed from

$$\mathbf{U}_R - \mathbf{U}_L = \sum_{q=1}^{p} \Delta\tilde{\omega}_q \tilde{\mathbf{K}}^{(q)}. \tag{3.89}$$

Marquina solver

The third method for computing the numerical fluxes is the Marquina flux formula proposed by Donat & Marquina (1996); Donat et al. (1998) which does not solve the Riemann problem completely but gives a direct approximation to the flux. This method combines the Roe numerical flux and a Lax-Friedrichs method at the sonic points that acts as an entropy fix to the Roe flux. The Marquina flux formula computes the characteristic flux in different ways depending on whether the eigenvalues associated to the left and right states have the same sign or not.

In the `Whisky` code we have actually implemented the so called modified Marquina scheme introduced by Aloy et al. (1999) instead of the original method as this new algorithm does not involve any *if*-clause corresponding to the sign of the eigenvalues and it has proved more stable. In this version of Marquina's flux formula the numerical fluxes at each cell interface are given by

$$\mathbf{f}^{Marq} = \frac{1}{2}\left[\mathbf{F}(\mathbf{U}_R) + \mathbf{F}(\mathbf{U}_L) + (\mathbf{Q}^R - \mathbf{Q}^L)\right], \tag{3.90}$$

where the quantities $\mathbf{Q}^S (S = L, R)$ are defined in the following way

$$Q_j^S = \sum_{i,k=1}^{5} |\lambda_i|_{max(L,R)}\, r_{ji}^S\, l_{ik}^S\, U_k^S, \qquad (j = 1, ..., 5). \tag{3.91}$$

Here the quantities $|\lambda_i|_{max(L,R)}$ $(i = 1, ..., 5)$ are the maxima of the moduli of the two corresponding eigenvalues at the left and right side of the interface, r_i^S and l_i^S with $i = (1, ..., 5)$ represent the corresponding eigenvectors at the right and left of the interface, respectively.

3.7 Relativistic Hydrodynamic Equations in Conservation Form

As mentioned in Section 3.3, the metric in the 3+1 decomposition is expressed as a function of the spatial 3-metric on each slice Σ_t, γ_{ij}, the lapse α and the shift vector β^i as

$$ds^2 = -\alpha^2 dt^2 + \gamma_{ij}\left(dx^i + \beta^i dt\right)\left(dx^j + \beta^j dt\right). \tag{3.92}$$

Eulerian observers, at rest in the slice Σ_t, measure the velocity of the fluid as

$$v^i = \frac{u^i}{\alpha u^t} + \frac{\beta^i}{\alpha}. \tag{3.93}$$

where $\mathbf{u}$ is the four velocity of the fluid. The Lorentz factor is defined as $W \equiv (1 - \gamma_{ij} v^i v^j)^{-1/2}$. Then, defining a new set of variables, the conserved variables $\mathbf{U}(\mathrm{w}) = (D, S_j, \tau)$, which are written in terms of the primitive hydrodynamic variables $\mathbf{w} = (\rho, v_i, \epsilon)$ as

$$\begin{aligned} D &= \rho W, \\ S_j &= \rho h W^2 v_j, \\ \tau &= \rho h W^2 - P - D, \end{aligned} \tag{3.94}$$

the relativistic hydrodynamic equations can be written a first-order flux conservative form (Martí et al., 1991; Banyuls et al., 1997; Ibáñez et al., 1998, 2001) as

$$\frac{1}{\sqrt{-g}}\left(\frac{\partial\sqrt{\gamma}\mathbf{U}(\mathrm{w})}{\partial t} + \frac{\partial\sqrt{-g}\mathbf{F}^i(\mathrm{w})}{\partial x^i}\right) = \mathbf{S}(\mathrm{w}), \tag{3.95}$$

where $g \equiv det(g_{\mu\nu})$ and $\sqrt{-g} = \alpha\sqrt{\gamma}$ ($\gamma \equiv det(\gamma_{ij})$). The vectors of fluxes, $\mathbf{F}^i(\mathrm{w})$ are given by

$$\mathbf{F}^i(\mathrm{w}) = \left[D\left(v^i - \frac{\beta^i}{\alpha}\right), S_j\left(v^i - \frac{\beta^i}{\alpha}\right) + P\delta^i_j, \tau\left(v^i - \frac{\beta^i}{\alpha}\right) + Pv^i\right], \tag{3.96}$$

and the vector of sources is given

$$\mathbf{S}(\mathrm{w}) = \left[0, T^{\mu\nu}\left(\frac{\partial g_{\nu j}}{x^\mu} - \Gamma^\delta_{\nu\mu} g_{\delta j}\right), \alpha\left(T^{\mu 0}\frac{\partial \ln\alpha}{\partial x^\mu} - T^{\mu\nu}\Gamma^0_{\nu\mu}\right)\right]. \tag{3.97}$$

In order to close this system of equations for the hydrodynamics an equation of state which relates the pressure to the rest-mass density and to the energy density must be specified.

3.8 3D General Relativistic Hydrodynamics: the "Whisky" Code

While the previous Sections served as an introduction to numerical relativity and relativistic hydrodynamics, the following Sections of this Chapter will be dedicated to my contributions to the development of a new 3D evolution code, the `Whisky` code, that solves the general relativistic hydrodynamic equations on a three dimensional numerical grid with Cartesian coordinates. The `Whisky` code has been developed in a collaboration of several European research institutes and universities (SISSA, the Albert Einstein Institute in Germany, the University of Valencia in Spain and the University of Thessaloniki in Greece) joint under the EU Network on *Sources of Gravitational Waves.* This code has been constructed within the framework of the `Cactus Computational Toolkit`, developed at the Albert Einstein Institute (Golm) and at Louisiana State University (Baton Rouge), taking advantage of the high-level facilities that the `Cactus` code provides such as parallelization, input/output, portability to different platforms and the availability of several evolution schemes to solve general systems of partial differential equations. The `Cactus` code also provides the solution of the full set of Einstein equations and the coupling between this system of equations and the hydrodynamic equations is done using the method of lines approach, described earlier. While the `Whisky` code is entirely new, its initial development has benefitted in part from the release of a public version of the general relativistic hydrodynamics code described in Font et al. (2000a) and Font et al. (2002c), and developed mostly by the group at the Washington University at St. Louis.

Most of the basics of the numerical schemes that the `Whisky` code uses to solve the hydrodynamic equations, *i.e.* the HRSC schemes, have already been discussed in this Chapter, so we will simply review the main aspects which make this evolution code one of the most advanced currently used in numerical relativistic hydrodynamics. Moreover, the

`Whisky` code incorporates many different schemes which have been implemented by several people so it is very much the result of a common effort. After summarizing the major features of the code, we will point out our main contributions to its development. Next, we will discuss numerical simulations of non-selfgravitating geometrically thick accretion discs orbiting around black holes and show that the available computational resources make this problem extremely difficult with the current 3D codes.

3.9 Structure of the Whisky Code

One on the important features of the `Whisky` code is the implementation of the *conservative formulation* of the general relativistic hydrodynamic equations proposed by Banyuls et al. (1997), in which the set of general relativistic equations is written in a hyperbolic, first-order and flux-conservative form. The explicit expressions of the equations implemented in the code can be found in Font et al. (2003). In order to write system of the local conservation of the baryon number and of the energy-momentum in the conservation form (see Section 3.7) the primitive hydrodynamic variables (rest-mass density ρ, 3-velocity v^i and specific internal energy ϵ) are mapped to the conserved variables $\mathbf{U} \equiv (D, S^i, \tau)$.

The code has been written to use any equation of state. Simulations shown in the following Sections have been carried out using either an (isentropic) polytropic equation of state

$$P = k\rho^{\Gamma} \ , \tag{3.98}$$

or an “ideal fluid” equation of state

$$P = (\Gamma - 1)\rho\epsilon \ . \tag{3.99}$$

Here, k is the polytropic constant and Γ is the adiabatic index. We note that the polytropic equation of state is suitable for numerical simulations involving regular flows but not for ones involving shocks since it assumes that the specific entropy remains constant and in the case, it is not necessary to solve the evolution equation for τ. In the case of the ideal-fluid equation of state (3.99), on the other hand, non-isentropic changes can take place in the fluid and the evolution equation for τ needs to be solved. In addition to these equations of state, a "hybrid" equation of state (suitable for core collapse simulations), as described in Zwerger et al. (1995 & 1997) and a tabulated realistic equation of state have recently been implemented.

For further details of the formulation of the equations implemented in the `Whisky` code we refer to Font et al. (2003). We stress that an important feature of this formulation is that it has allowed to extend to a general relativistic context the powerful numerical methods developed in classical hydrodynamics, the HRSC schemes. As we have already discussed, these schemes are essential for the correct representation of shocks since these schemes can resolve accurately discontinuities while avoiding the formation of non-physical oscillations. The `Whisky` code is a general purpose code which offers users a choice of methods. For a detailed description of the numerical methods for the solution of the hydrodynamic equations we refer to Baiotti et al. (2003). Here we list the main features of the code:

1.- Reconstruction methods:

(i) Piecewise Parabolic Method (PPM, Collela & Woodward 1984).

(ii) Essentially Non-Oscillatory (ENO, Harten et al., 1987; Shu 1999)

(iii) MC slope limiter (van Leer 1977).

2.- Approximate Riemann solvers :

(i) The Harten-Lax-van Leer-Einfeldt (HLLE) solver.

(ii) Roe's approximate solver.

(iii) The Marquina flux formula.

3.- Left eigenvectors : The code uses analytic expressions for the left eigenvectors (Ibáñez et al. 2001), thereby avoiding the computationally expensive inversion of the three 5×5 matrices of the right eigenvectors, associated to each spatial direction. This implementation brings a $\sim 40\%$ reduction of the computational time spent in the solution of the hydrodynamic equations.

4.- Time integration : This follows the "method of lines" (MoL) approach for the implementation of high-order time evolution schemes. There are several ODE methods available such as Runge-Kutta schemes of different order and an iterative Crank-Nicholson method (ICN).

5.- Coupling to spacetime: The code allows for the possibility to couple the general relativistic hydrodynamic equations with the full set of Einstein's equations. In this case, the solution of the Einstein equations is provided by the `Cactus` code which implements this system of equations following the 3+1 formalism and the integration forward in time is done by means of the *method of lines* (Toro 1999)

Contributions to Whisky

In general, our main contributions to the `Whisky` code consist of the implementation of approximate Riemann solvers (HLLE, Roe and Marquina flux formula) described in Section 3.6.4 as well as in the testing of the code under several different conditions.

3.10 Numerical Tests of the Whisky Code

Several numerical tests have been performed to assess the accuracy and stability of the `Whisky` code which I have taken part in 2002. Firstly, we have carried out a series of shock-tube tests which aim to establish the ability of our code to resolve discontinuities. Secondly, we have investigated the dynamics of neutron stars both in the Cowling approximation, where the spacetime is held fixed, and in full evolutions which solve the hydrodynamic equations together with the full set of Einstein equations which also allow checking of the coupling between the `Whisky` and the `Cactus` codes.

3.10.1 Shock-tube Test

We have first tested the `Whisky` hydrodynamic code and the performance of the different approximate Riemann solvers which we have implemented by means of a simple shock-tube test along a principal coordinate direction. The initial data for the left state is $P_L = 13.33, \rho_L = 10.00, v_L = 0.00$ and for the right state $P_R = 0.66 \times 10^{-6}, \rho_R = 1.00, v_R =$

0.00. The fluid is assumed to be an ideal fluid with an equation of state $P = (\Gamma - 1)\rho\epsilon$ with $\Gamma = 5/3$. The following series of panels in Fig. 3.3 shows the solution of the shock-tube test along the x-direction, where the left and right states are separated by an interface located at $x = 0$, with the HLLE, Roe and Marquina solvers. The computational domain goes from -0.5 to 0.5 and we have used 200 grid points along the x-direction. We used the method of lines and the ICN iterative scheme to integrate the hydrodynamic equations in time. In order to compare the results from each of the different Riemann solvers, we used the same reconstruction scheme (van Leer reconstruction scheme) for all of these simulations. The first three panels at the top in Fig. 3.3 correspond to results for each of the hydrodynamic variables obtained with the HLLE solver, the middle three are for the Roe solver and the bottom three for the Marquina solver. The exact solution of this Riemann problem is represented with a solid line. We observe that the agreement with the exact solution is very good for all the hydrodynamic variables with all the three approximate solvers. Equivalent results have also been obtained along the y and the z directions.

Next, we solved this 1-dimensional problem along the diagonal of the cubic computational grid, placing the initial interface separating the left and right states orthogonal to the diagonal. In this way, the numerical fluxes along all of the directions are required, allowing for assessing the performance of the approximate solvers in all directions simultaneously. Fig. 3.4 shows the numerical solution (we have used 140^3 grid points) for the hydrodynamical variables and the exact solution. Again, the agreement between the two is very good.

3.10.2 Relativistic Spherical Stars

We have used the solution of the Tolman-Oppenheimer-Volkoff equations (Tolman 1939; Oppenheimer & Volkoff 1939; hereafter TOV) for a static spherically symmetric star to test the stability of the `Whisky` code in evolving stable relativistic spherical stars. In order to assess the performance of the hydrodynamic code on its own, we have evolved a TOV star in a fixed spacetime. The upper panel in Fig. 3.5 shows the time evolution of the central rest-mass density normalized to the initial value for a model with mass $M = 1.4$, polytropic constant $k = 100$ and polytropic index $\Gamma = 2$ (in units $c = G = M_\odot = 1$).

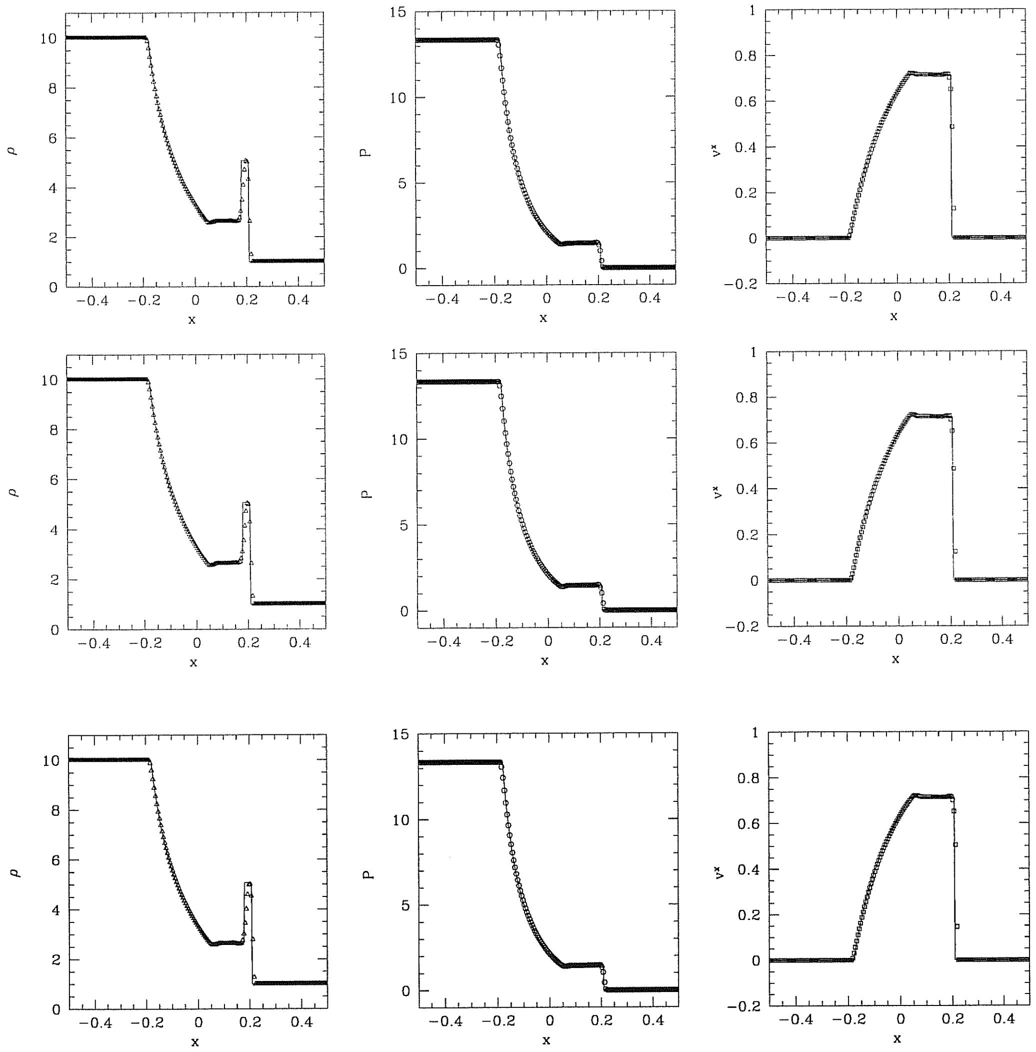

Figure 3.3: Solution of a Riemann problem along the x-direction. The figure shows the comparison between the hydrodynamical variables, indicated with symbols, and the exact solution, represented with a solid line. The numerical simulation was obtained with van Leer reconstruction method and the ICN integration scheme using 200 grid points along x.

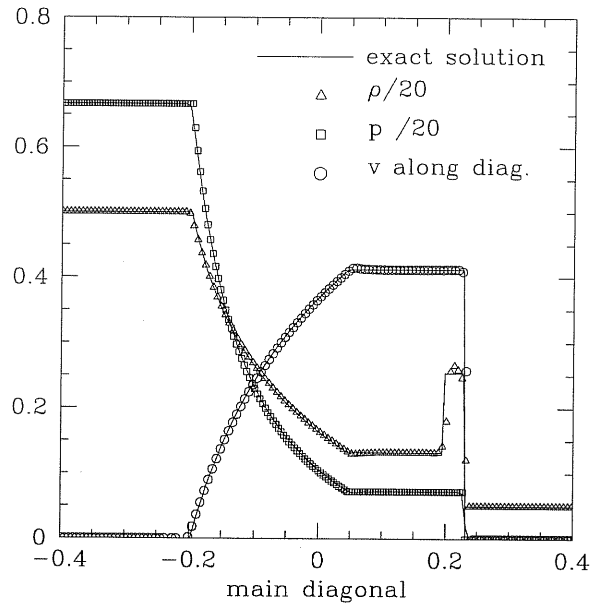

Figure 3.4: Solution of a Riemann problem set on the main diagonal of the cubic grid. The figure shows the comparison between the hydrodynamical variables evolved by `Whisky`, indicated with symbols, and the exact solution. The numerical simulation was carried out with the van Leer reconstruction method and the Roe solver, on a 140^3 grid.

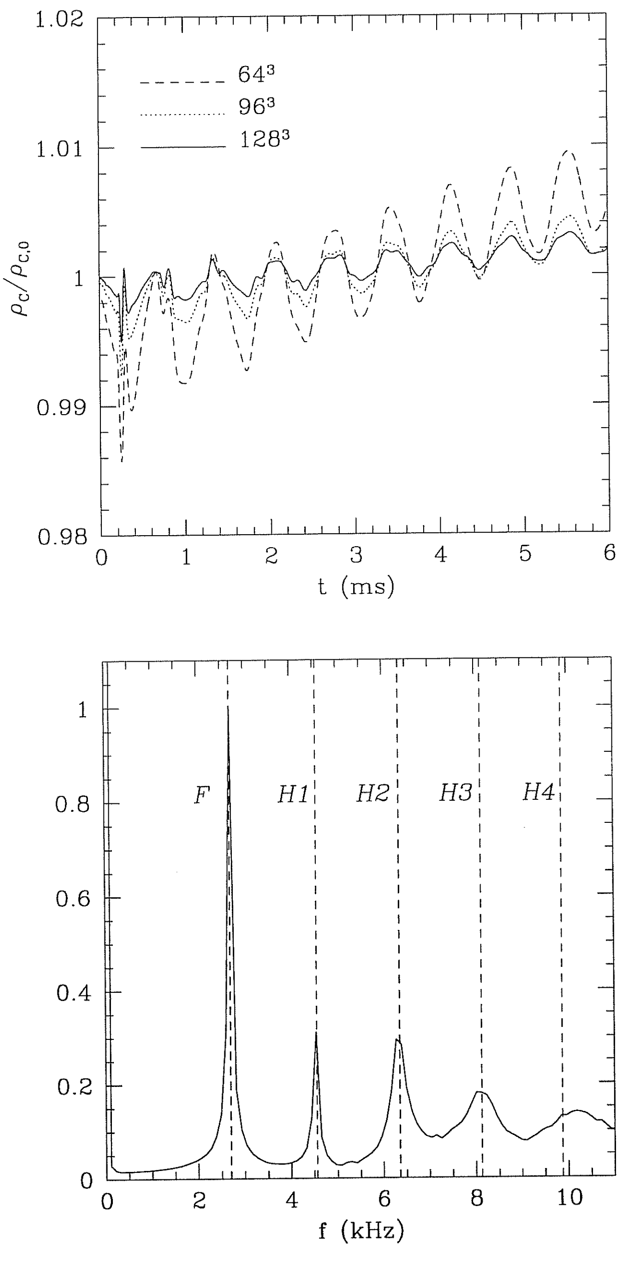

Figure 3.5: The top panel shows the value of central rest-mass density, normalized to the initial value, for the evolution of a stable TOV star ($M = 1.4\,M_\odot$ and polytropic index $\Gamma = 2$) in a fixed spacetime with different resolutions. PPM and Marquina were used for all runs. The bottom panel shows the power spectrum of the evolution of the central rest-mass density of the same stable TOV star performed with 128^3 grid points. The units of the vertical axis are arbitrary.

We note that with increasing resolution the truncation error is reduced and the amplitude of the oscillation decreases. The convergence rate is slightly less than second-order as the reconstruction schemes are only first-order at the centre and the surface of the star. The lower panel shows the power spectrum of the central mass-density evolution for the same stable TOV star. We have compared the frequencies of the fundamental mode and the first overtones with those obtained with an independent 2D code by Font et al. (2000b) and the agreement is very good with a relative error in the fundamental mode of less than 1%. We have also successfully performed several TOV tests in dynamical spacetimes which confirmed the accuracy of our 3D code and the approximately second-order convergence rate (these tests are treated in detail in Baiotti et al. 2003). During 2003-2004 the `Whisky` code has been further developed and tested, with new important features being added recently, in fact, the code has been successfully used for simulations of rapidly rotating stable neutron stars and in the collapse of rotating neutron stars to form Kerr black holes (Baiotti et al. 2004).

3.11 Simulations of Non-Selfgravitating Accretion Tori around Schwarzschild Black Holes

Based on the analytical theory of thick discs orbiting around black holes (Kozlowski et al., 1978), it is possible to construct stationary matter configurations contained within the equipotential surfaces, that is surfaces of constant pressure. One of the most interesting features of these matter configurations is that under certain condition self-crossing (sometimes referred to as Roche-lobe) equipotential surfaces exist. In other words, there are equipotential surfaces that present a sharp cusp on the equatorial plane. Thus, it is possible to construct models of accretion tori that fill this self-crossing surface and which present a cusp at the inner edge. The presence of the cusp has important implications as it behaves as an effective Langrangian point so that accretion of matter onto the black hole can take place through this point even in the case that there is no shear viscosity in the fluid. Another interesting aspect of tori with a cusp is that accretion process may diverge leading to a runaway accretion process know as the runaway instability, which can destroy the disc on a dynamical time scale.

Although the initial intention to investigate this dynamical instability through 3D simulations we have started our investigation by considering non-selfgravitating and non-accreting matter configurations. These are matter configurations filling a equipotential surface which is within the Roche-lobe and therefore, non accretion can take place. There are at least, two reasons that justify this choice. First of all, the numerical evolution of stable tori will help to assess whether it is possible to perform accurate and stable simulations in 3D of the runaway instability with the presently available computational resources. Although the `Whisky` code takes advantage of the parallelization provided through the `Cactus computational tool`, 3D simulations are computationally very demanding, particularly, when using uniform Cartesian grids. The approach followed by Font & Daigne (2002a,b); Daigne & Font (2004); Zanotti et al. (2003) and Zanotti et al. (2004) allows for much higher resolutions at the inner edge of the disc than those that can be achieved in 3D with uniform Cartesian grids (unless one uses techniques such as fixed mesh refinement and adaptive mesh refinement) so it is not certain a priory that the code can accurately handle this type of investigations.

Here we will briefly review the construction of the stationary configurations of tori in a Schwarzschild spacetime although, we will use an axisymmetric spacetime in order to derive more general expressions. We first assume that the external gravitational field is stationary and axisymmetric. That is, the metric does not depend on the time coordinate or on the azimuthal coordinate ϕ and can be written in spherical coordinates (t,r,θ,ϕ) as follows

$$ds^2 = g_{tt}dt^2 + 2g_{t\phi}dtd\phi + g_{\phi\phi}d\phi^2 + g_{rr}dr^2 + g_{\theta\theta}d\theta^2. \tag{3.100}$$

We consider a perfect fluid so that the stress-energy tensor is given by

$$T_{\mu\nu} = \rho h u_\mu u_\nu + P g_{\mu\nu}, \tag{3.101}$$

where **u** is the four-velocity of the fluid, ρ the rest-mass density, h the enthalpy and $g_{\mu\nu}$ the spacetime metric which in this case is the Schwarzschild metric. We will describe the fluid as an ideal fluid with a polytropic equations of state, $P = k\rho^\Gamma$, where k is the polytropic constant and Γ the adiabatic index. The fluid is assumed to rotate around the central black hole in circular motion with four-velocity $u^\mu = (u^t, 0, 0, u^\phi)$. We can define the coordinate angular velocity observed from infinity as $\Omega(r, \theta) \equiv u^\phi/u^t$ and the specific angular momentum as $\ell \equiv -u_\phi/u_t$.

It is easy to show that the specific angular momentum and the angular velocity are related in terms of the metric functions through the following expressions

$$\ell = -\frac{\Omega g_{\phi\phi} + g_{t\phi}}{\Omega g_{t\phi} + g_{tt}}, \tag{3.102}$$

$$\Omega = -\frac{\ell g_{tt} + g_{t\phi}}{\ell g_{t\phi} + g_{\phi\phi}}, \tag{3.103}$$

after imposing stationary and axisymmetry for the hydrodynamic equations, these can be written as a simple hydrostatic equilibrium equations of the type

$$\frac{\nabla_i P}{P + \epsilon} = -\nabla_i \ln u_t - \frac{\Omega \nabla_i \ell}{1 - \Omega \ell}. \tag{3.104}$$

Note that the equation of motion simplifies considerably for the case of tori with a constant distribution of specific angular momentum as the second term in the right-hand-side of 3.104 vanish. In order to construct the initial model we first choose a distribution of specific angular momentum which determines the positions of the cusp and the centre of the torus, since at these positions the specific angular momentum must be that of a Keplerian geodesic circular orbit. For a constant distribution of specific angular momentum, its value has to be within the values of the specific angular momentum of the marginally bound and marginally stable orbits as this condition guarantees that the closed equipotential surface has a finite sizes and a cusp (see Section 2.4). Next, the inner edge of the torus $r_{\rm in}$ is determined by fixing the potential gap, $\Delta W_{in} = W_{\rm in} - W_{\rm cusp}$, which for a generic distribution of specific angular momentum, ℓ, is defined as

$$\Delta W_{\rm in} = \ln[(-u_t)_{\rm in}] - \ln[(-u_t)_{\rm cusp}] - \int_{\ell_{\rm cusp}}^{\ell_{\rm in}} \frac{\Omega d\ell}{1 - \Omega \ell}\ . \tag{3.105}$$

A torus with $\Delta W_{\rm in} = 0$ will fill its Roche-lobe so that its inner edge coincides with the position of the cusp, while if $\Delta W_{\rm in} < 0$ the torus will be contained within the Roche-lobe. Once the inner edge of the torus is fixed, we obtain the position of the outer edge by enforcing that both edges belong to the same equipotential surface. Finally, we compute the hydrodynamical variables from the equation of state and the relativistic Euler equation.

3.11.1 Numerical Results

As a first and, indeed, last attempt to study this problem in 3D we have investigated the dynamical evolution of a stable torus (*i.e.* $\Delta W_{\rm in} < 0$) orbiting around a Schwarzschild black hole in a fixed spacetime. We have used a polytropic equation of state with polytropic constant $k = 1.21 \times 10^{14}(cgs)$ and adiabatic index $\gamma = 3/4$. The self-gravity of the torus is neglected and the spacetime metric is that of a Schwarzschild black hole of $M_{bh} = 2.5 M_{\odot}$. We have constructed a torus with constant distribution of specific angular momentum ($\ell/M_{bh} = 3.8$) and density maximum $\rho_{max} = 5.73 \times 10^{14}(cgs)$. This model has a cusp at $r_{cusp} = 4.576 r_g$ and the density maximum located at $r_{max} = 8.352 r_g$, where r_g is the gravitational radius. In the vacuum regions we introduce a sufficiently low atmosphere that will not affect the dynamical evolution of the bulk matter (Font et al., 2002c) . For this atmosphere, we use the Michel solution (Michel 1972; Font & Ibáñez 1998a,b) of a spherical accreting flow onto a Schwarzschild black hole such that the maximum density of this background spherical solution is approximately 1.0×10^{-7} the maximum density of the torus. At the outer boundaries of the computational domain we impose flat boundary conditions which keep the hydrodynamical variables at the boundary points fixed to the initial value given by the Michel solution. We have used the Marquina's flux formula for the evaluation of the intercell fluxes and PPM reconstruction.

The upper panel in Fig. 3.6 shows the time evolution of the density maximum of the torus. Since the initial model is stable and no accretion through the cusp is possible unless the model is perturbed from its equilibrium, we expect that actually no 'evolution' occurs, or in other words, that the density maximum remains close to the initial value during the numerical evolution. However, this figure shows a significant decrease in the the density maximum. The three different lines refer to the same initial data evolved with three different resolutions using 32^3, 64^3 and 96^3 grid points. Although the numerical error and therefore the mass loss reduced by increasing the resolution, the numerical solution is far from being accurate. For instance, the density maximum decreased about 50% in the highest resolution run in only a few dynamical timescales (where the dynamical timescale is taken to be that of the orbital period at the centre of the torus, $t_{orb} = 1.86$ ms; note

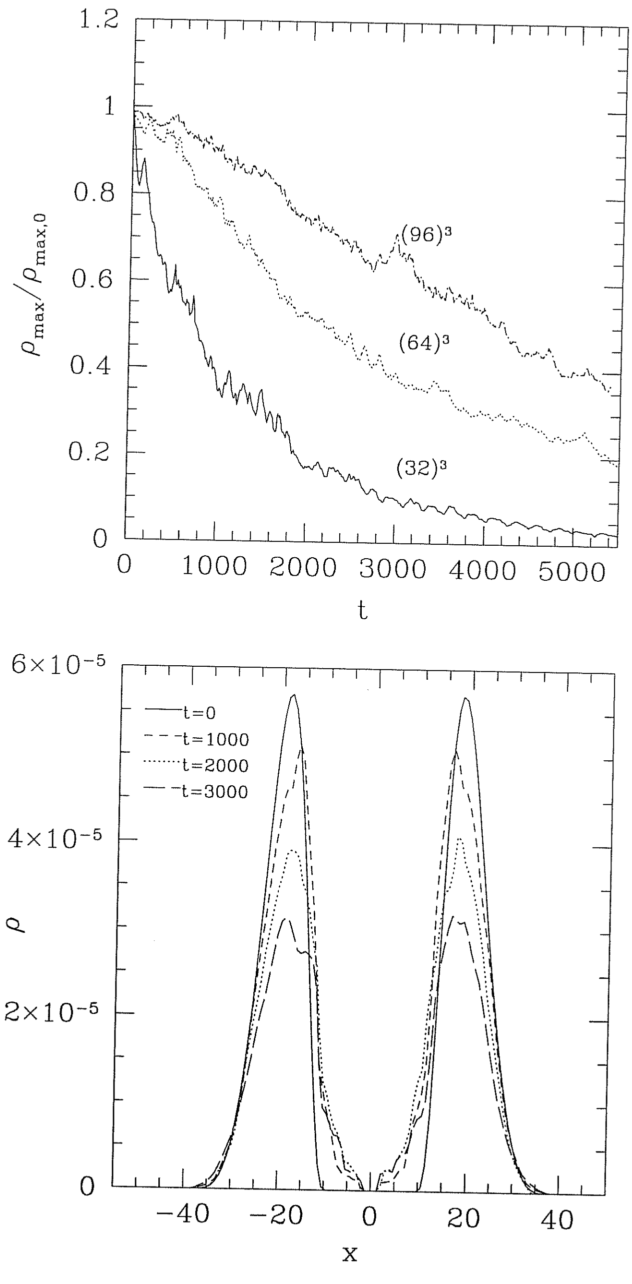

Figure 3.6: Left panel shows the time evolutions of the density maximum of a stable torus corresponding to simulations with 32^3, 64^3 and 96^3 grid points while the right panel shows the rest-mass density profile along the x-axis at four different times during the evolution performed with a 96^3 grid points.

that in $c = G = M_\odot = 1$ units, $t = 1000 \approx 5$ ms). We note that Font & Daigne (2002a,b) and Zanotti et al. (2003) were able to carry out long-term stable numerical simulations of analogous initial models using as well the HRSC schemes but with a 2D code which allowed for much higher resolutions. The lower panel of Fig. 3.6 shows the rest-mass density profile along the x-axis at the initial time and three later times of the highest resolution simulation with 96^3 grid points. Again, this figure clearly shows that the solution degrades significantly in time on the whole.

We performed simulations using all approximate Riemann solvers and reconstruction schemes available in the `Whisky` code but the results were not improved. We believe this inaccurate simulations are the result uniquely of a lack of spatial resolution. While higher resolution with more than 100^3 grid points can be used, would be computationally extremely expensive and certainly it would not allow for a systematic study of the dynamics of self-gravitating tori, in general, and of the runaway instability in particular. Because of this, we have not carried out further investigations on the dynamics of tori with `Whisky` and rather start in 2003 developing from scratch the new 2D `Nada` code for solving in 2-dimensions the coupled system of equation consisting of Einstein equations and general relativistic hydrodynamic equations in Cartesian coordinates.

Chapter 4

A New 2D-Axisymmetric Fully Relativistic Code: the "Nada" Code

4.1 Introduction

Interested to investigate the dynamics of self-gravitating tori and the runaway instability of accreting tori, we have developed a new two dimensional (2D), fully relativistic and non-vacuum code, the `Nada` code, for the study of axisymmetric systems. The `Nada` code implements high resolution shock capturing (HRSC) methods and the Einstein equations are cast into a system of constraint and evolution equations resulting from the 3+1 decomposition of this system of equations. Since this system of equations has been discussed in Chapter 3, in the following Sections we make a general description of the `Nada` code postponing the discussion of the results obtained with our code to the following Chapter. Particular attention in this Chapter is given to the method we use to impose the condition of axisymmetry when expressing equations in Cartesian coordinates, to the boundary and gauge conditions chosen, to the explicit form of the relativistic hydrodynamic equations used in the code and to the scheme for integrating forward in time the system of the Einstein and the hydrodynamic equations.

4.2 Discretization of Axisymmetric Systems: "Cartoon" Method

Axisymmetric systems pose well known difficulties for stable numerical simulations when they are expressed in coordinates adapted to the symmetry (*i.e.* cylindrical (ρ,z,ϕ) and spherical polar (r,θ,ϕ) coordinates) due to coordinate singularities on the symmetry axis. The advantage of using these types of coordinates systems is that they fully exploit the intrinsic symmetries of the system (*cf.* Brandt et al., 2000 for hydrodynamic evolutions in dynamical axisymmetric black hole spacetimes) and reduce considerably the computational cost. An alternative is to use three dimensional Cartesian coordinates where all terms are regular and, as a result, do not present these types of pathology. On the other hand, three dimensional Cartesian coordinates require larger computational resources and are less adapted to the astrophysical problems. In order to combine the best of both options, Alcubierre et al. (2001a) proposed a method, referred as *Cartoon* method (Alcubierre et al., 2001a; Shibata 2000; Frauendiener 2002; Shibata 2003a,b) , which takes advantage of the regular nature of 3D Cartesian coordinates and where an equivalent 2D problem is solved instead of the full 3D one.

The basic idea behind the cartoon method is that given any system of equations in 3D and possesing a rotation symmetry with respect to the z-axis it can be finite differenced and solved for instance, in the x,z ($y = 0$) plane alone because of the condition of symmetry with respect to rotations about the z-axis. When the system of equations is expressed in Cartesian coordinates, partial derivative terms with respect to the y-coordinate will appear and these need to be computed using the computational domain. For instance, in a second order centred difference approximation, the values of the derivative in the y-direction of a quantity $u(x, 0, z)$, are computed using the values of u at the nearest two grid points *i.e.* $u(x, -\Delta y, z)$,$u(x, \Delta y, z)$. It should be noticed that because of the axisymmetry, the y derivatives of all quantities can be determined in the x-z plane from information contained in this same plane, in other words, the solution in the x-z plane can be rotated to any y value according to tensor transformations laws.

The cartoon method obtains the boundary conditions at $y = \pm\Delta y$ that are neces-

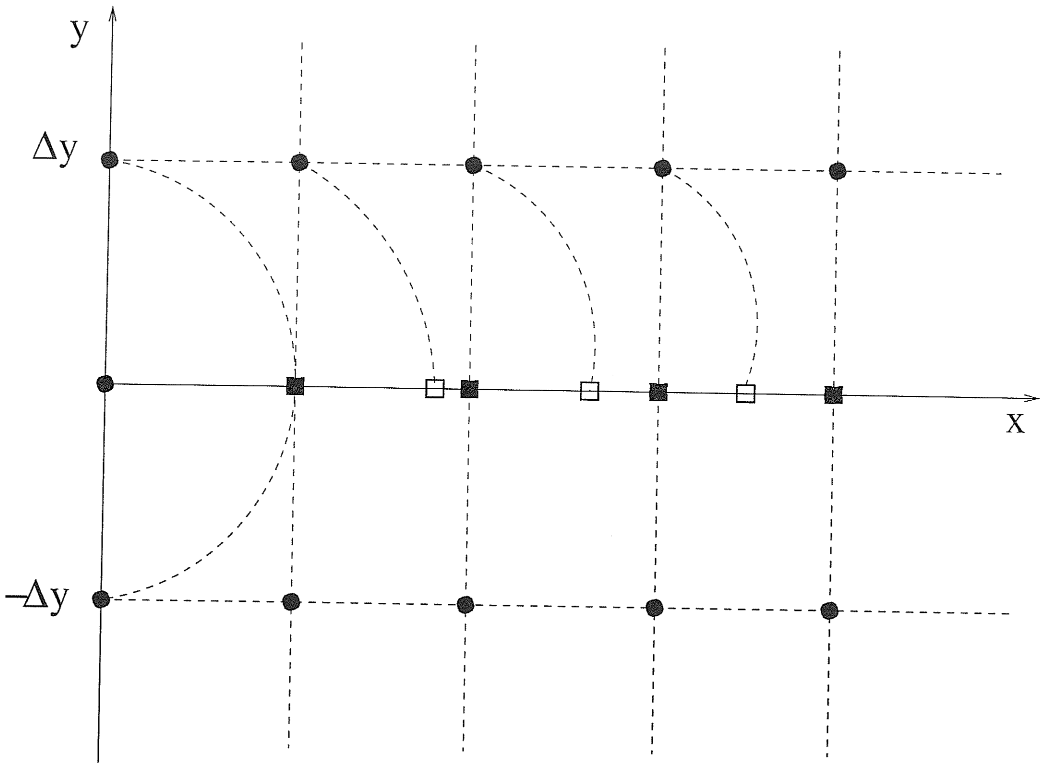

Figure 4.1: Illustration of cartoon method. Black squares indicate grid points along the x-axis. Solid cicles indicate boundary points and squares indicate points where the grid functions are interpolated.

sary to evaluate the derivatives in the y direction by means of a rotation about the symmetry axis of the different tensor quantities. In Fig.4.1 we illustrate how to find the value of grid functions at $y = \Delta y$ by a rotation through an angle $\phi_0(x) = \arccos(x/\sqrt{x^2 + \Delta y^2})$. It shows the view of the x-y ($z = 0$) plane where black squares show the grid points along the x-axis and solid circles refer to points outside the grid at $y = \pm\Delta y$ and at the origing. The value of the grid functions at $y = \pm\Delta y$ can be computed from the invariance condition under rotations about the z-axis. The transformation for a scalar field, T, and a tensor field, T^{ij}, used to compute their values at $y = \Delta y$ are given by the following expressions

$$T(x, \Delta y, z) = T(\sqrt{x^2 + \Delta y^2}, 0, z), \tag{4.1}$$

$$T^{ij}(x, \Delta y, z) = \Lambda^i_m \Lambda^j_n T^{mn}(\sqrt{x^2 + \Delta y^2}, 0, z), \tag{4.2}$$

where the rotation matrix, Λ^i_j, is given by

$$\Lambda^i_j = \begin{pmatrix} \dfrac{x}{\sqrt{x^2 + \Delta y^2}} & \dfrac{-\Delta y}{\sqrt{x^2 + \Delta y^2}} & 0 \\ \dfrac{\Delta y}{\sqrt{x^2 + \Delta y^2}} & \dfrac{x}{\sqrt{x^2 + \Delta y^2}} & 0 \\ 0 & 0 & 1 \end{pmatrix}. \tag{4.3}$$

The values of variables at the position $(\sqrt{x^2 + \Delta y^2}, 0, z)$, (points illustrated with a transparent square in Fig.4.1) must be interpolated from the neighboring grid points. We obtain the values of variables at $(\sqrt{x^2 + \Delta y^2}, 0, z)$ by using second-order parabolic interpolation from the nearby grid points along the x-direction (i.e. $x - \Delta x, x, x + \Delta x$) while at the outer boundary, $x = L$, we use only two points for extrapolation (Shibata 2003a).

4.3 Boundary conditions

As customary when solving PDEs with finite difference codes, boundary conditions need to be specified at the boundary of the computational domain at each time step during the evolution. Imposing the appropriate boundary conditions is an important ingredient to achieve stable numerical simulations although so far there is not an ultimate prescription for specifying fully consistent boundary conditions for the type of formulation which we are using. We have implemented a number of different boundary conditions that can be imposed for the spacetime variables or the hydrodynamical variables at the inner and outer boundaries depending on the physical problem under study. We have in general the computational domain as $0 \leq x \leq L$ and $0 \leq z \leq L$, where L refers to the location of the outer boundaries. These conditions can be summarize as follows:

π-Rotation symmetry: We have assumed π-rotation symmetry around the z-axis for both the spacetime and hydrodynamical variables. We impose the boundary condition as

$$Q(x,0,z) = Q(-x,0,z), \tag{4.4}$$

$$Q_A(x,0,z) = -Q_A(-x,0,z), \tag{4.5}$$

$$Q^A(x,0,z) = -Q^A(-x,0,z), \tag{4.6}$$

$$Q_z(x,0,z) = -Q_z(-x,0,z), \tag{4.7}$$

$$Q^z(x,0,z) = -Q^z(-x,0,z), \tag{4.8}$$

$$Q_{AB}(x,0,z) = Q_{AB}(-x,0,z), \tag{4.9}$$

$$Q_{Az}(x,0,z) = -Q_{Az}(-x,0,z), \tag{4.10}$$

$$Q_{zz}(x,0,z) = Q_{zz}(-x,0,z), \tag{4.11}$$

where A and $B = x$ or y, and Q, $Q^i(Q_i)$, Q_{ij} denote arbitrary scalar, vector and tensor quantities, respectively.

Equatorial plane symmetry: Symmetry is also assumed with respect to the $z = 0$ plane for both the spacetime and hydrodynamical variables

$$Q(x,0,z) = Q(x,0,-z), \tag{4.12}$$

$$Q_A(x,0,z) = -Q_A(x,0,-z), \tag{4.13}$$

$$Q^A(x,0,z) = -Q^A(x,0,-z), \tag{4.14}$$

$$Q_z(x,0,z) = -Q_z(x,0,-z), \tag{4.15}$$

$$Q^z(x,0,z) = -Q^z(x,0,-z), \tag{4.16}$$

$$Q_{AB}(x,0,z) = Q_{AB}(x,0,-z), \tag{4.17}$$

$$Q_{Az}(x,0,z) = -Q_{Az}(x,0,-z), \tag{4.18}$$

$$Q_{zz}(x,0,z) = Q_{zz}(x,0,-z), \tag{4.19}$$

Static: The variables are kept fixed at the outer boundaries. We have mainly used static boundary condition for the hydrodynamical variables.

Radiative: At the outer boundaries we have imposed radiative boundary conditions applied to the difference between a given spacetime variable, u and its asymptotic value, u_0 (typically 1 for the lapse and diagonal metric components, and zero for everything else). Note that we do not apply this boundary condition to the conformal connection functions, $\tilde{\Gamma}^i$, for which we used static boundary conditions (Alcubierre et al. 2003a; Yo et al. 2002). In our code the radiative boundary condition is expressed as

$$\frac{x_i}{r}\partial_t u + \partial_i u + \frac{x_i}{r^2}\left(u - u_0\right) = 0, \tag{4.20}$$

where $r^2 = x^2 + z^2$ and $x_i = x, z$.

4.4 Gauge Conditions

In addition to the spacetime variables $(\tilde{\gamma}_{ij}, \tilde{A}_{ij}, K, \phi, \tilde{\Gamma}^i)$, there are two more variables left undetermined, the lapse, α and the shift vector, β^i, which reflect the coordinate freedom in general relativity. Thus, in the 3+1 formalism, this gauge freedom allows the possibility of choosing different time slicings and spatial coordinates on each slice. Choosing the appropriate gauge is one of the key issues for successful simulations in numerical relativity. The `Nada` code is designed to handle arbitrary lapse and shift conditions, which can be chosen according to each numerical simulation. We list below the gauge conditions available in the code.

A. Slicing conditions

Although in some numerical evolutions the simplest slicing would be to hold fixed in time the value of the lapse function, it turns out that it is difficult to keep the evolution stable if the lapse is not allowed to adapt to the other evolved spacetime variables, in particular to the trace of the extrinsic curvature, K. We have used the so called *hyperbolic K-driver slicing conditions* (Bona et al. 1995, Alcubierre et al. 2000a, 2001) given by

$$\partial_t \alpha = -f(\alpha)\alpha^2 \left(K - K_0\right) + \beta^i \partial_i \alpha, \tag{4.21}$$

where $K_0 = K(t = 0)$ and $f(\alpha) > 0$. The *"Harmonic"* slicing condition is recovered by setting $f = 1$, while by setting $f = q/\alpha$, with q an integer we recover the *"1+log"* slicing condition, where we usually set $q = 2$. These types of algebraic slicing are now widely used in numerical relativity because of their stability properties and because they are computationally more efficient than "maximal" slicing, since one solves an evolution equation for the lapse instead of an elliptic equation.

B. Shift conditions

For the spatial gauge, we normally use either the analytic prescription for the shift or the so called *"Gamma-driver"* condition that evolves the shift in such a way that the conformal connection functions (Alcubierre et al., 2000, 2003a; Alcubierre & Brügmann 2001) are kept constant. We have implemented this condition in the following form

$$\partial_t \beta^i = \lambda \partial_t \tilde{\Gamma}^i, \tag{4.22}$$

where we choose $\lambda = 0.05$. Yo et al. (2002) have shown that this shift condition leads to long-term stable evolutions of single black holes in Kerr-Schild coordinates.

4.5 Formulation of the Hydrodynamic Equations in Axisymmetry

First, the general relativistic hydrodynamic equations are written in a conservative form in cylindrical coordinates following Shibata (2003a). However, since we solve the Einstein equations in the $y = 0$ with Cartesian coordinates, we then rewrite the hydrodynamic equations in the Cartesian coordinates for $y = 0$. The explicit form of the hydrodynamic equations used in the `Nada` code is as follows (Shibata 2003; we recall that the field variables are $\phi, \tilde{\gamma}_{ij}, \tilde{A}_{ij}, K, \beta_i$ and α)

$$\partial_t \rho_* + \partial_x(\rho_* v^x) + \partial_z(\rho_* v^z) = -\frac{\rho_* v^x}{x}, \tag{4.23}$$

$$\begin{aligned}
&\partial_t(\rho_* \hat{\mathrm{u}}_x) + \partial_x \left[\rho_* \hat{\mathrm{u}}_x v^x + P\alpha e^{6\phi}\right] + \partial_z \left[\rho_* \hat{\mathrm{u}}_x v^z\right] \\
&\quad = -\frac{\rho_* \hat{\mathrm{u}}_x v^x}{x} + \frac{\rho_* \hat{\mathrm{u}}_y v^y}{x} + P\partial_x(\alpha e^{6\phi}) \\
&\quad -\rho_* \left[Wh\partial_x\alpha - \hat{\mathrm{u}}_j \partial_x \beta^j + \frac{\alpha e^{-4\phi}\hat{\mathrm{u}}_i \hat{\mathrm{u}}_j}{2Wh}\partial_x \tilde{\gamma}^{ij} - \frac{2\alpha h(W^2-1)}{W}\partial_x\phi\right],
\end{aligned} \tag{4.24}$$

$$\partial_t(\rho_* \hat{\mathrm{u}}_y) + \partial_x(\rho_* \hat{\mathrm{u}}_y v^x) + \partial_z(\rho_* \hat{\mathrm{u}}_y v^z) = -2\frac{\rho_* \hat{\mathrm{u}}_y v^x}{x} \tag{4.25}$$

$$\begin{aligned}
&\partial_t(\rho_* \hat{\mathrm{u}}_z) + \partial_x \left[\rho_* \hat{\mathrm{u}}_z v^x\right] + \partial_z \left[\rho_* \hat{\mathrm{u}}_z v^z + P\alpha e^{6\phi}\right] \\
&\quad = -\frac{\rho_* \hat{\mathrm{u}}_z v^x}{x} + P\partial_z(\alpha e^{6\phi}) \\
&\quad -\rho_* \left[Wh\partial_z\alpha - \hat{\mathrm{u}}_j \partial_z \beta^j + \frac{\alpha e^{-4\phi}\hat{\mathrm{u}}_i \hat{\mathrm{u}}_j}{2Wh}\partial_z \tilde{\gamma}^{ij} - \frac{2\alpha h(W^2-1)}{W}\partial_z\phi\right],
\end{aligned} \tag{4.26}$$

$$\begin{aligned}
&\partial_t(\rho_* \hat{\mathrm{e}}) + \partial_x \left[\rho_* \hat{\mathrm{e}} v^x + P e^{6\phi}(v^x + \beta^x)\right] + \partial_z \left[\rho_* \hat{\mathrm{e}} v^z + P e^{6\phi}(v^z + \beta^z)\right] \\
&\quad = -\frac{\rho_* \hat{\mathrm{e}} v^x + P e^{6\phi}(v^x + \beta^x)}{x} + \alpha e^{6\phi} P K + \frac{\rho_*}{u^t}\hat{\mathrm{u}}_i \hat{\mathrm{u}}_j K^{ij} - \rho_* \hat{\mathrm{u}}_i \gamma^{ij} D_j \alpha,
\end{aligned} \tag{4.27}$$

where we have used the following definitions

$$\rho_* \equiv \rho W e^{6\phi}, \tag{4.28}$$

$$v^i \equiv \frac{u^i}{u^t} = -\beta^i + \alpha\gamma^{ij}\frac{\hat{\mathrm{u}}_j}{hW}, \tag{4.29}$$

$$\hat{\mathrm{u}}_i \equiv hu_i, \tag{4.30}$$

$$\hat{\mathrm{e}} \equiv \frac{e^{6\phi}}{\rho_*}T_{\mu\nu}n^\mu n^\nu = hW - \frac{P}{\rho W}, \tag{4.31}$$

$$W \equiv \alpha u^t. \tag{4.32}$$

Equations (4.23)-(4.27) can be written in a conservation form as

$$\partial_t \mathbf{U} + \partial_x \mathbf{F}^x + \partial_z \mathbf{F}^z = \mathbf{S}, \tag{4.33}$$

where $\mathbf{S}$ is the vector of sources given by the right-hand-sides of Eqs. (4.23)-(4.27). The unknowns, $\mathbf{U}$, and fluxes $\mathbf{F}^x$ and $\mathbf{F}^z$ are defined as

$$\mathbf{U} = (\rho_*, J_x, J_y, J_z, E_*), \tag{4.34}$$

$$\mathbf{F}^x = [\rho_* v^x, J_x v^x + P\alpha\sqrt{\gamma}, J_y v^x, J_z v^x, E_* v^x + P\alpha\sqrt{\gamma}(v^x + \beta^x)], \tag{4.35}$$

$$\mathbf{F}^z = [\rho_* v^z, J_x v^z, J_y v^z, J_z v^z + P\alpha\sqrt{\gamma}, E_* v^z + P\alpha\sqrt{\gamma}(v^z + \beta^z)], \tag{4.36}$$

where $J_i \equiv \rho_* \hat{\mathrm{u}}_i$ and $E_* \equiv \rho_* \hat{\mathrm{e}}$.

Spectral decomposition

The Jacobian matrix in the x-direction $M^x_{ab} = \partial F^x_a / \partial U_b$ for $a, b = (1, ..., 5)$ for this set of equations has the following set of eigenvalues corresponding to the characteristic speeds in the x-direction

$$\begin{aligned}\lambda^x_\pm = \frac{1}{\alpha^2 - V_k V^k c_s^2} \Big[v^x \alpha^2 (1 - c_s^2) - \beta^x c_s^2 (\alpha^2 - V_k V^k) \\ \pm \alpha c_s \sqrt{(\alpha^2 - V_k V^k)\left\{\gamma^{xx}(\alpha^2 - V_k V^k c_s^2) - (1 - c_s^2) V^x V^x\right\}} \Big],\end{aligned} \tag{4.37}$$

$$\lambda^x = v^x \ \ \text{(triple root)} \tag{4.38}$$

where

$$c_s^2 = \frac{1}{h}\left(\chi + \frac{P}{\rho}\kappa\right), \tag{4.39}$$

$$V^k = \gamma^{kl}V_l = v^k + \beta^k, \tag{4.40}$$

$$\chi = \left.\frac{\partial P}{\partial \rho}\right|_{\epsilon}, \tag{4.41}$$

$$\kappa = \frac{1}{\rho}\left.\frac{\partial P}{\partial \epsilon}\right|_{\rho}. \tag{4.42}$$

Next, the set of right eigenvectors such that

$$M^x_{ad} = K^x_{ab}\Lambda^x_{bc}(K^x_{cd})^{-1}, \tag{4.43}$$

can be expressed as

$$K^x_{ab} = C_{ac}T^x_{cb}, \tag{4.44}$$

where

$$T^x_{ab} = \begin{bmatrix} 1 & -\kappa & 0 & 0 & 1 \\ H^{xx}(\lambda^x_+) & 0 & 0 & 0 & H^{xx}(\lambda^x_-) \\ H^{xy}(\lambda^x_+) & 0 & \rho^{-1} & 0 & H^{xy}(\lambda^x_-) \\ H^{xz}(\lambda^x_+) & 0 & 0 & \rho^{-1} & H^{xz}(\lambda^x_-) \\ P/\rho^2 & 0 & 0 & \chi/\rho & P/\rho^2 \end{bmatrix}, \tag{4.45}$$

$$C_{ab} = \begin{bmatrix} W & \rho W^3V_x/\alpha^2 & \rho W^3V_y/\alpha^2 & \rho W^3V_z/\alpha^2 & 0 \\ h_1W^2V_x/\alpha & \rho hW^2F_{xx}/\alpha & \rho hW^2F_{xy}/\alpha & \rho hW^2F_{xz}/\alpha & \rho h_2W^2V_x/\alpha \\ h_1W^2V_y/\alpha & \rho hW^2F_{xy}/\alpha & \rho hW^2F_{yy}/\alpha & \rho hW^2F_{yz}/\alpha & \rho h_2W^2V_y/\alpha \\ h_1W^2V_z/\alpha & \rho hW^2F_{xz}/\alpha & \rho hW^2F_{yz}/\alpha & \rho hW^2F_{zz}/\alpha & \rho h_2W^2V_z/\alpha \\ h_1W^2 - \chi & 2\rho hW^4V_x/\alpha^2 & 2\rho hW^4V_y/\alpha^2 & 2\rho hW^4V_z/\alpha^2 & \rho h_2W^2 - \rho\kappa \end{bmatrix}, \tag{4.46}$$

and

$$F_{ij} = \gamma_{ij} + \frac{2W^2V_iV_j}{\alpha^2}, \tag{4.47}$$

$$h_1 = 1 + \epsilon + \chi, \tag{4.48}$$

$$h_2 = 1 + \kappa, \tag{4.49}$$

$$H^{xi}(\lambda) = \frac{-c_s^2(v^x - \lambda)\left\{\alpha^2\gamma^{xi} - V^i(\beta^x + \lambda)\right\}}{\rho W^2(v^x - \lambda)^2}. \tag{4.50}$$

4.6 Time Integration and Coupling to the Einstein Equations

The method which we have adopted for the time integration, the so called *method of lines* (Thornburg 1993; Teukolsky 2000; Frauendiener 2002), is applied to the hydrodynamic equations and the Einstein equations. A important advantage of the method of lines approach is that provides a neat way of coupling the spacetime and hydrodynamical variables and allows for a straightforward implementation of different evolution schemes. Essentially, the method of lines transforms the solution of a system of PDEs into the solution of a system of ordinary differential equations (ODEs) by discretizing only in space and retaining the continuous time derivatives, yielding a set of ODEs for the time dependence of the field variables at the spatial grid points. This set of equations can then be solved numerically by any stable ODE solver.

That is, the method of lines discretizes first only in space so that the PDEs can be approximated to ODEs in time. For instance, the one-dimensional system of conservation laws (3.71) is written as a system of ODEs as follows

$$\frac{d}{dt}\mathbf{U}_i = \frac{1}{\Delta x}(\mathbf{f}_{i-\frac{1}{2}} - \mathbf{f}_{i+\frac{1}{2}}) + \mathbf{S}_i. \tag{4.51}$$

The computational domain is a 2-dimensional grid (Fig. 4.2), so it is convenient to identify every grid point by two indices determining its location in the grid. According to the above discretization (4.51), it follows that the system of equations (4.33) can be approximated at every mesh point of the 2-dimensional computational grid by the following system of ODEs

$$\frac{d}{dt}\mathbf{U}_{i,k} = \frac{1}{\Delta x}(\mathbf{f}^x_{i-\frac{1}{2},k} - \mathbf{f}^x_{i+\frac{1}{2},k}) + \frac{1}{\Delta z}(\mathbf{f}^z_{i,k-\frac{1}{2}} - \mathbf{f}^z_{i,k+\frac{1}{2}}) + \mathbf{S}_{i,k}. \tag{4.52}$$

There are two schemes implemented for the update of the numerical solution with time: an iterative Crank-Nicholson (ICN) scheme (Teukolsky 2000, Alcubierre et al., 2000a) and a third-order Runge-Kutta (RK) algorithm. The ICN scheme was proposed in order to take advantage of the good stability properties of the implicit Crank-Nicholson scheme by turning this later implicit scheme into an explicit one. The ICN scheme has become very popular in numerical relativity in recent years for the good stability properties in

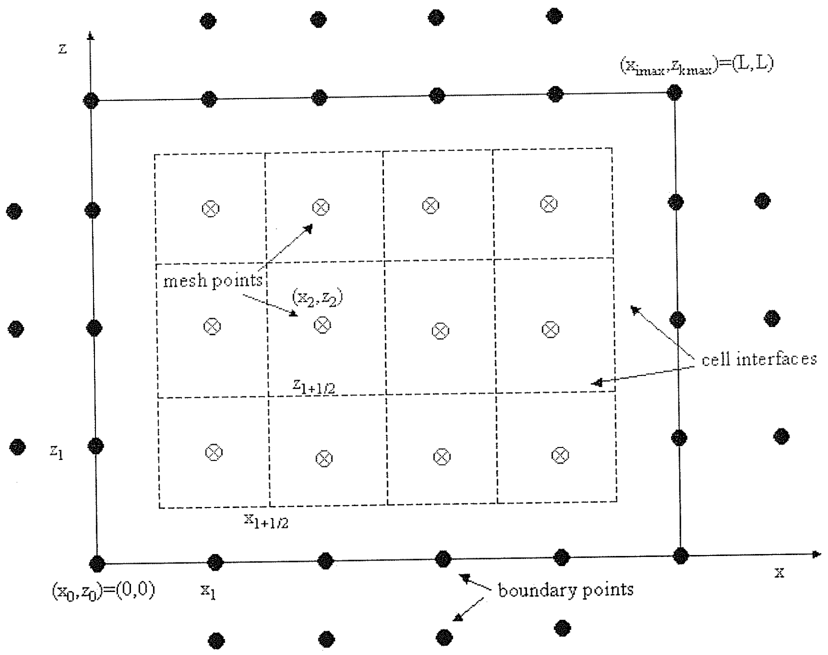

Figure 4.2: Schematic representation of the 2-dimensional grid used with the `Nada` code. Solid circles indicate boundary points. These points are not updated using the evolution equations but according to the specific boundary condition that we impose. Crossed circles refer to grid points at which the variables are evolved.

solving Einstein's equations. We have implement the ICN scheme taking two corrector steps, which are enough to achieve a (conditionally) stable second-order accurate scheme. The ICN method is implemented in the `Nada` code for the solution of the Einstein equations and also the general relativistic hydrodynamic equations. On the other hand, the third-order Runge-kutta algorithm, also known for its good stability properties, has only been implemented in our code for the solution of the hydrodynamic equations so far.

We use the second order MC reconstruction scheme to obtain the left and right states of the primitive variables (i.e. $\rho, v^x, v^y, v^z, \epsilon$) at each cell interface and these reconstructed variables are then used to compute the left and right states of the evolved quantities ($\rho_*, J_x, J_y, J_z, E_*$). Next, we use the Roe approximate Riemann solver to compute the numerical fluxes in the x and z directions.

The derivative terms in the spacetime evolution equations are represented by a second order centred finite difference approximation in a uniform Cartesian grid except for the advection terms (terms formally like $\beta^i \partial_i u$), for which we use a second order upwind scheme (Kelly et al. 2001) of the form

$$\partial_x u \approx \frac{(u_{i+1} - u_{i-1})}{2\Delta x} \pm \frac{(u_{i\mp 1} - 3u_i + u_{i\pm 1} - u_{i\pm 2})}{6\Delta x}, \tag{4.53}$$

where the choice of sign is given by $\pm = sign(\beta^i)$.

4.6.1 Recovering of the Primitive variables

After each iteration of the ODE solver the conserved variables are updated and we then need to find the primitive hydrodynamical variables at the corresponding step. We use either a bisection method or a Newton-Raphson method (Press 1986) to solve the simple equations that calculate the primitive quantities (i.e. $\rho, v^x, v^y, v^z, \epsilon$) in terms of the conserved ones ($\rho_*, J_x, J_y, J_z, E_*$).

The primitives quantities are computed by solving the following equation for the Lorentz factor, W, derived from the normalization of the 4-velocity of the fluid (Shibata 2003a)

$$W^2 = 1 + \gamma^{ij} u_i u_j = 1 + \gamma^{ij} \hat{\mathrm{u}}_i \hat{\mathrm{u}}_j \left(\frac{\hat{\mathrm{e}}}{W} + \frac{P}{\rho W^2} \right)^{-2}. \tag{4.54}$$

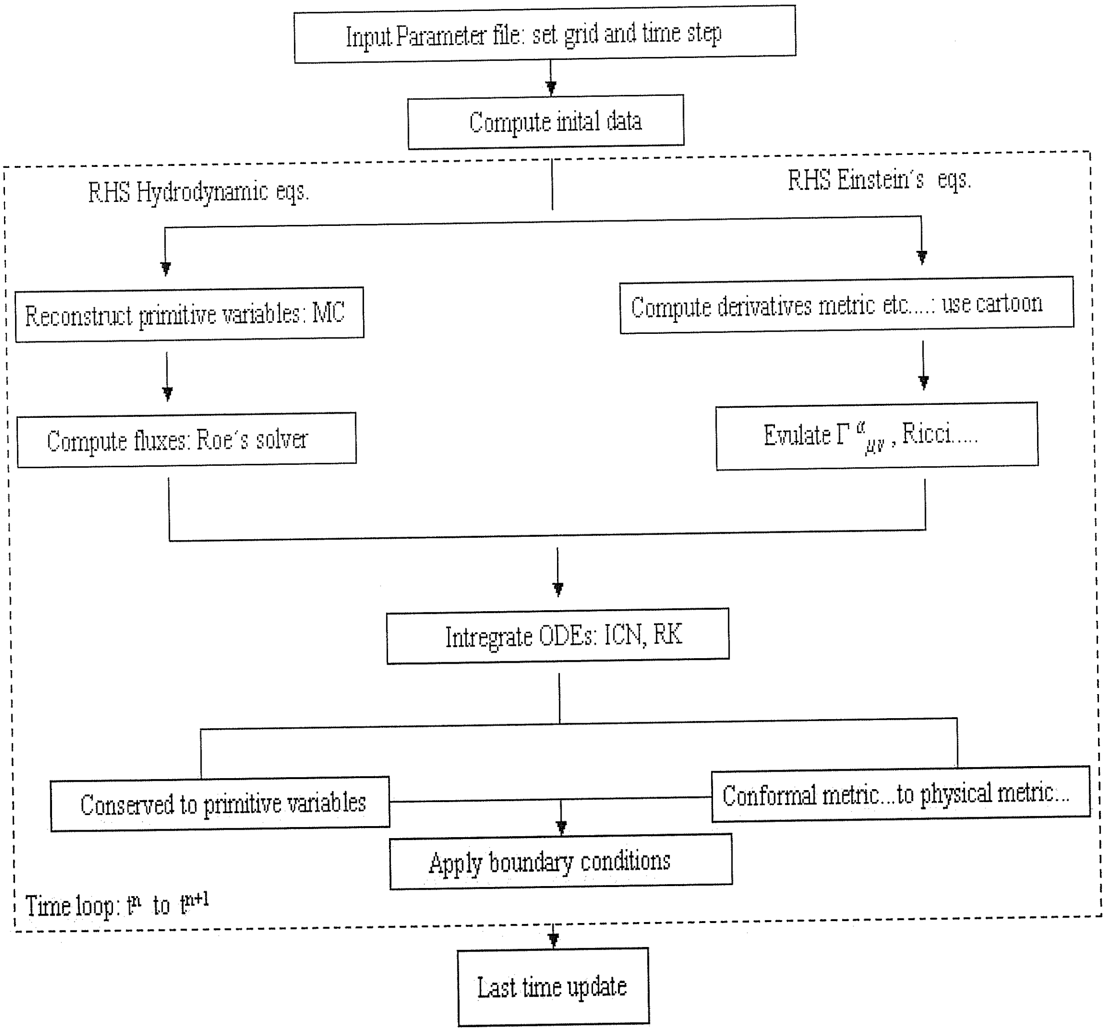

Figure 4.3: Flow chart of the `Nada` code in which the general relativistic hydrodynamic equations and Einstein equations are solved using the method of lines.

Once we solve for W we compute the updated ρ, v^i, P, ϵ and h from Eqs. (4.28)-(4.32) and the equation of state.

4.6.2 Atmosphere Treatment

A final ingredient in numerical simulations that use HRSC schemes to solve the hydrodynamic equations is the treatment of the vacuum regions. The standard approach is to add an atmosphere of very low density filling these regions (Font et al., 2002). We have followed this approach and treated the atmosphere as a perfect fluid with a rest-mass density several orders of magnitude smaller than that of the bulk matter. In particular for simulations of relativistic stars, the atmosphere's density is usually taken to be seven orders of magnitude smaller than the initial central rest-mass density of the star and when the rest-mass density on a grid point falls below the value set for the atmosphere, this point is reset to have the atmosphere rest-mass density.

Chapter 5

2D-Axisymmetric Simulations with the "Nada" Code

5.1 Introduction

In this Chapter we present several different simulations we have performed to test the accuracy of the `Nada` code to solve the Einstein equations and the hydrodynamic equations. We first concentrate on simulations in vacuum or with static matter where only the Einstein equations are solved. In particular, we consider simulations of quadrupolar gravitational waves and spherical relativistic stars with fixed matter sources. Next, we show hydrodynamic simulations of a standard shock-tube test and of spherical stars in a fixed spacetime. Finally, we present fully relativistic simulations of spherical relativistic stars in which the coupled system of the Einstein equations and the hydrodynamic equations is solved.

5.2 Quadrupolar Gravitational Waves

As the first code test in vacuum we have investigated the dynamics of low amplitude quadrupolar gravitational waves whose initial data has been derived analytically in a linearized form of the Einstein equations (Teukolsky, 1982). As these solutions have an analytic expression they provide a useful way of checking the accuracy of the numerical solution and the convergence of the code. Moreover, this solution also allows us to assess the ability of the cartoon method to evolve spacetimes with two dimensional Cartesian grids. We have investigated the evolution of quadrupolar waves both in linear and non-linear regimes and experimented with different guage conditions for these simulations.

Using the linearized form of the Einstein equations in spherical coordinates and the TT gauge, Teukolsky (1982) expressed the metric for the quadrupolar waves as

$$\begin{aligned} ds^2 = {} & -dt^2 + (1 + Af_{rr})\, dr^2 + 2Bf_{r\theta} r dr d\theta + 2Bf_{r\phi} r \sin(\theta) dr d\phi + \\ & \left(1 + Cf^{(1)}_{\theta\theta} + Af^{(2)}_{\theta\theta}\right) r^2 d\theta^2 + \left[2\,(A - 2C)\, f_{\theta\phi}\right] r^2 \sin(\theta) d\theta d\phi + \\ & \left(1 + Cf^{(1)}_{\phi\phi} + Af^{2}_{\phi\phi}\right) r^2 \sin^2(\theta) d\phi^2, \end{aligned} \tag{5.1}$$

where f_{ij} are combinations of trigonometric functions of θ and ϕ which depend on the azimuthal number m and the functions A, B and C are functions of time t and of the radial coordinate r. For instance, for even-parity ($L = 2$) and $m = 0$ data these functions are given by

$$f_{rr} = 2 - 3\sin^2\theta, \tag{5.2}$$

$$f_{r\theta} = -3\sin\theta\cos\theta, \tag{5.3}$$

$$f_{r\phi} = 0, \tag{5.4}$$

$$f^{(1)}_{\theta\theta} = 3\sin^2\theta, \tag{5.5}$$

$$f^{(2)}_{\theta\theta} = -1, \tag{5.6}$$

$$f_{\theta\phi} = 0, \tag{5.7}$$

$$f^{(1)}_{\phi\phi} = -f^{(1)}_{\theta\theta}, \tag{5.8}$$

$$f^{(2)}_{\phi\phi} = 3\sin^2\theta - 1, \tag{5.9}$$

while the functions A, B and C are given respectively by

$$A = 3\left[\frac{F^{(2)}}{r^3} + \frac{3F^{(1)}}{r^4}\frac{3F}{r^5}\right], \tag{5.10}$$

$$B = -\left[\frac{F^{(3)}}{r^2} + \frac{3F^{(2)}}{r^3} + \frac{6F^{(1)}}{r^4} + \frac{6F}{r^5}\right], \tag{5.11}$$

$$C = \frac{1}{4}\left[\frac{F^{(4)}}{r} + \frac{2F^{(3)}}{r^2} + \frac{9F^{(2)}}{r^3} + \frac{21F^{(1)}}{r^4} + \frac{21F}{r^5}\right], \tag{5.12}$$

with

$$F \equiv F(t \pm r) \text{ and } F^{(n)} \equiv \frac{d^n F(t \pm r)}{d(t \pm r)^n}. \tag{5.13}$$

The initial data is specified after choosing the function, F and its time derivatives at time $t = 0$. Following Anninos et al. (1997); Tobias (1997) we have studied waves initially centred at the origin and followed the evolution as they move outwards. The initial data need to be chosen as a combination of ingoing ($F_{in}(t+r)$) and outgoing ($F_{out}(t-r)$) waves in order to make the solution regular everywhere (Eppley 1979) and we have used the function F given by the "Eppley packet"

$$F = A \cdot (t \pm r)e^{-(t \pm r)^2}, \tag{5.14}$$

where A is the wave amplitude. We have first considered even-parity low amplitude waves with $A = 10^{-5}$ corresponding to a perturbation in the metric functions of about 0.025% respect to flat space and as a result, the evolution behaves essentially linear since, in this case, the non-linearities in the Einstein's equations play role in the evolution but not an important one (*cf.* this is discussed in the following Section).

5.2.1 Numerical Results

The initial data which is first computed in spherical coordinates and then transformed into Cartesian ones, it is evolved using the `Nada` code in the x-z plane. For the simulations discussed below the computational domain is $0 \leq x \leq 6$ and $0 \leq z \leq 6$, where π-rotation symmetry and equatorial plane symmetry are assumed about the z and x axis respectively. For the outer boundaries we have used outgoing wave boundary conditions.

By comparing the numerical solution with the linearized solution we can measure the error in the metric components for instance, in g_{xx} as

$$E = \frac{{g_{xx}}^{(a)} - {g_{xx}}^{(n)}}{{g_{xx}}^{(a)}}, \tag{5.15}$$

where ${g_{xx}}^{(a)}$ is the analytic solution and ${g_{xx}}^{(n)}$ is the numerical solution obtained with the 2D code solving the full Einstein equations.

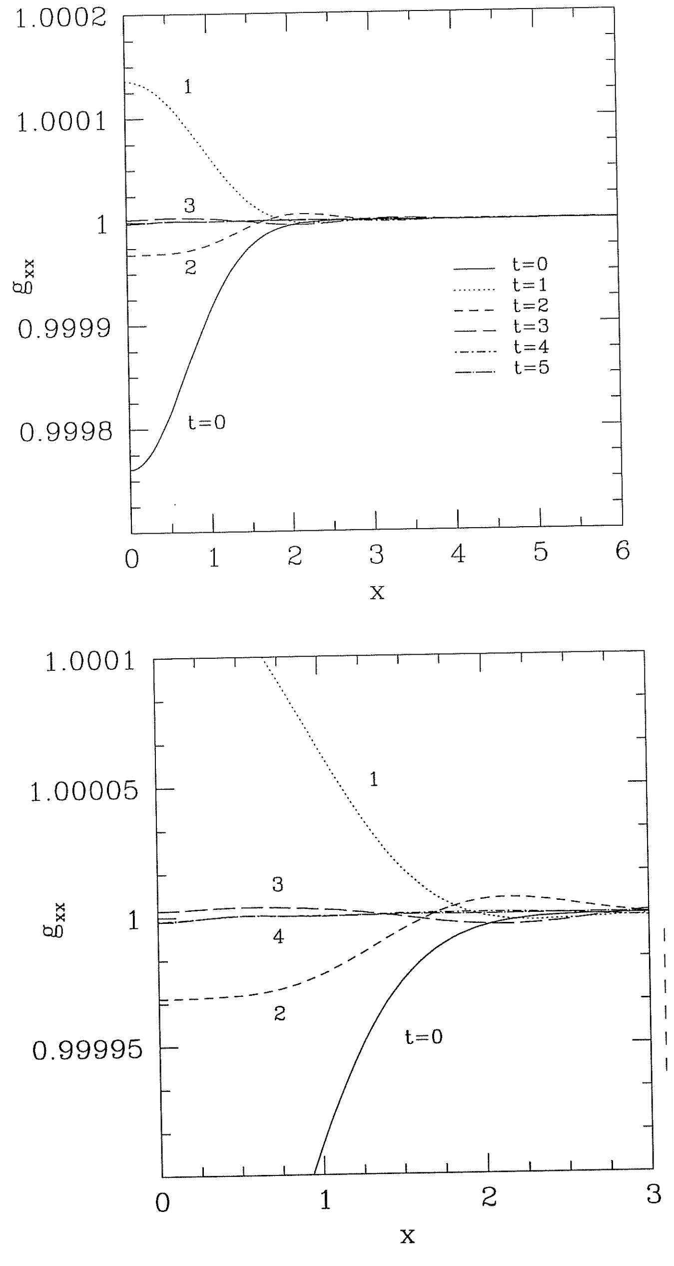

Figure 5.1: The metric component g_{xx} along the x-direction for a low amplitude, $A = 10^{-5}$, even-parity axisymmetric gravitational wave. The evolution has been carried out with 120^2 grid points and grid spacing $\Delta x = \Delta z = 0.05$. The Bottom panel zooms the region near the origin.

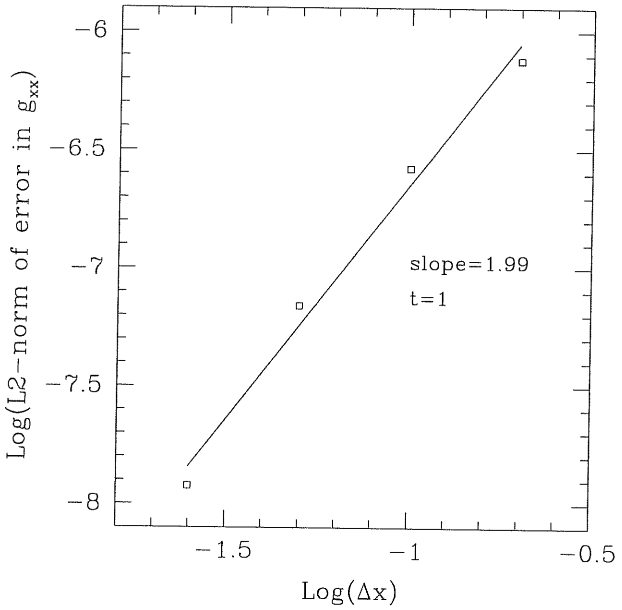

Figure 5.2: Convergence test of the code at t=1. The code achieves a convergence rate of 1.99 which agrees with the expected second order convergence since second order methods have been implemented throughout the code.

Figure 5.1 shows the evolution of g_{xx} along the x-direction at $z = \Delta z$ (*i.e.* the first grid point) for a simulation performed on a grid of 120^2 grid points with geodesic slicing. The top panel shows the g_{xx} metric component at different times while the bottom panel zooms the region near to the origin. The L2-norm of the error in g_{xx} at time $t = 5$ is about 1.3×10^{-7}. Obtaining such a low error shows that the non-linear code is able to solve the equations with great accuracy.

Another powerful way of testing the large numerical codes used in numerical relativity is to check the convergence rate of the code since an analytical solution is often not available. The numerical methods chosen in the code will determine the truncation error and, if implemented correctly they also specify the rate of convergence that the evolved quantities should achieve as the resolution increases. As we have implemented second order methods we generally expect the error to decrease by a factor of 4 when doubling the resolution. The first convergence test which we have performed is shown in Fig. 5.2 where we have plotted the logarithm of the L2-norm of the error in g_{xx}, as defined by equation

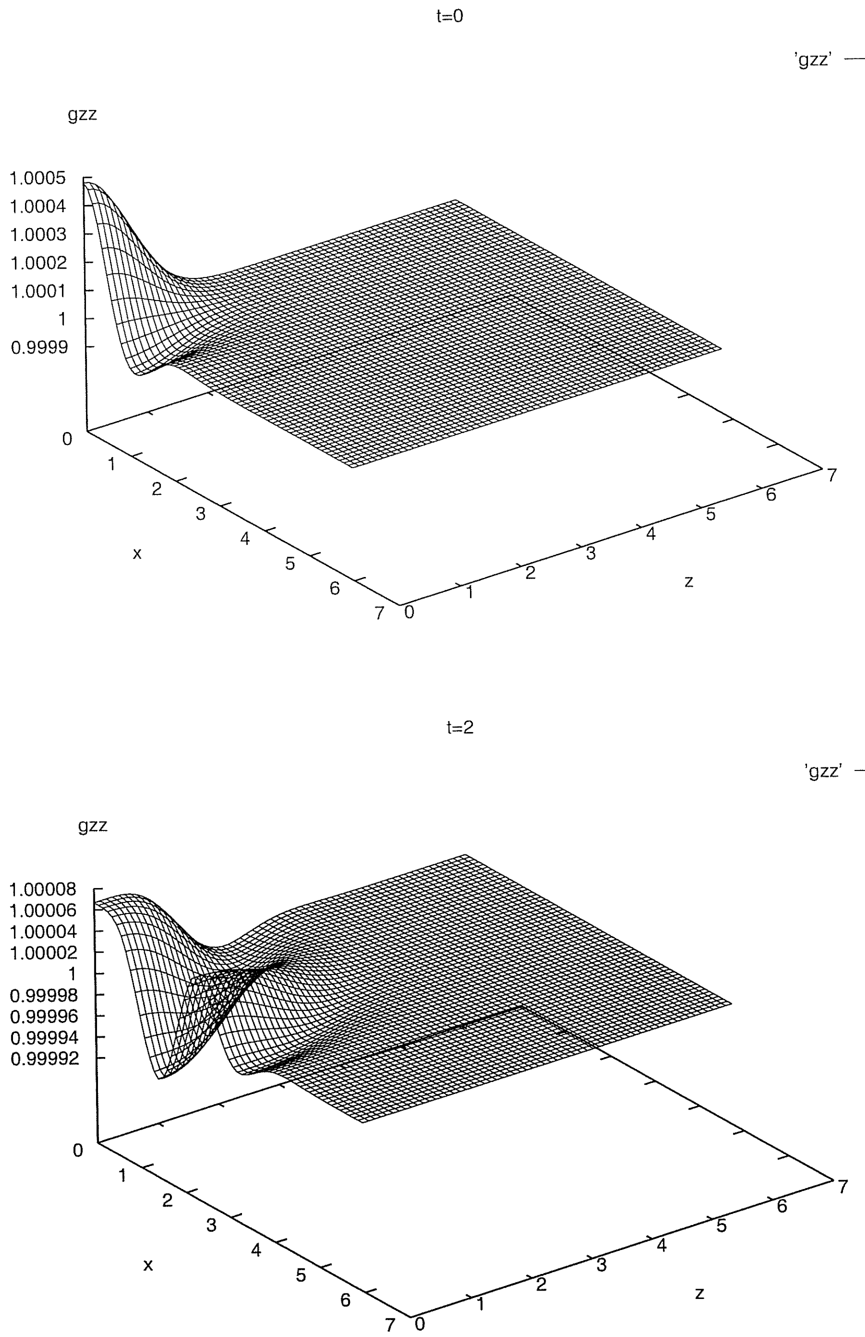

Figure 5.3: This figure shows the evolution of g_{zz} in the whole computational domain (*i.e.* $0 \leq x, z \geq 6$) at times $t = 0$ and $t = 2$. The amplitude of the initial data is $A = 10^{-5}$ and this simulation was done with 60^2 grid points.

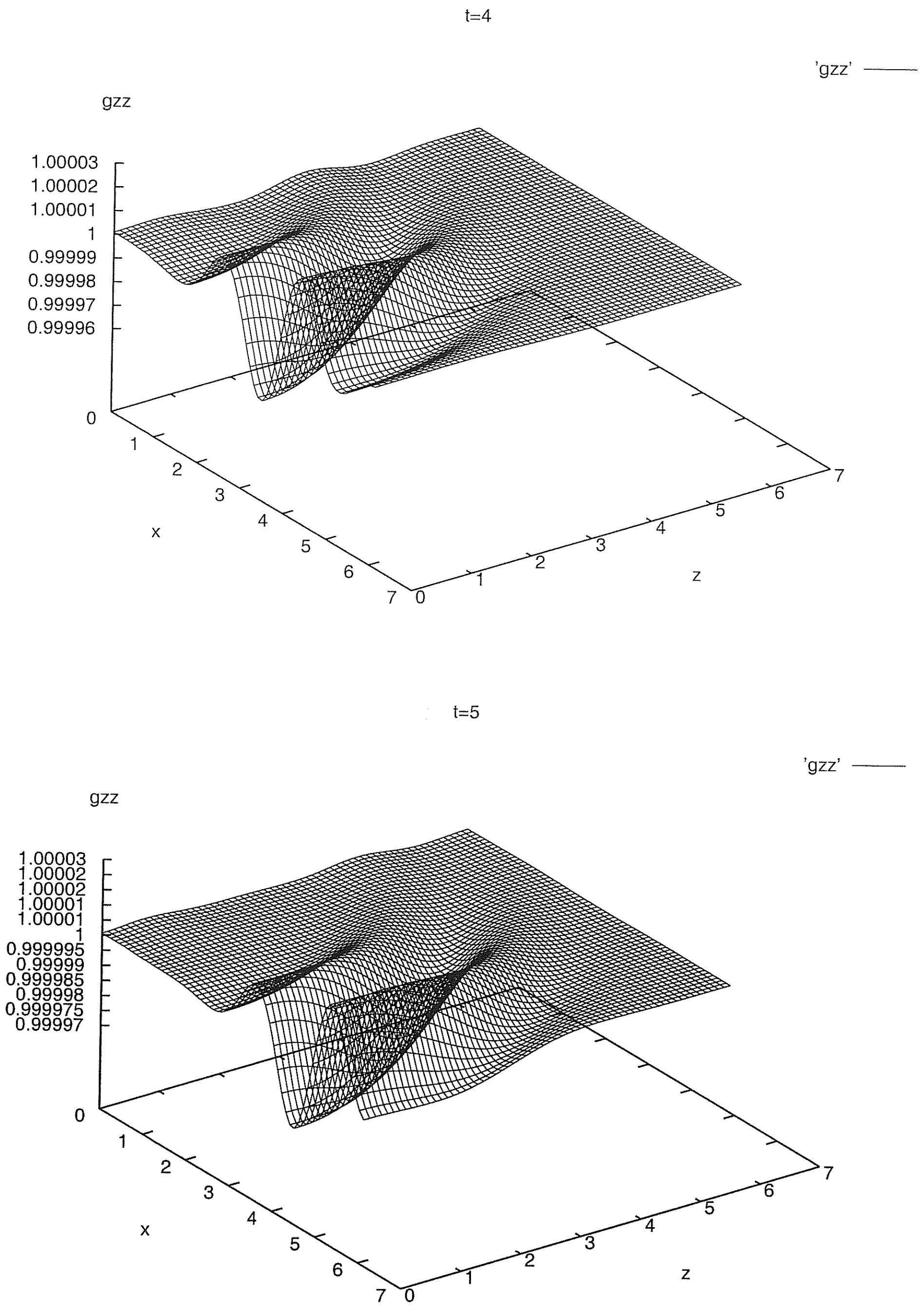

Figure 5.4: This figure shows the evolution of g_{zz} at later times $t = 4$ and $t = 5$.

(5.15), against the logarithm of Δx. As expected, we find that the error scales as $E \approx \Delta x^q$ with $q \approx 2$, thus showing that the numerical solution converges to the analytical solution at the correct rate.

Next, we have studied waves with higher amplitude, $A = 10^{-4}$ and have been able to reproduce a feature found by Anninos et al. (1997) with a similar set up and geodesic slicing. Namely, at the end of the evolution, when the wave has dispersed, the metric functions develop a dip at the origin instead of recovering the flat space values. Anninos et al. (1997) investigated in detail the cause of the dipping which we have used to test the code with different slicings. We note that Anninos et al. (1997) concluded that the dipping is due to non-linear gauge effects and although it does not converge away with higher resolution it was found that it did not appear in simulations carried out with maximal slicing, thus strongly suggesting that is due to the gauge.

In Fig.5.5 we show the metric component g_{xx} for gravitational wave with an amplitude $A = 10^{-4}$. The evolution has been carried out with 120^2 grid points and grid spacing $\Delta x = \Delta z = 0.05$. The top panel corresponds to the numerical evolution performed with geodesic slicing while the bottom panel corresponds to a simulation with the "1+log" slicing. Clearly, the simulation with geodesic slicing displays the dip near to the origin in the metric function g_{xx} at late times of the evolution when the wave has dispersed. In analogous simulations with smaller amplitude, $A = 10^{-5}$ and geodesic slicing, this dip of g_{xx} did not occur. We have also performed simulations with different resolutions and observed that the dipping does not converge away with increasing resolution. On the other hand, the bottom panel shows the same initial data evolved with the "1+log" slicing condition. We note that when this slicing is used the dip of the metric functions does not appear. These simulations confirm the results obtained by Anninos et al. (1997) who used maximal slicing to show that the dip occured only when using geodesic slicing. Furthermore, the fact that this is not observed with "1+log" slicing supports their interpretation of this being a non-linear gauge effect. A natural next step is performing the evolution of Brill waves but we found non-vacuum spacetimes more interesting and these simulations are described in the following Sections.

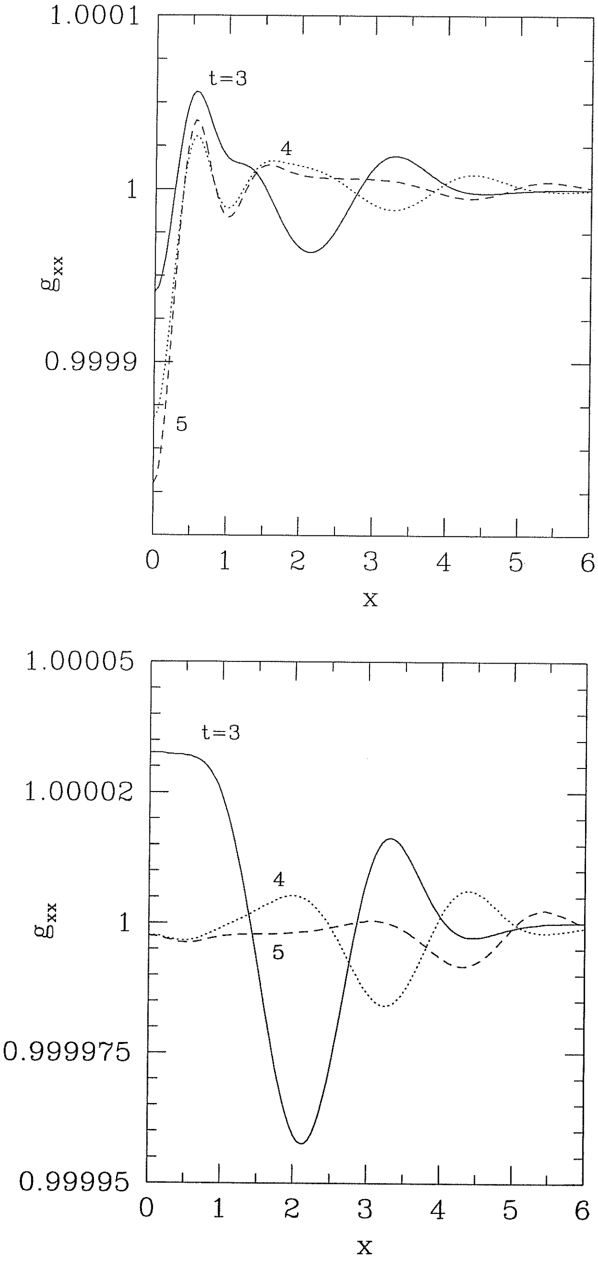

Figure 5.5: The metric component g_{xx} for gravitational wave with amplitude, $A = 10^{-4}$. The evolution has been carried out with 120^2 grid points and grid spacing $\Delta x = \Delta z = 0.05$. The numerical evolution performed with geodesic slicing is shown in the upper panel and one with '1+log' slicing is shown in the lower panel.

5.3 Hydro-without-Hydro Test: TOV Solution

We have shown that the code is able to evolve accurately vacuum axisymmetric spacetimes in the linear and nearly linear regimes. However, numerical relativity often has to face simulations of compact objects that necessarily involve strong gravitational fields and obtaining long-term stable evolutions of such systems is a challenging task which a numerical code must be able to handle accurately. Before performing full general relativistic non-linear hydrodynamic simulations of spherically symmetric relativistic stars we have carried out a series of simulations in which only the spacetime is evolved, *i.e.* following the so called *hydro-without-hydro* approach proposed by Baumgarte et al. (1999). The purpose of this approach is to solve the Einstein equations after including the matter sources that come from the solution of the Tolman-Oppenheimer-Volkoff equations (Tolman 1939; Oppenheimer & Volkoff 1939; hereafter TOV) for a static spherically symmetric star without actually solving the general relativistic hydrodynamic equations during the spacetime evolution. In this way, it is possible to assess the stability of a spacetime evolution code and its capability of evolving accurately strong gravitational fields in spacetimes with static matter without having to worry about the hydrodynamical evolution. Thus, this approach it is both a testbed and a preliminary step towards making fully relativistic dynamical simulations of TOV stars.

5.3.1 Numerical Results

We have considered polytropic stellar models with the equation of state $P = k\rho^{1+1/N}$, where k is the polytropic constant and N is the polytropic index. In order to compare our evolutions with results from Baumgarte et al. (1999), we have first considered the same initial model, an $N = 1$ polytrope with polytropic constant $k = 1$ and central rest-mass density $\rho_c = 0.2$ (we recall that here we use dimensionless units in which $G = c = M_\odot = 1$). For this values the star has a mass $M = 0.157$ and Schwarzschild radius $R = 0.866$ that corresponds to an isotropic radius of the star $R_{iso} = 0.7$. The compactness of the star is $M/R = 0.18$.

In Fig. 5.6 we show the trace of the extrinsic curvature, K, and the conformal

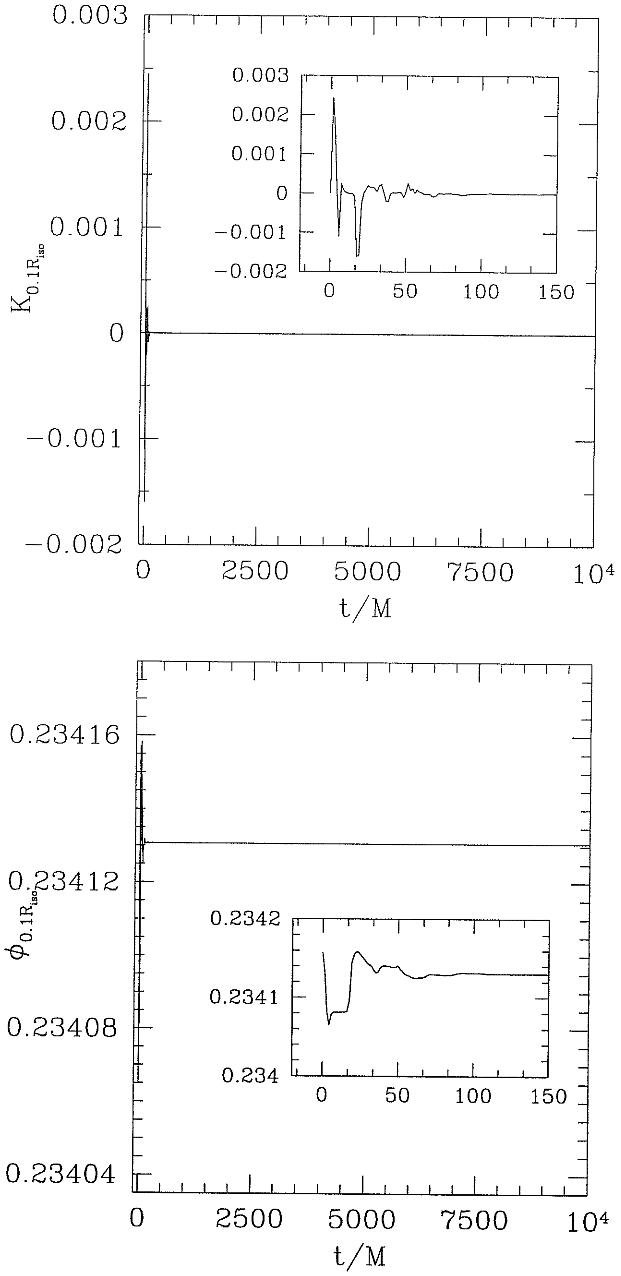

Figure 5.6: Trace of the extrinsic curvature, K, and the conformal exponent, ϕ, at the first evolved grid point (i.e. at a radial distance of 0.065 from the centre). The grid spacing is $\Delta x = \Delta z = 0.046$ and we have used 64^2 points

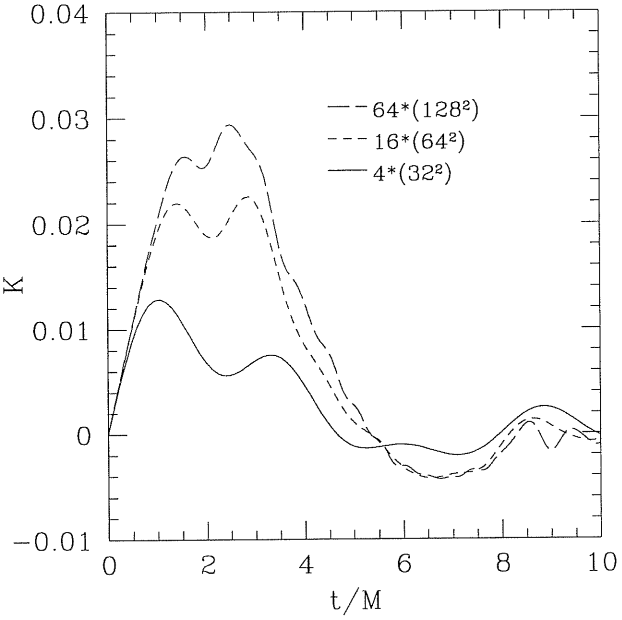

Figure 5.7: Convergence test for the trace of the extrinsic curvature at a distance $r = 0.36R_{iso}$ from the centre of the star. Second-order convergence is lost for times greater than $t \approx 0.2$ as a result of the finite difference at the surface of the star being first-order.

exponent, ϕ, at the first evolved grid point (i.e. at a radial distance of 0.065 from the centre). The computational domain is defined as $0 \leq x \leq L$ and $0 \leq z \leq L$, where the outer boundaries are located at $L = 3$ and we use a 64^2 grid (note that we show results at the first grid point $(\Delta x, \Delta z)$, since the centre of the star is a boundary point and not an evolved mesh point). We terminated the computation at time $t \approx 12739$ M and found no sign of instability. The evolution settles down into an essencially static solution after a short initial phase at the beginning of the evolution during which numerical noise caused by the finite differencing, by the surface of the star and by the location of boundaries being at a finite distance, propagates off the grid.

We have also checked the convergence of the code and evolved the same initial data on grids with $32^2, 64^2$ and 128^2 grid points with the location of the outer boundaries being kept fixed at $L = 3$ so that the resolution is doubled. The error should decrease by a factor of 4 when doubling the resolution as we use second order accurate schemes. In Fig. 5.7 we plot the trace of the extrinsic curvature K multiplied by a factor of 4, 16 and 64 for

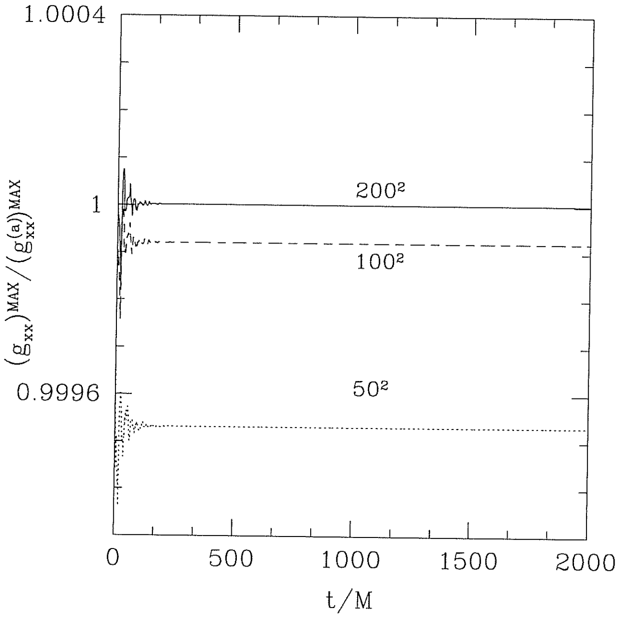

Figure 5.8: Maximum value of g_{xx} normalize to the analytic value, for evolutions with $50^2, 100^2$ and 200^2 grid points. The initial model consist of a TOV with $N = 1$, $K = 100$ and central density $\rho_c = 1.28 \times 10^{-3}$.

simulations with $32^2, 64^2$ and 128^2 grid points respectively. We show the value of K at a distance $r = 0.36R_{iso}$ which corresponds to the first grid point of the lowest resolution run. We note that the analytic solution is $K = 0$ thus any deviation from this value is effectively a measure of the error in the evolution. In the early part of the evolution (*i.e.* $t \lesssim 0.2$) K converges at second order, but rather soon the convergence rate is no longer second order. This effect has been investigated by Baumgarte et al. (1999) and Font et al. (2000), and is the result of the non-smoothness of the second order spatial derivatives at the surface of the star which causes the decrease in the convergence rate. As a result we conclude we have not encounter any problem in performing long-term evolutions of the TOV spacetime when matter sources are kept constant.

We have also performed evolutions for other different initial data and we have observed an analogous behavior. In Fig. 5.8 we report the maximum in the metric component g_{xx}, normalized to the initial analytic value $g_{xx}^{(a)}$ on grids with $50^2, 100^2$ and 200^2 grid points. "1+log" slicing was used for all of these dynamical simulations. The initial model consisted of a TOV solution with $N = 1$, $K = 100$ and central density $\rho_c = 1.28 \times 10^{-3}$. The mass of this TOV star is $M = 1.4$ and the radius $R = 9.59$. We note that the evolutions have not shown any sign of instabilities and so these runs were terminated without code crash at $t = 2000M$. Again, after the initial stages of the numerical simulation the evolution settles down into the numerical solution which converges to the analytic solution with increasing resolution.

5.4 Relativistic Shock-tube Test

As a first test of the solution of the relativistic hydrodynamic equations we have performed a standard one dimensional shock-tube problem. In this test, two uniform and different fluid states, are initially separated by an interface which is then instantaneously removed. The initial data taken for the left state is $P_L = 13.33, \rho_L = 10.00, v_L = 0.00$ and for the right state $P_R = 0.66 \times 10^{-6}, \rho_R = 1.00, v_R = 0.00$ (in $c = G = M_\odot = 1$ units) with the initial interface located at $x = 0.5$. The fluid is assumed to be an ideal fluid with equation of state $P = (\Gamma - 1)\rho\epsilon$ and $\Gamma = 5/3$.

Results of the evolution are shown in Fig.5.9, where we plot the solutions for the pressure, density and z-component of the fluid velocity for a shock-tube test along the z-direction at time $t = 0.25$. The solid line represents the exact solution of the shock-tube problem computed using the public domain code *RIEMANN* by J.M. Martí and E. Müller. The numerical solution is represented by crosses. We have used 400 grid points in the z-direction and a grid spacing of $\Delta x = 1/400$. The simulation was carried out using a van Leer MC reconstruction and a third order Runge-Kutta scheme to integrate the evolution equations forward in time. Overall, these plots show that the agreement between the exact solution and the numerical solution is very good for all three hydrodynamic variables, especially in the smooth parts of the solution where the scheme is second-order. At the shock the accuracy is reduced because of the scheme being only first-order but still the ability of our code to capture the shock is nevertheless, very good.

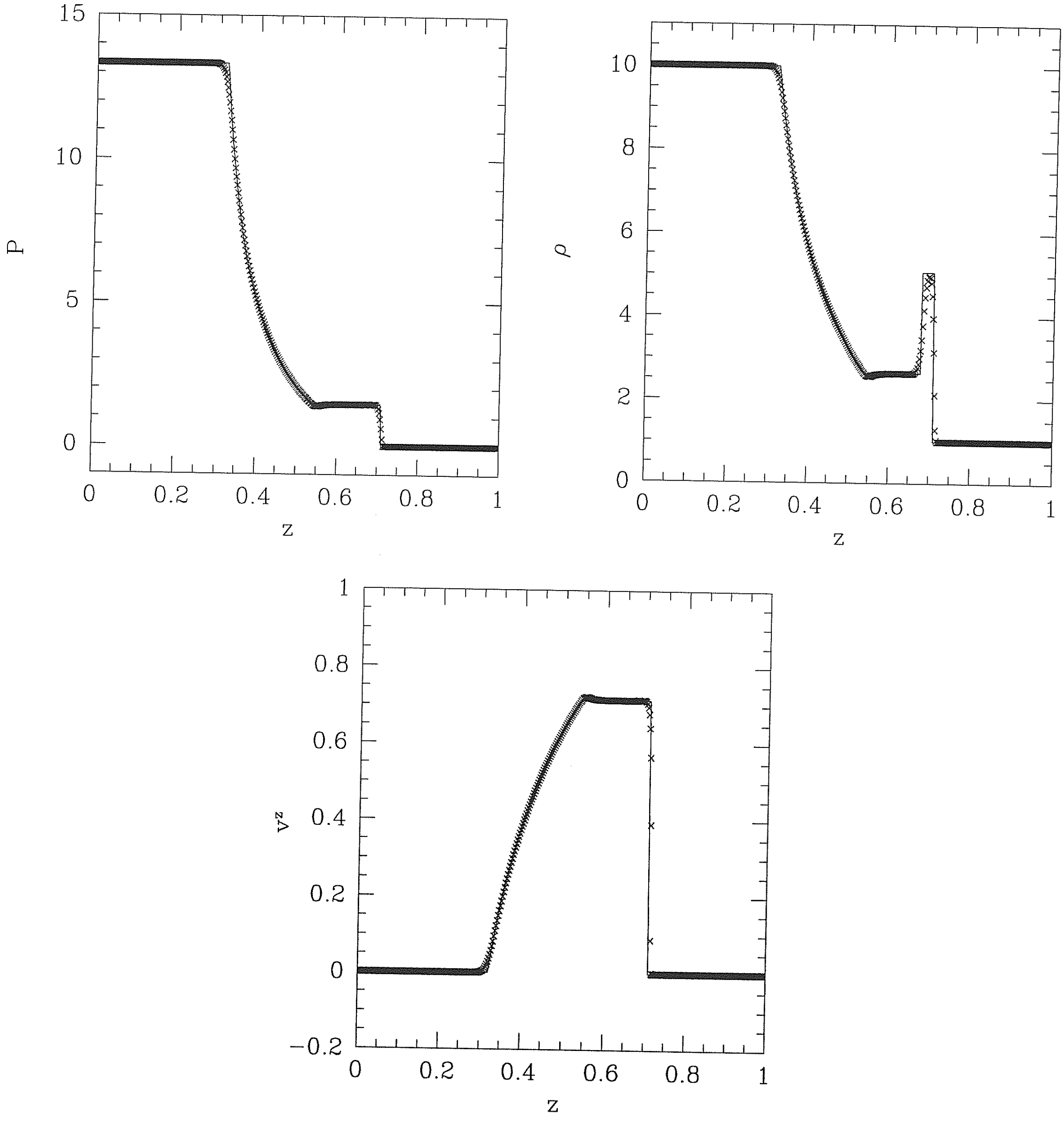

Figure 5.9: Pressure, density and z-component of velocity profiles at time $t = 0.25$ for the solution of the shock-tube problem along the z-direction with the evolution code. The exact solution is represented by the solid line and numerical solution by crosses.

5.5 Evolution of TOV Stars

We have also used the solution of the TOV equations to test the capability of the code to perform long-term stable numerical simulation of neutron stars. In order to check the hydrodynamical evolution independently from the spacetime evolution we have followed here the standard approach of keeping the spacetime fixed during the numerical evolution, that is known as Cowling approximation (Cowling 1941). In analogy with corresponding approximation in perturbative studies of stellar oscillations in which the metric component (or the gravitational potential in Newtonian studies) are kept constant. Section 5.5.2, on the other hand, is devoted to fully relativistic simulations where both the Einstein equations and the hydrodynamic equations are solved by our evolution code.

5.5.1 TOV in a Fixed Spacetime

We first show consider an initial model consisting of a polytropic star of mass $M = 1.65$, central rest-mass density $\rho_c = 1.0 \times 10^{-3}$, polytropic constant $k = 123.5$ and polytropic index $N = 1$ (we recall that these quantities are expressed in dimensionless units with $G = c = M_\odot = 1$). Although, we simply use a polytropic equation of state, these parameters lead qualitatively to an initial model which resembles those assumed for realistic neutron stars.

In the upper panel of Fig. 5.10 we plot with a dashed line the central rest-mass density along the x-direction corresponding to an evolution with $\Delta x = 0.6$ and with a solid line the evolution with $\Delta x = 0.3$. The lower resolution simulation shows a small secular increase of the central rest-mass of about 2% after 15 ms. The secular increase in the higher resolution simulation is much smaller, less than 0.2% when the simulation was terminated at time $t = 15$ ms, showing that the numerical solution converges to the initial solution with increasing resolution. The convergence of the hydrodynamic 2D code is at least second order in smooth parts of the solution and, as expected, it is reduce at local extrema where the schemes are only first-order accurate.

It has been shown (Font et al., 2002) that the truncation errors are enough to excite small periodic radial oscillations which manifest themselves for instance, as periodic

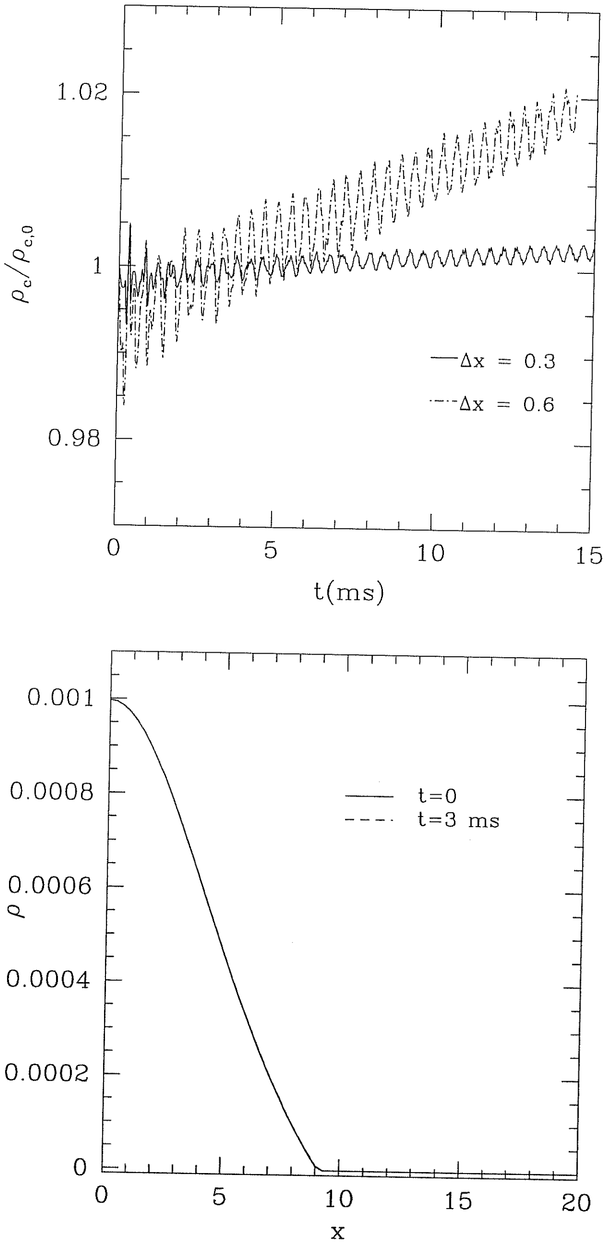

Figure 5.10: The upper panel shows the evolution for the central rest-mass density of polytropic star of mass $M = 1.65$, polytropic constant $k = 123.5$ and polytropic index $N = 1$ with two different resolutions, $\Delta x = 0.3, 0.6$. The secular increase in the central rest-mass density is about 2% after 15ms with the coarsest resolution. The lower panel shows the rest-mass density profile along the x-axis at the initial time $t = 0$ and at $t = 3$ ms with $\Delta x = 0.3$

variations of the central density. In the top panel of Fig. 5.10 we see that the damping of the periodic oscillations of the central rest-mass density is very small during the whole evolution demostrating the low numerical viscosity of the schemes implemented. The bottom panel shows the rest-mass density profile along the x-direction at the initial time and at time $t = 3$ ms obtained with a grid spacing of $\Delta x = 0.3$, which shows that the agreement is very good.

The power spectrum of the evolution of the central density provides the frequencies of the fundamental mode oscillation and of its overtones, which can be compared with the corresponding frequencies computed by perturbative techniques. Although the excited oscillations are purely numerical in origin (*i.e.* their amplitude converges to zero as the resolution increases) they still represent the oscillation modes of the relativistic star and their frequencies should agree with the eigenfrequencies computed by linear perturbation analysis. For the purposes of testing the code and comparing with independent results we have focused on a different initial model that has been extensively investigated with both numerical simulations by Font et al. (2000, 2002). This model is a relativistic star with $N = 1$, polytropic constant $k = 100$ and central rest-mass density $\rho_c = 1.28 \times 10^{-3}$ so that its mass is $M = 1.4$ and its radius $R = 9.59$. We have evolved this initial data with our non-linear code with a grid resolution $\Delta x = 0.1$ using both ICN and third order Runge-Kutta ODE solvers. In Fig. 5.11 we show with a solid line the power spectrum of the evolutions of the central rest-mass density while the dashed vertical lines indicate the fundamental frequency and the first six overtones computed by Font et al. (2000) with a nonlinear hydrodynamic code using spherical polar coordinates (in Table 5.1 we also report the results obtained with the 3D CACTUS code, Font et al. 2002). The top panel plots results computed from the evolution with ICN while the bottom panel is for results obtained with third order Runge-Kutta method. In both cases, the agreement for the the fundamental frequency and all of the overtones is very good. We note that the relative error between the fundamental frequency with ICN method is about 2% while it is only 0.2% with the Runge-Kutta scheme. We have also computed the Fourier transform of the evolution of the rest-mass density at other grid points within the star and the results confirm that the frequencies computed are independent of the position where the variation in the rest-mass

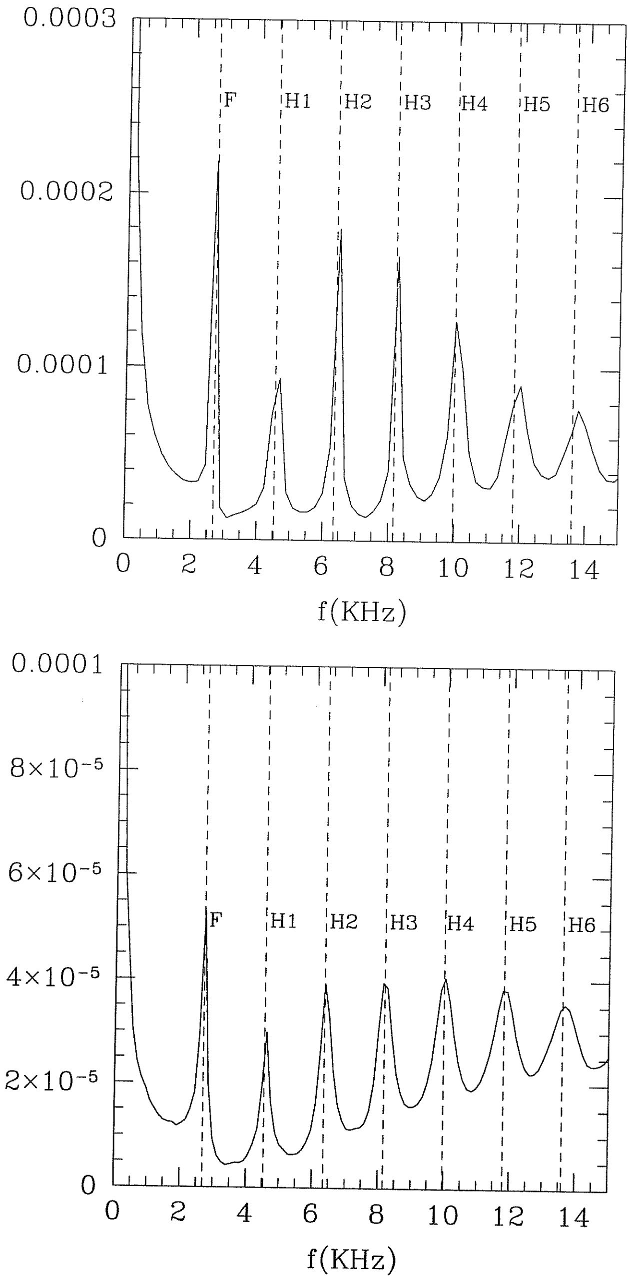

Figure 5.11: Power spectrum of the evolution of the central rest-mass density for an $M = 1.4$, $K = 100$, $N = 1$ polytrope in the Cowling approximation. F represents the frequency of the fundamental mode and H1-H6 are the first six overtones computed by Font et al. (2000). The agreement is excellent for both the simulations carried out with ICN (top panel) and for the one with Runge-Kutta (bottom panel).

Table 5.1: Comparison of the radial oscillation frequencies obtained within the Cowling approximation with the 2D Nada code and with two independent nonlinear codes.

Mode	Nada code ICN (KHz)	Nada code RK-3 (KHz)	3D CACTUS code (KHz)	2D code (Font et al.) (KHz)
F	2.668	2.705	2.696	2.701
H1	4.555	4.598	4.534	4.563
H2	6.444	6.272	6.346	6.352
H3	8.220	8.184	8.161	8.129
H4	9.983	9.999	9.971	9.875
H5	11.90	11.82	11.81	11.66
H6	13.77	13.67	13.60	13.42

density is measured. This is what expected for global oscillations.

5.5.2 TOV in a Evolved Spacetime

The coupling of the Einstein equations and the general relativistic hydrodynamic equations has first been tested using the TOV solution. In analogy to what happens in the Cowling approximation, truncation errors excite oscillations in the star. Now, however, the truncation errors come not only from the hydrodynamic part of the code but also from the spacetime part solving the full set of Einstein equations.

We have first tested the long-term stability of the code by evolving the TOV model with central rest-mass density $\rho_c = 1.0 \times 10^{-3}$, polytropic constant $k = 123.5$, polytropic index $N = 1$ and using 96^2 grid points with $\Delta x = 0.3$. In Fig. 5.12, the top panel shows the time evolution of the maximum density normalized to its initial value while the bottom panel shows the time evolution of the trace of the extrinsic curvature at the centre of the star. We show in both plots that our code can perform long-term stable fully relativistic evolutions of spherical stars without any problem.

We have also computed the eigenfrequencies of the coupled evolution of the TOV star with $k = 100$, $N = 1$ and central rest-mass density $\rho_c = 1.28 \times 10^{-3}$ which has been discussed above under the assumption of a fixed background spacetime. In particular, in Fig. 5.13 we show the power spectrum of the central rest-mass density (solid line) computed from a simulation carried out with 128^2 grid points and a grid spacing of $\Delta x =$

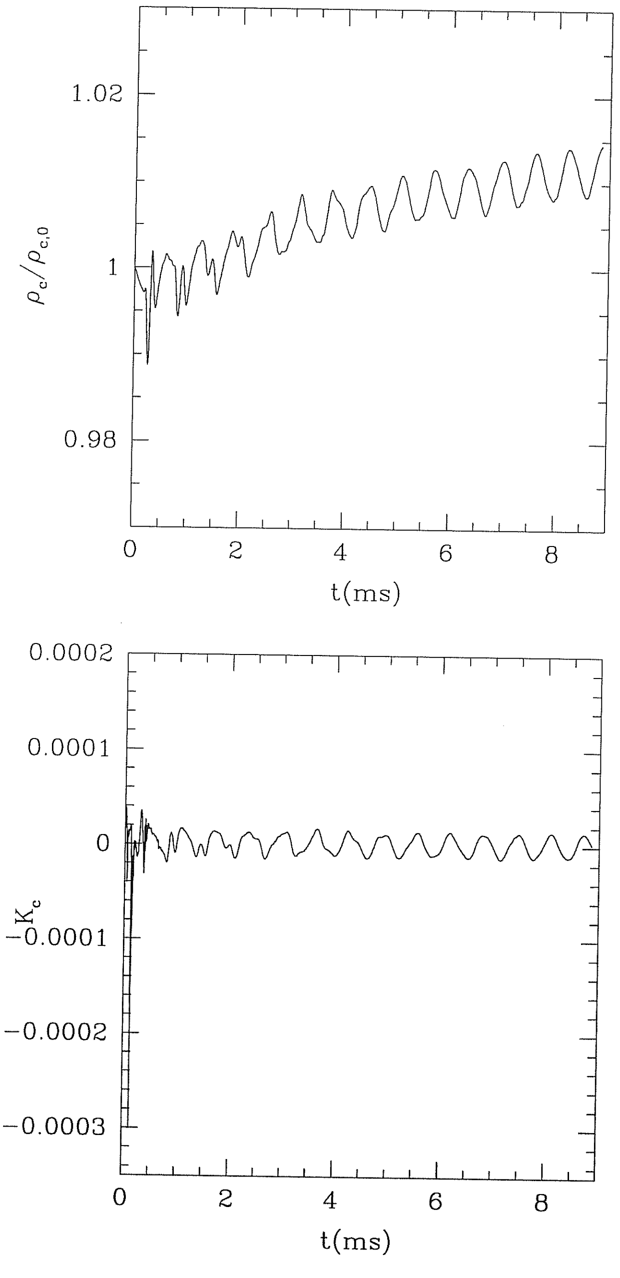

Figure 5.12: The top panel shows the time evolution of maximum density normalized to its initial value, for a TOV star using 96^2 grid points with $\Delta x = 0.3$. The bottom panel shows the time evolution of the trace of the extrinsic curvature at the centre.

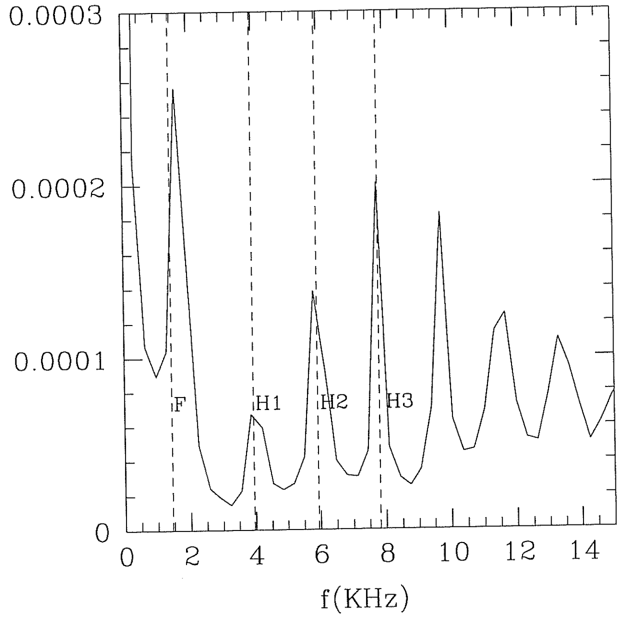

Figure 5.13: The power spectrum of the evolution of the central rest-mass density for an $M = 1.4$, $k = 100$, $N = 1$ polytrope in a coupled evolution. F represents the frequency of the fundamental mode and H1-H3 are the first three overtones.

$\Delta z = 0.1$. The eigenfrequencies computed by Kokkotas (2001) using linear perturbative techniques are also shown (dashed lines). We note that the locations of the frequency peaks for the fundamental mode and the first three overtones for which we have the data is in relatively good agreement with the perturbative results. The fundamental frequency peak computed from our simulations is located at 1.61 KHz while the perturbative techniques give 1.44 KHz. We have performed several different simulations of the same TOV star with lower resolutions and found that the computed frequencies converged to the value given by the linear perturbative techniques as the resolution increased. Furthermore, we have also checked the convergence of the coupled evolutions by performing simulations of this same TOV model with 50^2, 100^2 and 200^2 grid points and computed the L2-norm of the trace of the extrinsic curvature on a spherical region inside the TOV star. This convergence test is shown in Fig. 5.14, in which we have plotted the logarithm of the L2-norm of the extrinsic curvature (recall that the trace of the extrinsic curvature is zero for a TOV, thus deviations during the evolution from this value are a measure of the numerical error) against

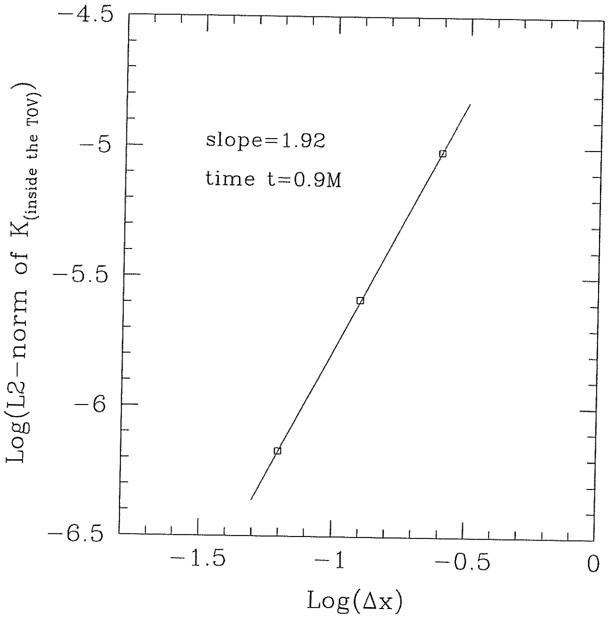

Figure 5.14: Convergence test for a coupled evolution of a TOV star. We obtained approximate second-order convergence (*slope* = 1.92) before the convergence rate is reduced as a results of the numerical schemes being only first order at the surface of the star.

the logarithm of the grid spacing. The slope being 1.92, at time $t = 0.9M$ (*i.e* 80 iterations in the 200^2 simulation), confirms that the convergence is approximately second-order inside the star. We note that, as we have previously discussed, the convergence rate is reduced at later times during the evolution as a result of the reconstruction schemes being only first-order at the surface of the star, but the code still converges to the TOV solution. Therefore, we conclude that the numerical solution converges to the exact TOV solution in the limit $\Delta x \longrightarrow 0$

Chapter 6

Conclusions

The work presented in this Thesis can be summarized as follows:

- We have presented the study of the oscillation properties of non-selfgravitating tori orbiting around Kerr black holes. This work extends the previous investigations of the oscillation properties of relativistic tori in a Schwarzschild background and their importance in explaining the HFQPOs in X-ray binaries containing a black hole candidate. We have considered the axisymmetric p-mode oscillations of relativistic tori assuming a vertically integrated description. By means of a local analysis in a Kerr spacetime we have determined the relations between acoustic and inertial waves, showing that both are present in the oscillations of geometrically thick discs and that they play a different role depending on the radial size of the disc and on the position of the rest-mass density maximum. We have then computed the eigenfunctions and eigenfrequencies of the axisymmetric p-modes for a large variety of background models which differed either in the spin of the black hole or in the distributions of specific angular momentum considered.

  The p-mode oscillations of vertically integrated tori in a Kerr spacetime possess all of the most important features already encountered in a Schwarzschild spacetime. Firstly, the fundamental eigenfrequencies depend on the position of the rest-mass density maximum and on the radial size of the discs, increasing as the latter decreases. Secondly, the fundamental eigenfrequencies tend to the values of the radial epicyclic frequencies at the position of the mass density maxima as the radial sizes of the tori tend to zero. Finally, for tori constructed with constant specific angular momentum, the first and second eigenfrequencies are in the harmonic ratio 2:3 of small integers. This ratio is not exact but is very accurately satisfied with deviations of $\sim 10\%$ at most. On the other hand, for non-constant specific angular momentum, we have found that a harmonic sequence is still present for sufficiently large tori, but the deviation from a precise 2:3 ratio increases, being $\sim 20\%$ at most.

We have also compared the linear perturbative approach with non-linear hydrodynamic simulations of geometrically thick discs performed with a 2D general relativistic hydrodynamic code. We have calculated the power spectrum of the time evolution of the L_2 norm of the rest-mass density for several models and computed the ratio of the frequencies corresponding to the fundamental mode and the first overtone. This comparison has shown results coming from the two distinct approaches are in very good agreement for most of the models with differences of $\sim 5\%$ at most.

We have discussed the detectability of the oscillations of perturbed relativistic tori via their gravitational wave emission. In good agreement with Zanotti et al. (2003), the chances for the detection of gravitational waves, for tori with non-constant specific angular momentum, are good and within the sensitivity curves of LIGO and VIRGO for galactic sources, but only marginal for extragalactic sources located at 20 Mpc.

We have also investigated the implications that *p*-mode oscillations could have for the HFQPOs observed in X-ray binaries containing a black hole candidate. In a recently proposed model, the oscillations of a sub-Keplerian flow (*i.e.* a torus) near to the black hole are used to explain many of the features of the HFQPOs and, in particular, the 2:3 ratio in the peaks of the power spectral density (Rezzolla et al., 2003a). In this model, the measure of the oscillation frequencies and the knowledge of the *p*-mode properties can be used to measure directly the black hole properties such as the mass and spin. In view of this, we have considered whether an equivalent interpretation of the HFQPO phenomenology can also be made in terms of a purely Newtonian description of physics. For doing this, we have performed a global analysis of vertically integrated Newtonian tori following the same mathematical and numerical approach developed for tori in a Kerr spacetime. Our results indicate that, at least *qualitatively*, the p-mode oscillations of Newtonian tori preserve all of the properties encountered in their relativistic counterparts. Furthermore, while *quantitative* differences do exist between the two frameworks, it may be difficult to distinguish between the two unless the oscillation frequencies are measured together with the radial extension of the torus L, or the location of the mass density maximum $\varpi_{\rm max}$.

- We have also contributed to the development of a new 3D, parallel and general relativistic hydrodynamic code, the `Whisky` code, which has been initially written in collaboration with L. Baiotti (SISSA) and I. Hawke (AEI,Golm), but also the Universities of Valencia (Spain) and Thessaloniki (Greece) have contributed to its development. The `Whisky` code implements high resolution shock capturing methods and exploits the spacetime evolution provided by the `Cactus` code developed at the AEI. We have presented our main contributions to the code, *i.e.* the implementation of the approximate Riemann solvers (HLLE, Roe and Marquina) and the tests we have carried out. We showed that the code passes with excellent accuracy shock-tube tests and is able to carry out accurate long-term evolutions of isolated relativistic stars. We found that accurate simulations of non-selfgravitating tori orbiting around black holes were not possible. We believe this inaccurate simulations are the result uniquely of a lack of spatial resolution. While higher resolution with more than 100^3 grid points can be used, would be computationally extremely expensive and certainly it would not allow for a systematic study of the dynamics of self-gravitating tori, in general, and of the runaway instability in particular. It is important also to mention that the `Whisky` code has recently been used to investigate the dynamics of the gravitational collapse of rotating neutron stars to form Kerr black holes.

- An important part of the work presented here has concentrated on developing computational tools needed in numerical simulations and which can easily be applied to investigate a number of different astrophysical scenarios. Starting in 2003, we have developed from scratch a new two dimensional, fully relativistic and non-vacuum code, the `Nada` code, for the study of the dynamics of axisymmetric systems and in particular with the aim of investigating the dynamics of geometrically thick self-gravitating tori orbiting around black holes and assessing whether these systems may be subject to the runaway instability. The `Nada` code solves the system of Einstein equations and the general relativistic hydrodynamic equations. It implements high resolution shock capturing methods and the Einstein equations are cast into a system of constraint and evolution equations.

In a series of tests for the validation of the code we have shown that the 2D code is convergent. We have first tested the spacetime part of the code (*i.e.* the part solving the Einstein equations) and investigated the performance of the code during the evolution of quadrupolar gravitational waves and in long-term numerical simulations of TOV stars. We have shown that the code is stable and accurate, and that is able to carry out simulations of TOV star when the matter sources are kept constant without any difficulty. Through these tests we have shown that the spacetime part of the code which uses the cartoon method to impose the axisymmetry condition, is able to carry out long-term and accurate simulations of TOV stars.

We have also tested the ability of the hydrodynamic part of the `Nada` code to solve accurately the general relativistic hydrodynamic equations. We have shown the good capabilities of the code to resolve shocks through shock-tube tests. We have also successfully performed long-term evolutions of TOV stars in a fixed spacetime and have compared the computed frequency of fundamental radial oscillations with independent calculations made with other numerical codes. These comparisons have shown that the agreement is excellent and the relative error is at most 1%.

Coupled numerical simulations of TOV stars have proved to be stable. We have computed the power spectrum of the evolution of the central rest-mass density and located the peak for the fundamental mode at 1.61 KHz (computed from a simulation with grid spacing $\Delta x = \Delta z = 0.1$) while linear perturbative analysis give 1.44 KHz. We note that the frequencies computed from the power spectra obtained from our simulations converge to the values obtained by means of linear perturbative techniques as the resolution is increased. Furthermore, we have shown that the numerical solution inside the star converges to the TOV solution at approximately second-order until the convergence rate is reduced as a result of the numerical schemes not being second-order at the surface of the star. We note even when the convergence rate is smaller than second-order, the numerical solution still converges to the TOV solution.

We have recently implemented in the `Nada` code the possibility to excise black holes. This is now being tested with single black hole simulations and we are also working on the implementation of excision for the hydrodynamic variables. After the excision techniques are sucessfully tested, the `Nada` code will be used to carry out numerical simulations of tori around a black holes.

Appendix A

On the Dispersion Relation for Tori around Kerr Black Holes

We here briefly discuss the simplifications of equations (2.12)–(2.14) that lead to the homogeneous linear system with matrix form (2.15). In particular, we start from the analogy of equation (2.12) with its Newtonian counterpart, equation (2.36), whose pressure-gradient term $\delta Q'$ and centrifugal term $2\varpi\Omega\delta W$ are of about the same order. The reason for this is that the inertial-acoustic modes are the results of small deviations from the equilibrium between the centrifugal force and the pressure gradients, which produce the small perturbative radial velocity field expressed by the first term in equation (2.36).

We expect this to be true also in the general relativistic case and assume, therefore, that the second and the third terms in equation (2.12) are of the same order. We also note that since $u^t = \mathcal{O}(1)$, then $\alpha = \mathcal{O}(1)$ and thus the leading order coefficient in the square bracket multiplying δW is the first one, *i.e.* $(\Delta^{3/2}/A)(A/\varpi^2)'\Omega$.

Because now $\Delta \sim \varpi^2$ and $A \sim \varpi^4$, it is not difficult to show that the ratio of the third to the first term in equation (2.12) is given by

$$\frac{\alpha(\Delta/\varpi^2)\delta Q'}{(\Delta^{3/2}/A)(A/\varpi^2)'\Omega\delta W} \sim \frac{k}{\Omega}\frac{\delta Q}{\delta W}\,, \tag{A.1}$$

where we have replaced radial derivative with a factor ik. Since we assume the ratio (A.1) to be $\mathcal{O}(1)$, we can deduce that

$$\frac{\delta W}{\delta Q} \sim \frac{k}{\Omega} \,. \tag{A.2}$$

Using now this order of magnitude estimate, we can consider the azimuthal Euler equation (2.13) and evaluate the ratio between the first and third terms, which is given by

$$\frac{(\sigma\varpi^2\sqrt{\Delta}/A)\delta W}{[A\sigma\alpha(\omega-\Omega)/\Delta\varpi^2]\delta Q} \sim \frac{1}{\Omega}\frac{\delta W}{\delta Q} \sim \frac{k}{\Omega^2} \,, \tag{A.3}$$

As a result, in the limit of large wavenumbers considered here (*i.e.* for $k \to \infty$), the third term in equation (2.13) can be neglected when compared with the first one.

Finally, in the continuity equation (2.14), we note that all of the terms except the first one are multiplied by $\widetilde{\Gamma}$ or comparable terms [*e.g.* $P'/(E+P)$]. The latter is rather small and of the order $\sim (c_s/c)^2$, where c_s and c are local sound speed and the speed of light, respectively. As a result, the leading terms we retain are the first and the second one, for which the radial derivative introduces a factor ik balancing the smallness of $\widetilde{\Gamma}$.

Appendix B

"Cartoon" to the GR Hydrodynamic Equations

We have solved the hydrodynamic equations in Cartesian coordinates using the formulation decribed by Banyuls et al. (1997). We make use of the cartoon method to obtain the necessary boundary conditions that allow for the reconstruction in the y-direction and the consequent evaluation of the fluxes in this same direction using Roe approximate Riemann solver.

B.1 Relativistic Shock-tube Test

The initial data taken for the left state is $P_L = 13.33, \rho_L = 10.00, v_L = 0.00$ and for the right state $P_R = 0.66 \times 10^{-6}, \rho_R = 1.00, v_R = 0.00$. Initially, the left and right states are separated by an interface located at $x = 0.5$. The fluid is assumed to be an ideal fluid with equation of state $P = (\Gamma - 1)\rho\epsilon$ and $\Gamma = 5/3$. In Fig. B.1 we show the solutions for the pressure, density and x-component of the fluid velocity for a shock-tube test along the x-direction at time t=0.25. The solid line represents the exact solution of the shock-tube problem computed using the public domain code *RIEMANN* by J.M. Martí and E. Müller and the numerical solution is represented by crosses. We have used 400 grid points in the x-direction and a grid spacing of $\Delta x = 1/400$. This simulation was performed using the van

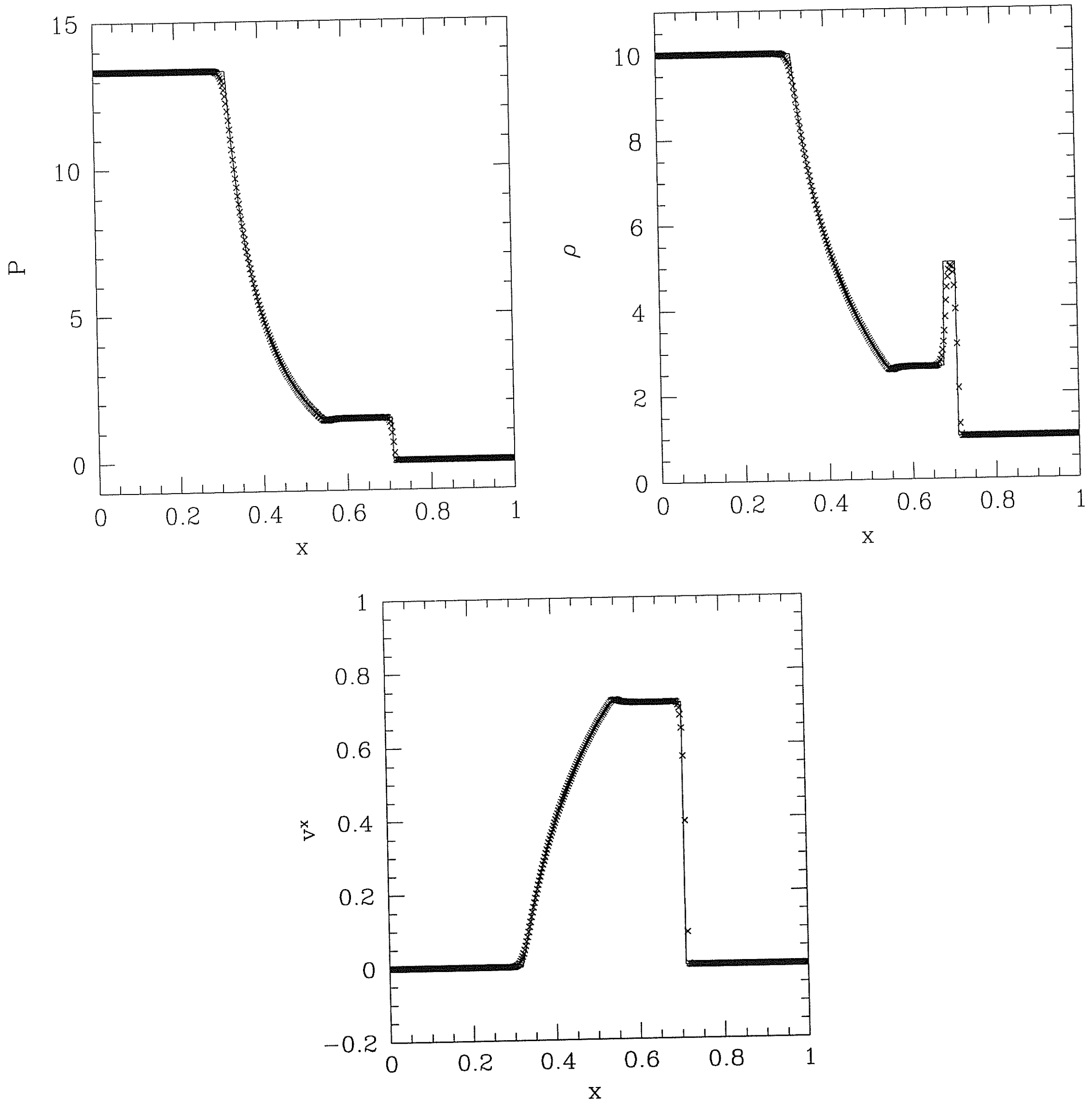

Figure B.1: Pressure, density and x-component of velocity profiles at time $t = 0.25$ for the solution of the shock-tube problem along the x-direction. The exact solution is represented by the solid line and numerical solution by crosses.

Leer MC reconstruction scheme and the Roe approximate Riemann solver. We have used a third order Runge-Kutta scheme to integrate the evolution equations forward in time. These plots show that the agreement between the exact solution and the numerical solution is very good for all three hydrodynamic variables.

B.2 TOV in the Cowling Approximation

In Fig. B.2 we plot in the top panel the evolution of the central rest-mass density for simulations performed with two different resolutions, where the grid spacing is $\Delta x = \Delta z = 0.6$ and $\Delta x = \Delta z = 0.3$. As expected, we observed periodic variations in the central rest-mass density but we also note a secular decrease of the central rest-mass density during the evolution. This secular behaviour reduces with increasing resolution but the numerical solution degrades significantly even in the highest resolution simulations which we have carried out. This behaviour is also clear in the bottom panel of Fig. B.2 where we show the profile of the rest-mass density along the x-direction at the initial time $t = 0$ and at $t = 3$ms. We clearly see that the numerical solution has deviated significantly from the initial solution. We can deduce that there are two possible sources of error that may cause this behaviour. The first is that there might be a coding error in the schemes that we use for the solution of the equations in our evolution code; the second possibility is that this departure from the initial solution may arise from the cartoon method and therefore, from the way in which we compute the reconstructed variables at the cell interfaces that are used for obtaining the fluxes in the y-direction. The most stringent way of discriminating between these two possible causes is to extend the 2D hydrodynamical code to a 3D code using Cartesian coordinates which does not impose axisymmetry and therefore, does not use cartoon method.

A major advantage of a 2D axisymmetric code which makes use of the cartoon method is that it is rather straightforward to extend it to a full 3D code (*i.e.* with no assumption of axisymmetry). This extension does not require significant changes in the original 2D code and it can be done simply by changing the 2-dimensional arrays into 3-dimensional ones. However, this slight modification will allow the primitive hydrodynamic

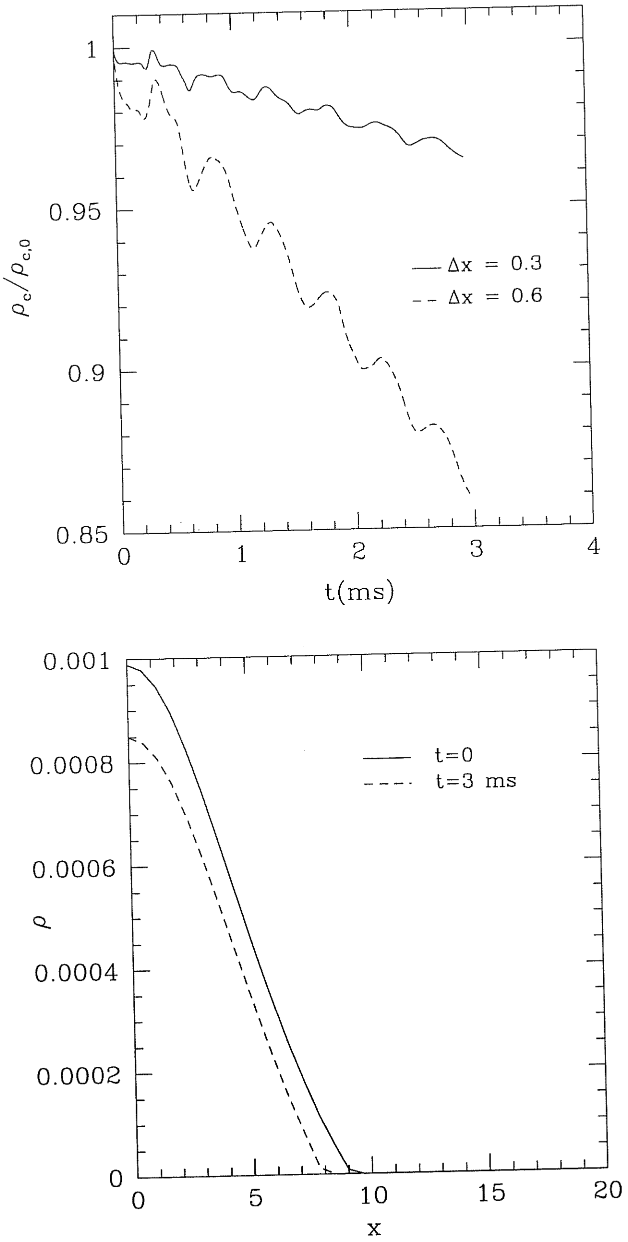

Figure B.2: The top panel shows the evolution of the central rest-mass density for a polytropic star of mass $M = 1.65$, polytropic constant $k = 123.5$ and polytropic index $N = 1$ with two different resolutions, $\Delta x = 0.3, 0.6$. The decrease in the central density is about 15% after 3ms with the coarsest resolution. The bottom panel shows the rest-mass density profile along the radial direction at the initial time $t = 0$ and at $t = 3$ ms with $\Delta x = 0.6$

variables to be reconstructed in the y-direction in exactly the same way as for the x and z-directions.

We have evolved the same TOV initial data with the 3D code and with the 2D code which applies cartoon. In both cases we use the same numerical schemes (as before, MC reconstruction, Roe's solver and third-order Runge-Kutta for the time integration) and the same resolution in order to compare the numerical solutions. In Fig. B.3 we show the evolution of the central rest-mass density obtained with simulations with equal grid spacing in all directions ($\Delta x = 0.6 = \Delta z$ for the 2D run, and $\Delta x = \Delta y = \Delta z = 0.6$ for the 3D run) with both evolution codes. In the top panel, we plot with a solid line the evolution obtained with the 3D code while the dashed line refers to the 2D code. It is clear that the secular evolution of the central rest-mass density obtained with the 3D code is significantly different from that obtained with the 2D code. The latter shows a decrease of the central-rest mass density of about 15% after 3 ms while the 3D code is able to perform a long-term accurate evolution until the numerical simulation was terminated at 15 ms, which corresponds to more than 30 dynamical time scales (defining the dynamical time scale as the fundamental radial mode period of pulsation), with no sign of instabilities. The bottom panel shows a close-up of the data obtained with the 3D code, in which we see that the numerical solution subsequently oscillates about the initial value. The departure from the initial value is about 0.02% at t=15 ms which shows the excellent performance of the 3D code. Through our 3D simulations we have succesfully tested our implementation of the HRSC schemes solving the general relativistic equations in the form given by Banyuls et al. (1997) and in view of these results, we conclude that the problem arises due to the application of the cartoon method to the hydrodynamical equations and that the 2D cartoon code is not able to solve accurately the hydrodynamic equations when axisymmetry is imposed. We have not tested further the 3D code with other initial data as we aimed to continue investigating the dynamics of axisymmetric systems taking advantage of the two dimensionality of the problem.

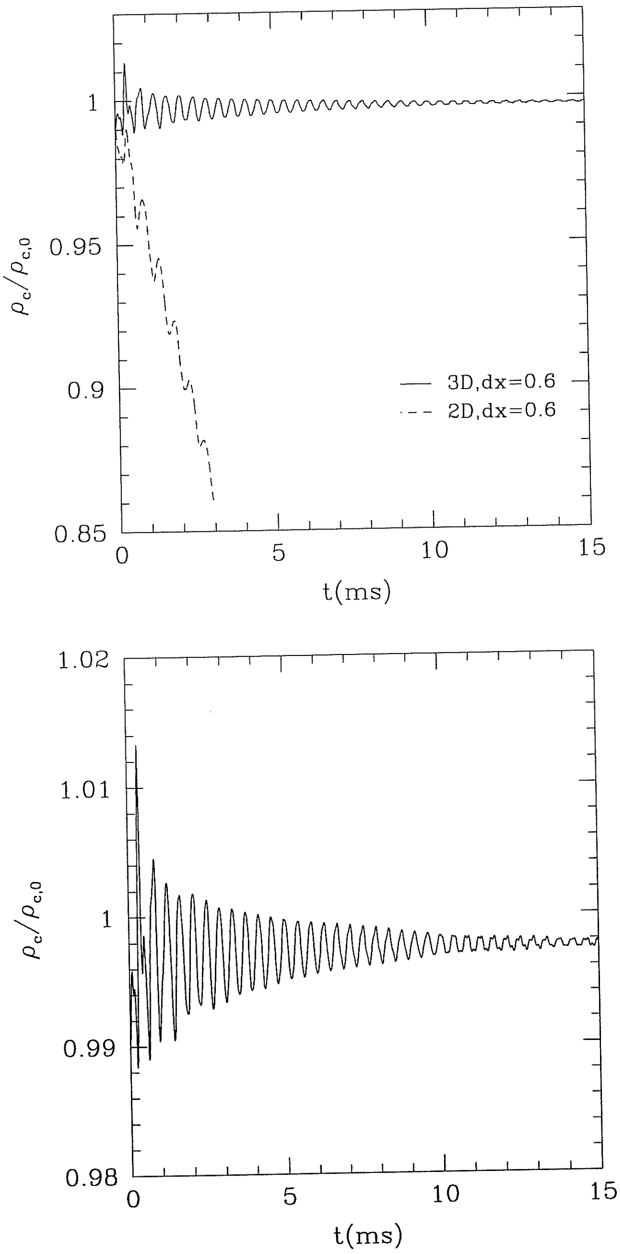

Figure B.3: The top panel shows the evolution of the central rest-mass density of the same polytropic star considered previously, with mass $M = 1.65$, polytropic constant $k = 123.5$ and polytropic index $N = 1$ with $\Delta x = 0.6$. The dashed line refers to results obtained with the 2D code using the cartoon method and the solid line to its extension to 3D. The bottom panel just shows the evolution of central rest-mass density just with the 3D code, showing that it is perfectly stable

Bibliography

[1] M. A. Abramowicz. *Acta Astron.*, 24:45, 1974.

[2] M. A. Abramowicz, M. Calvani, and L. Nobili. *Nature*, 302:597, 1983.

[3] M. A. Abramowicz, M. Jariszyński, and M. Sikora. *A & A*, 63:221, 1978.

[4] M. A. Abramowicz, V. Karas, and A. Lanza. *A & A*, 331:1143, 1998.

[5] M. A. Abramowicz and W. Kluźniak. *A & A*, 374, 2001.

[6] M. A. Abramowicz and W. Kluźniak. Proceedings of *"x-ray timing 2003: rossi and beyond"*, editor = P. Kaaret and F.K. Lamb and J.H. Swank. 2004.

[7] M. A. Abramowicz, W. Kluźniak, and J. P. Lasota. *A & A*, 396, 2002.

[8] M. A. Abramowicz and A. R. Prasanna. *MNRAS*, 245:720, 1985.

[9] M. Alcubierre, G. Allen, B. Brügmann, E. Seidel, and W.-M. Suen. *Phys. Rev. D*, 62:124011, 2000b.

[10] M. Alcubierre, S. Brandt, B. Brügmann, D. Holz, E. Seidel, R. Takahashi, and J. Thornburg. *Int. J. Mod. Phys. D*, 10:273, 2001a.

[11] M. Alcubierre and B. Brügmann. *Phys. Rev. D*, 63:104006, 2001.

[12] M. Alcubierre, B. Brügmann, P. Diener, M. Koppitz, D. Pollney, E. Seidel, and R. Takahashi. *Phys. Rev. D*, 67:084023, 2003a.

[13] M. Alcubierre, B. Brügmann, T. Dramlitsch, J. A. Font, P. Papadopoulos, E. Seidel, N. Stergioulas, and R. Takahashi. *Phys. Rev. D*, 62:044034, 2000a.

[14] M. A. Aloy, J. M$^{\underline{a}}$. Ibáñez, J. M$^{\underline{a}}$. Martí, and E. Müller. *Astroph. J. Supp.*, 122:151, 1999.

[15] P. Anninos, J. Massó, E. Seidel, W.-M. Suen, and M. Tobias. *Phys. Rev. D*, 54:6544, 1996.

[16] P. Anninos, J. Massó, E. Seidel, W.-M. Suen, and M. Tobias. *Phys. Rev. D*, 56:842, 1997.

[17] R. Arnowitt, S. Deser, and C. W. Misner. In L. Witten, editor, *Gravitation: An Introduction to Current Research*, page 227. John Wiley, New York, 1962.

[18] B. Aschenbach, N. Grosso, D. Porquet, and P. Predehl. *A & A*, 417:71, 2004.

[19] L. Baiotti, I. Hawke, P. J. Montero, F. Loffler, L. Rezzolla, N. Stergioulas, J. A. Font, and E. Seidel. *Phys. Rev. D in press*, 2004.

[20] L. Baiotti, I. Hawke, P. J. Montero, and L. Rezzolla. In R. Capuzzo-Dolcetta, editor, *Mem. Soc. Astron. It.*, volume 1, page 327, 2003.

[21] F. Banyuls, J. A. Font, J. Mª. Ibáñez, J. Mª. Martí, and J. A. Miralles. *ApJ.*, 476:221, 1997.

[22] T. W. Baumgarte, S. A. Hughes, and S. L. Shapiro. *Phys. Rev. D*, 60:087501, 1999.

[23] T. W. Baumgarte and S. L. Shapiro. *Physical Review D*, 59:024007, 1999.

[24] T. W. Baumgarte and S. L. Shapiro. *Phys. Rep.*, 376:41, 2003.

[25] O. M. Blaes. *MNRAS*, 216:553, 1985.

[26] C. Bona, J. Massó, E. Seidel, and J. Stela. *Physical Review D*, 75:600, 1995.

[27] R. H. Boyer. *Proc. Cambridge Phil. Soc.*, 61:527, 1965.

[28] S. Brandt, J. A. Font, J. Mª. Ibáñez, J. Massó, and E. Seidel. *Comp. Phys. Comm.*, 124:169, 2000.

[29] B. Brügmann. *Ann. Phys. (Leipzig)*, 9:227, 2000.

[30] `Cactus Computational Toolkit. www.cactuscode.org.`

[31] M. Choptuik. *http://laplace.physics.ubc.ca/People/matt/Teaching/98Spring/Phy387N/Doc/3+1.p* 1998.

[32] P. Collela and P. R. Woodward. *J. Comput. Phys.*, 54:174, 1984.

[33] R. Courant and K. O. Friedrichs. Springer, Germany, 1976.

[34] T. G. Cowling. *MNRAS*, 101, 1941.

[35] F. Daigne and J. A. Font. *MNRAS*, 351:1120, 2004.

[36] F. Daigne and R. Mochkovitch. *MNRAS*, 285:L15, 1997.

[37] R. Donat, J. A. Font, J. Mª. Ibáñez, and A. Marquina. *Journ. Comput. Phys.*, 146:58–81, 1998.

[38] R. Donat and A. Marquina. *Journ. Comput. Phys.*, 125:42, 1996.

[39] M. D. Duez, P. Marronetti, S. L. Shapiro, and T. W. Baumgarte. *Phys. Rev. D*, 67:024004, 2003.

[40] M. D. Duez, S. L. Shapiro, and H. Yo. *Phys. Rev. D*, 69:104016, 2004.

[41] B. Einfeldt. *J. Comp. Phys.*, 25:294, 1988.

[42] K. Eppley. In L. Smarr, editor, *Sources of Gravitational Radiation*, page 275. Cambridge University Press, Cambridge, England, 1979.

[43] G. B. Cook et al. *Phys. Rev. Lett*, 80:2512, 1998.

[44] S. L. Finn. In C. Evans, L. Finn, and D. Hobill, editors, *Frontiers in Numerical Relativity*. Cambridge University Press, England, 1989.

[45] L. G. Fishbone and V. Moncrief. *ApJ*, 207:962, 1976.

[46] J. A. Font. *Living Rev. Relativity*, 6,4, 2003.

[47] J. A. Font and F. Daigne. *MNRAS*, 334:383, 2002a.

[48] J. A. Font and F. Daigne. *ApJ*, 581:L23, 2002b.

[49] J. A. Font, T. Goodale, S. Iyer, M. Miller, L. Rezzolla, E. Seidel, N. Stergioulas, W. M. Suen, and M. Tobias. *Phys. Rev. D*, 65:084024, 2002c.

[50] J. A. Font and J. M$^{\underline{a}}$. Ibáñez. *ApJ*, 494:297, 1998a.

[51] J. A. Font and J. M$^{\underline{a}}$. Ibáñez. *MNRAS*, 298:835, 1998b.

[52] J. A. Font, M. Miller, W. M. Suen, and M. Tobias. *Phys. Rev. D*, 61:044011, 2000a.

[53] J. A. Font, N. Stergioulas, and K. D. Kokkotas. *Mon. Not. R. Astron. Soc.*, 313:678, 2000b.

[54] J. Frauendiener. *Phys. Rev. D*, 66:104027, 2002.

[55] D. Giannios and H.C. Spruit. *A & A*, in press, 2004.

[56] S. K. Godunov. *Mat. Sb.*, 47:271, 1959. in Russian.

[57] A. Harten, B. Engquist, S. Osher, and S. R. Chakrabarty. *J. Comput. Phys.*, 71:2311, 1987.

[58] A. Harten, P. D. Lax, and B. van Leer. *SIAM Rev.*, 25:35, 1983.

[59] J. Homan, J.M. Miller, R. Wijnands, D. Steeghs, T. Belloni, M. van der Klis, and W.H.G. Lewin. *ATel*, 162, 2003.

[60] J. M$^{\underline{a}}$. Ibáñez, M. A. Aloy, J. M$^{\underline{a}}$. Martí J. A. Font, J. A. Miralles, and J. A. Pons. In E.F. Toro, editor, *Godunov methods: theory and applications*. Kluwer Academic/Plenum Publishers, 2001.

[61] J. M$^{\underline{a}}$. Ibáñez, J. A. Font, J. M$^{\underline{a}}$. Martí, and J. A. Miralles. In J. Frieman A. Olinto and D. Schramm, editors, *Proceedings of The 18th Texas Symposium on Relativistic Astrophysics*, Singapore, 1998. World Scientific.

[62] J. M$^{\underline{a}}$. Ibáñez and J. M$^{\underline{a}}$. Martí. *Journal of Computational and Applied Mathematics*, 109:173, 1999.

[63] J. R. Ipser and L. Lindblom. *ApJ*, 389:392, 1992.

[64] S. Kato. *PASJ*, 53:1, 2001.

[65] S. Kato, J. Fukue, and S. Mineshige. *Black-Hole Accretion Disks*. Kyoto University Press, Japan, 1998.

[66] B. Kelly, P. Laguna, K. Lockitch, J. Pullin, E. Scnetter, D. Shoemaker, and M. Tiglio. *Phys. Rev. D*, 64:084013, 2001.

[67] R. Khanna and S. K. Chakrabarti. *MNRAS*, 259:1, 1992.

[68] W. Kluźniak, M. A. Abramowicz, S. Kato, W. H. Lee, and N. Stergioulas. *ApJ*, 603:L89, 2004.

[69] M. Kozlowski and M. A. Abramowicz M. Jaroszynski. *A & A*, 63:209, 1978.

[70] P. Laguna and D. Shoemaker. *Class. Quantum Grav.*, 19:3679, 2002.

[71] L. D. Landau and E. M. Lifschitz. *Mechanics*. Pergamon Press, Oxford, 1976.

[72] W. H. Lee, M. A. Abramowicz, and W. Kluźniak. *ApJ*, 603:L93, 2004.

[73] L. Lehner. *Class. Quantum Grav.*, 18:R25, 2001.

[74] R. J. Leveque. *Numerical Methods for Conservation Laws*. Birkhauser Verlag, Basel, 1992.

[75] R. J. Leveque. In Ed. Steiner O. & Gautschy A., editor, *Computational Methods for Astrophysical Fluid Flow*. Springer-Verlag, 1998.

[76] LIGO - http://www.ligo.caltech.edu/.

[77] Y. Lu, K. S. Cheng, and L. Yang Zhang. *MNRAS*, 341:453, 2000.

[78] D. Lynden-Bell. *Nature*, 223:690, 1969.

[79] T. W. Baumgarte C. Bona D. Fiske T. Goodale F. Siddhartha Guzmán I. Hawke S. Hawley S. Husa M. Koppitz C. Lechner L. Lindblom D. Pollney D. Rideout M. Salgado E. Schnetter E. Seidel H. Shinkai D. Shoemaker B. Szilágyi R. Takahashi M. Alcubierre, G. Allen and J. Winicour. *Class. Quantum Grav.*, 21(2):589, 2004.

[80] A. I. MacFadyen and S. E. Woosley. *ApJ*, 524:262, 1999.

[81] J. M. Martí and E. Müller. *J. Comput. Phys.*, 258:317, 1994.

[82] J. M. Martí and E. Müller. *Living Rev. Relativity*, 2, 1999.

[83] J. M$^{\underline{a}}$. Martí, J. M$^{\underline{a}}$. Ibánez, and J. A. Miralles. *Phys. Rev. D*, 43:3794, 1991.

[84] N. Matsuda, S. Nishida, and Y. Eriguchi. *MNRAS*, 297:1139, 1998.

[85] F. C. Michel. *Astrophys. Spa. Sci.*, 15:153, 1972.

[86] P. J. Montero, L. Rezzolla, and S. Yoshida. *MNRAS in press*, 2004.

[87] E. Müller, M. Rampp, R. Buras, H.-Th. Janka, and D. H. Shoemaker. *ApJ*, 603:221, 2004.

[88] T. Nakamura, K. Oohara, and Y. Kojima. *Prog. Theor. Phys. Suppl.*, 90:1, 1987.

[89] R. Narayan, T. Piran, and P. Kumar. *ApJ*, 557:949, 2001.

[90] S. Nishida and Y. Eriguchi. *ApJ*, 461:320, 1996.

[91] M. A. Novak and R. V. Wagoner. *ApJ*, 378:656, 1991.

[92] I. Novikov and K. S. Thorne. *Black Holes*. B. de Witt and C. de Witt, New York, 1973.

[93] A.T. Okazaki, S. Kato, and J. Fukue. *PASJ*, 39:457, 1987.

[94] European RTN on Sources of Gravitational Waves. `www.eu-network.org`.

[95] J. R. Oppenheimer and G. Volkoff. *Physical Review*, 55:374, 1939.

[96] B. Paczyński and P. J. Wiita. *A & A*, 88:23, 1980.

[97] C. A. Perez, C. A. Silbergleit, R. V. Wagoner, and D. E. Lehr. *ApJ*, 476:589, 1997.

[98] T. Piran. 2004.

[99] J. A. Pons, J. A. Font, J. Mª. Ibáñez, J. Mª. Martí, and J. A. Miralles. *A & A*, 339:638, 1998.

[100] J. A. Pons, J. Mª. Martí, and E. Müller. *Journ. Fluid Mech.*, 422:125, 2000.

[101] W. H. Press, B. P. Flannery, S. A. Teukolsky, and W. T. Vetterling. *Numerical Recipes*. Cambridge University Press, Cambridge, 1986.

[102] R. A. Remillard, E. H. Morgan, J. E. McClintock, C. D. Bailyn, and J. A. Orosz. *ApJ*, 522:397, 1999.

[103] R. A. Remillard, M. P. Muno, J. E. McClintock, and J. A. Orosz. *ApJ*, 580:1030, 2002.

[104] L. Rezzolla, S'i. Yoshida, T. J. Maccarone, and O. Zanotti. 344:L37, 2003c.

[105] L. Rezzolla, S'i. Yoshida, and O. Zanotti. *MNRAS*, 344:978, 2003b.

[106] L. Rezzolla and O. Zanotti. *J. Fluid Mech.*, 449:395, 2001.

[107] L. Rezzolla, O. Zanotti, and J. Pons. *J. Fluid Mech.*, 479:199, 2003.

[108] RIEMANN: http://relativity.livingreviews.org/Articles/lrr-2003-7/index.html.

[109] M. O. Rodriguez, A. S. Silbergleit, and R. V. Wagoner. *ApJ*, 567:1043, 2002.

[110] P. L. Roe. *J. Comput. Phy.*, 43:357, 1981.

[111] M. Ruffert and H H.-Th Janka. *A & A*, 380:544, 2001.

[112] J. D. Schnittman. 2004.

[113] J. D. Schnittman and E. Bertschinger. *ApJ*, 606:1098, 2004.

[114] F. H. Seguin. *ApJ*, 197:745, 1975.

[115] Y. Sekiguchi and M. Shibata. *gr-qc/0403036*, 2004.

[116] M. Shibata. *Phys. Rev. D*, 60:104052, 1999.

[117] M. Shibata. *Prog. Theor. Phys.*, 104:325, 2000.

[118] M. Shibata. *Phys. Rev. D*, 67:024033, 2003a.

[119] M. Shibata. *ApJ*, 595:992, 2003b.

[120] M. Shibata, T. W. Baumgarte, and S. L. Shapiro. *Phys. Rev. D*, 61:044012, 2000.

[121] M. Shibata and T. Nakamura. *Phys. Rev. D*, 52:5428, 1995.

[122] M. Shibata, K. Taniguchi, and K. Uryu. *Phys. Rev. D*, 68:084020, 2003.

[123] M. Shibata and K. Uryu. *Phys. Rev. D*, 61:064001, 2000. gr-qc/9911058.

[124] M. Shibata and K. Uryu. *Phys. Rev. D*, 64:104017, 2001.

[125] M. Shibata and K. Uryu. *Prog. Theor. Phys.*, 107:265, 2002.

[126] C. W. Shu and S. J. Osher. *Journ. Comput. Phys.*, 77:439, 1988.

[127] S. A. Silbergleit, R. V. Wagoner, and M. Rodriguez. *ApJ*, 548:325, 2001.

[128] T. E. Strohmayer. *ApJ*, 552:L49, 2001.

[129] J. L. Tassoul. *Theory of Rotating Stars*. Princeton University Press, 1978.

[130] S. Teukolsky. *Phys. Rev. D*, 26:745, 1982.

[131] S. Teukolsky. *Phys. Rev. D*, 61:087501, 2000.

[132] K. W. Thompson. *J. Fluid Mech.*, 171:365, 1986.

[133] J. Thornburg. PhD thesis, University of British Columbia, Vancouver, British Columbia, 1993.

[134] K. S. Thorne. In S. W. Hawking and W. Israel, editors, *300 Years of Gravitation*. Cambridge University Press, 1987.

[135] M. Tobias. *PhD. Thesis: The Numerical Evolution of Gravitational Waves*. PhD thesis, Washington University, Saint Louis, MO, 1997.

[136] R. C. Tolman. *Phys. Rev.*, 55:364, 1939.

[137] E. F. Toro. *Riemann Solvers and Numerical Methods for Fluid Dynamics*. Springer-Verlag, 1999.

[138] B. J. van Leer. *Journ. Comput. Phys.*, 23:276, 1977.

[139] J. P. De Villiers, J. F. Hawley, and J. H. Krolik. *ApJ*, 599:1238, 2003.

[140] http://www.virgo.infn.it/.

[141] R. V. Wagoner. *Phys. Rep.*, 311:259, 1999.

[142] R. M. Wald. *General Relativity*. The University of Chicago Press, Chicago, 1984.

[143] Whisky, EU Network GR Hydrodynamics Code: `http://www.aei.mpg.de/ hawke/Whisky.html`.

[144] D. B. Wilson. *Nature*, 312:620, 1984.

[145] S. E. Woosley and A. I. MacFadyen. *A & AS*, 138:499, 1999.

[146] H.-J. Yo, T. W. Baumgarte, and S. L. Shapiro. *Phys. Rev. D*, 66:084026, 2002.

[147] J. W. York, Jr. In L. L. Smarr, editor, *Sources of Gravitational Radiation*, page 83. Cambridge University Press, Cambridge, UK, 1979.

[148] O. Zanotti, J. A. Font, L. Rezzolla, and P. J. Montero. *submitted to MNRAS*, 2004.

[149] O. Zanotti, L. Rezzolla, and J. A. Font. *MNRAS*, 341:832, 2003.

[150] T. Zwerger. PhD thesis, Technische Universität München, München, Germany, 1995.

[151] T. Zwerger and E. Müller. *A & A*, 320:209, 1997.